NORTHWESTERN UNIVERSITY

Dynamics of Biomineralization in Sea Urchin Primary Mesenchyme Cells

A DISSERTATION

SUBMITTED TO THE GRADUATE SCHOOL

IN PARTIAL FULFILMMENT OF THE REQUIREMENTS

for the degree

DOCTOR OF PHILOSOPHY

Field of Materials Science and Engineering

By

Bradley Keck Moreno

EVANSTON, ILLINOIS

September 2022

Abstract

Dynamics of Biomineralization in Sea Urchin Primary Mesenchyme Cells

Bradley Keck Moreno

Sea urchins are virtuosi of biomineralization, the process by which organisms build mineralized tissues. The embryonic animal exemplifies this with the formation of its endoskeletal spicule. The primary mesenchyme cells (PMCs) undertake spicule synthesis, which involves deposition of the initial granule, elongation of the spicule, and several choreographed changes in crystallographic direction. The final spicule is smooth and curved single crystalline magnesium calcite ($Ca_{0.95}Mg_{0.05}CO_3$) that also comprises 0.1% embedded organic matrix. Although early PMC morphogenesis has been studied in detail, the precise mechanisms through which the PMCs control spiculogenic events such as granule nucleation, spicule growth, and crystallographic direction switching, are not well-understood. Remarkably, PMC construction of the skeleton is largely autonomous, so PMCs cultured *in vitro* still form spicules. In this dissertation, we leverage *in vitro* PMC culture to dissect the molecular toolkit effecting this complex process of biogenic single crystal growth.

We first build upon and further develop a technique for isolation and culture of PMCs, compatibilizing it with powerful characterization methods such as confocal and electron microscopy. Using *in vitro* culture, pharmacological inhibitors, and fluorescence microscopy, we then examine indirect control of spicule formation through the signaling molecule VEGF and direct control through the cytoskeleton. We find that the temporal distribution of VEGF is a control lever for crystal growth. We also find that the cytoskeleton is essential to spicule formation by enabling macropinocytosis-driven uptake of ions into the mineral.

In another set of experiments, we leverage immunofluorescence to examine the spatial distribution of organic matrix proteins within the spicule. We found a heterogeneous distribution of two key spicule matrix proteins, indicating they have different functions in guiding crystal growth. Finally, in a collaborative project, we use X-ray diffraction and electron microscopy to examine the shell of the gastropod species *C. fornicata* and find that it comprises aragonitic crossed-lamellar microstructure.

Our results expand upon theories for spiculogenesis. The formation of the sea urchin spicule is a model system for studying biomineralization, and we thus expect that the results herein will elucidate analogous processes in other organisms and in materials synthesis.

Acknowledgements

I first would like to thank my advisor Derk Joester for admitting me to his research group and for six years of guidance and mentoring. Becoming a scientist takes years of patient support, and I am thankful for our conversations that transformed me into a mature researcher and STEM professional. I also would like to thank my committee members Kenneth Shull, Nathan Gianneschi, and Deirdre Lyons for their insights and feedback.

I am indebted to the mentorship I received early on within the Joester group. Emily Campbell, thank you for imparting your technical knowledge of the sea urchin project to me, and for providing invaluable advice regarding not only the Ph.D., but career development in general – you steered my tenure as a graduate student in the right direction from day one. Noah Metoki, thank you for helping me climb out of the early-mid Ph.D. rut by encouraging me to take more initiative with my own experiments and to be less afraid of making mistakes in the laboratory. Vivian Merk, thank you for salvaging many of my first materials characterization sessions at Northwestern and for sharing your veteran insights of the biomineralization field. Keith Alvares, thank you for continued support and collaboration within the sea urchin project and for being an inexhaustible source of biology and biotechnology know-how.

To past and current group members, I am thankful for the sense of community we have fostered. Karen DeRocher and Robert Free, thank you for teaching me materials characterization sample preparation that was initially quite foreign to a chemistry undergraduate major. Utthara Rameshbabu, I am grateful that we came to Evanston at the same time and grew together as professionals. Allessandra DiCorato, thank you for camaraderie within the group and countless hours spent sharing pastries and inside jokes in the office. Victoria Cooley, thank you for being a

wonderful officemate and for sharing memes on and off campus. Danielle Duggins, thank you for working with me to deal with any catastrophes that popped up in the sea urchin tank room or laboratory. Maya Kompella, it was my honor to mentor you throughout your undergraduate research project and I know you will go far in your academic and career pursuits.

In addition to members of the Joester Group, I received guidance and feedback from individuals at other groups or facilities at Northwestern, as well as from outside the university. I would like to thank Jessica Hornick of the Northwestern University Biological Imaging Facility (BIF) for training me on the confocal microscopes and for providing valuable feedback on sample preparation and image collection. I also thank Carla Shute of the Materials Characterization and Imaging Facility (MatCI) for helping me with sample preparation. Similarly, I would like to thank Tirzah Abbott of the Northwestern University Electron Probe Instrumentation Center (EPIC) for training me on the electron microscopes and Jerry Carsello of the Jerome B. Cohen X-Ray Diffraction Facility for training me on the XRD systems. I would also like to thank Woojong Lee for advising me on confocal microscopy sample preparation, no matter how late at night I needed help troubleshooting issues. To Grant Batzel and advisor Deirdre Lyons of The University of California, San Diego, it was a pleasure to collaborate with you on the *C. fornicata* project.

This work was made possible by the National Science Foundation (NSF-IOS-1456837). I gratefully acknowledge support given by the Ryan Fellowship and the Northwestern University International Institute for Nanotechnology (IIN). Confocal microscopy was performed at BIF, which is supported by the Chemistry for Life Processes (CLP) Institute, the Northwestern University Office for Research, and the Rice Foundation. Electron microscopy was performed at

EPIC at the Northwestern University Atomic and Nanoscale Characterization Experimental Center (NU*ANCE*), which has received support from the Soft and Hybrid Nanotechnology Experimental (ShyNE) Resource (NSF-ECCS-1542205), the Northwestern University Materials Research Science and Engineering Center (NU-MRSEC) program (NSF-DMR-1720139) at the Materials Research Center, the IIN, the Keck Foundation, and the State of Illinois through the IIN. X-ray diffraction was performed at the Jerome B. Cohen X-Ray Diffraction Facility supported by the MRSEC program of the NSF (NSF-DMR-1720139) at the Materials Research Center and the ShyNE Resource (NSF-ECCS-1542205).

Preface

Chapter 2. A version of Chapter 2 has been published as Moreno, B., DiCorato A., Park, A., Mobilia, K., Knapp, R., Bleher, R., . . . Joester, D. (2019). Culture of and experiments with sea urchin embryo primary mesenchyme cells. *Methods Cell Biol*, 150, 293-330. Doi:10.1016/bs.mcb.2019.01.002. The version published in this thesis has been edited in some respects to fit within the context of other chapters and for brevity. This work expanded on a technique originally developed by Okazaki and Wilt. Charlene Wilke and Reiner Bleher of the BioCryo NU*ANCE* core facility at Northwestern University prepared primary mesenchyme cell cultures for transmission electron microscopy (TEM) and Allessandra DiCorato imaged the cell cultures on a TEM. Charles Ettensohn of Carnegie Mellon University provided monoclonal antibodies against MSP-130. Keith Alvares collected total RNA from cell cultures. Derk Joester was the supervising author throughout this work and the other authors contributed to manuscript edits and provided feedback while writing.

Chapter 3. The majority of Chapter 3 was written as a manuscript. Keith Alvares synthesized and purified rVEGF and provided a written protocol thereof. Keith Alvares also helped with project conceptualization and provided manuscript feedback and edits. Derk Joester was the supervising author for this project.

Chapter 4. The majority of Chapter 4 was written as a manuscript. Maya Kompella stained primary mesenchyme cell cultures with calcein and wrote a custom MATLAB program to obtain intensity profiles from confocal images. Keith Alvares helped with project conceptualization and provided manuscript feedback and edits. Derk Joester was the supervising author for this project.

Chapter 5. Maya Kompella expanded on the spicule blot technique originally developed by Kitajima to compatibilize it with our available laboratory equipment and confocal microscopes. Maya Kompella performed the spicule blots and helped image some of the samples. Derk Joester was the supervising author for this project.

Chapter 6. The majority of Chapter 6 was written into a manuscript and accepted for publication in Integrative Organismal Biology. This project was a collaboration between groups at Northwestern University and The University of California San Diego. Grant Batzel and Deirdre Lyons provided *C. fornicata* shells. Derk Joester was involved in data interpretation and manuscript editing. Grant Batzel was the lead doctoral investigator for this project. Deirdre Lyons was the supervising author for this project.

Dedication

To everyone who has supported me throughout my Ph.D.

Table of Contents

List of Figures

Figure 6.2. Length scales of the crossed-lamellar microstructure of the shell of *C. fornicata*. (A) Ventral view of the adult shell. (B-C) Reflected, polarized light microscopy images of sections approximately normal to the anterior-posterior axis. A number of macro layers with different orientations of 1˚ lamellae are visible where the shelf is joined to the shell (B); on the arc between these junctions three macro layers can be recognized by the slightly different orientation of the banding pattern (dashed lines, C). (D) SEM image of a fracture surface, approximately normal to the anterior-posterior axis. White arrows indicate first order (1˚) lamellae. (E) Higher magnification image from the same area in B. (F) SEM image of a polished and etched surface on the plane normal to the posterior-anterior axis and looking down the posterior direction. Black arrows indicate boundaries between 1˚ lamellae and white arrowheads indicate boundaries between second order (2˚) lamellae. (G) SEM image of third order (3˚) lamellae (white arrows) in a fracture surface. (H) SEM image showing 3˚ lamellae (white arrows) in neighboring 1˚ lamellae in a polished and etched sample. 163

Chapter 1. Introduction

1.1. Biomineralization

Biomineralization is the process by which organisms form mineralized tissues from chemical building blocks in their local environments. This is an ancient process, as fossil evidence exists for cyanobacteria organizing sand into stromatolites as far as 3.5 billion years ago.[1] True biomineralization likely emerged during the Cambrian Explosion 600 million years ago in the form of skeletal body parts and has since dominated the fossil record.[2, 3] Mineralizing organisms quite literally shape the world, as biomineralization plays a fundamental role in global element cycling. Magnificent examples adorn the planet; stony corals lock up calcium and carbon dioxide into the aragonite of their massive skeletons, which forms entire ecosystems such as the Great Barrier Reef.[4] Coccolithophores, a class of marine plankton, lock up oceanic bicarbonate into their calcite shells, with yearly blooms large enough to be visible from space.[5] Diatoms, another class of marine plankton, mold silicic acid into their silica exoskeletons, which form the *diatom*aceous soil of brackish water ecosystems and fertilize the Amazon basin.[6]

Structurally, biominerals differ tremendously from their geological and synthetic counterparts. Instead of the typical thermodynamically favored mineral geometries, biominerals often express complex shapes and hierarchical organization. For example, diatom shells (referred to as frustules) can assume rectangular, oval, and other more complex structures and incorporate patterned nanopores (Figure 1.1).[7, 8] Adding further subtlety, biominerals are nanocomposite materials that comprise an inorganic mineral phase (such as calcium carbonate or silicon dioxide) and an organic phase (such as proteins and/or polysaccharides). A classic example is the mollusk shell type nacre, for which fracture surfaces will show stacked tablets of aragonite;

however, light etching reveals alternating layers of aragonite and organic matrix (Figure 1.2).[9] Biominerals also exhibit unique and tightly controlled chemical structures and crystal polymorphs, as they often have high ratios of substituted elements that are extremely difficult to achieve synthetically and comprise crystalline phases that are thermodynamically unstable.[10-12] For example, gastropod shells usually comprise aragonite, which is a less thermodynamically stable polymorph of calcium carbonate than calcite, and have high Sr/Ca substitution ratios.[13] Incidentally, these sorts of chemical features provide a record of both past and current environmental conditions, as gastropod shell Sr/Ca ratios correlate with water salinity while fossilized marine carbonate $^{18}O/^{16}O$ ratios can be used to calculate paleotemperature differences with 1 °C resolution.[14]

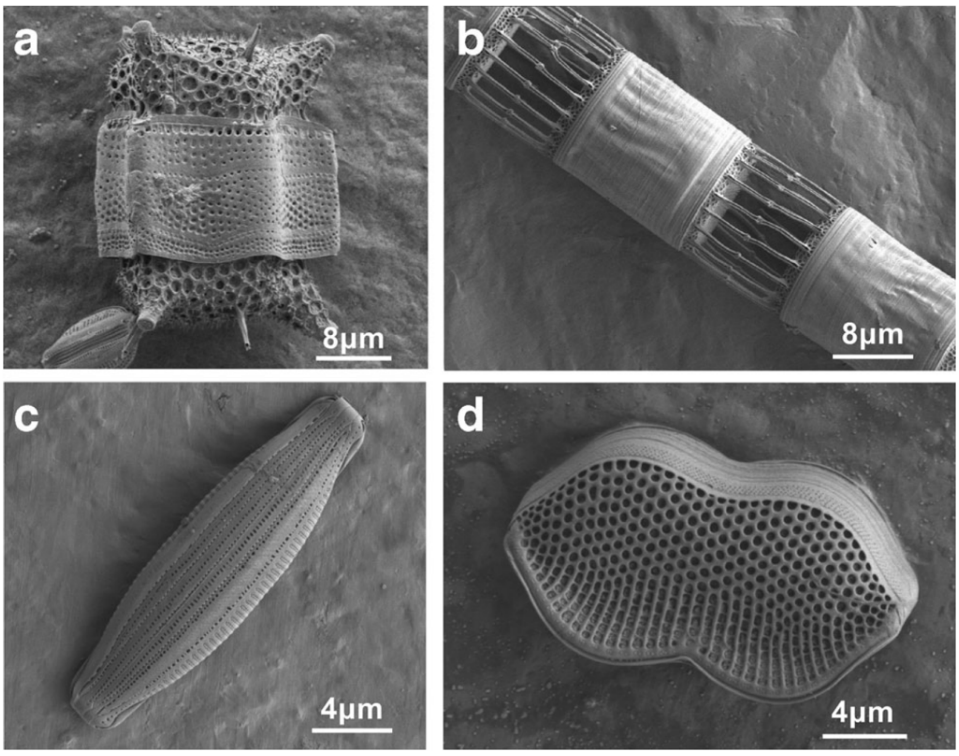

Figure 1.1. Example scanning electron microscope (SEM) images of diatom frustules. (A) *Biddulphia dubia*, (B) *Skeletonema* sp., (C) *Amphora holsatica*, (D) *Tryblionella* sp. Reproduced from reference 7.[7]

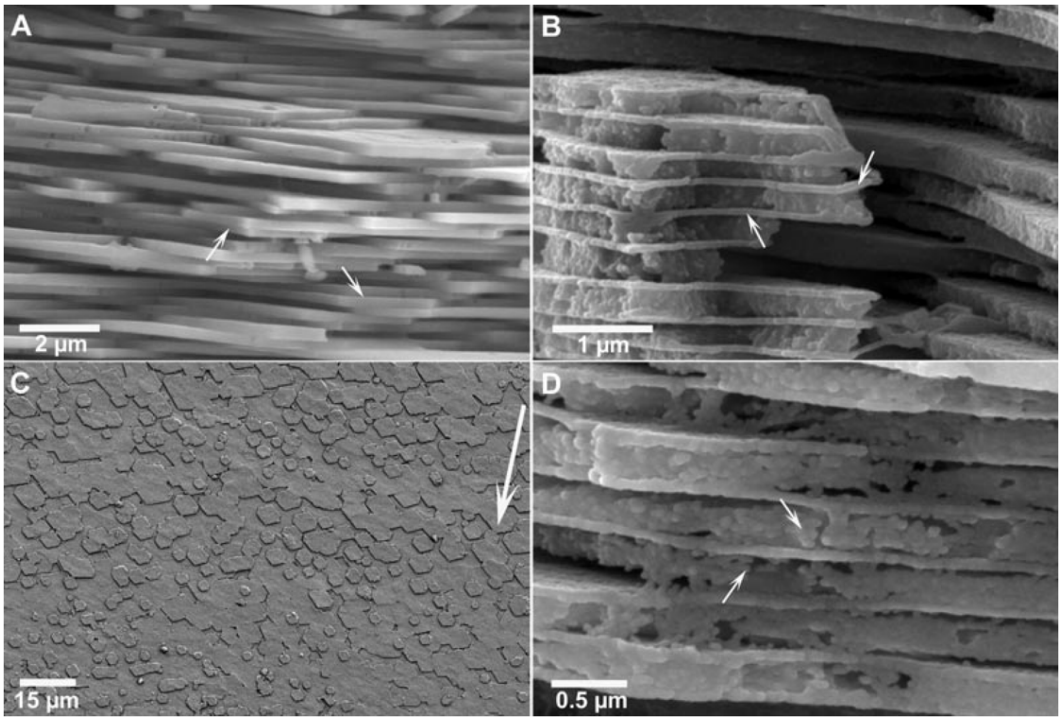

Figure 1.2. Example SEM images of nacre from the bivalve species *Atrina rigida* (A, C) and the cephalopod species *Nautilus pompilius* (B, D). (A) Fracture surface of nacre perpendicular to the shell. (B) Fracture surface of nacre perpendicular to the shell after light etching with EDTA. (C) Nacre growth front on the inner shell surface. (D) Higher magnification image emphasizing organic material between aragonite bricks. Reproduced from reference 9.[9]

Evolution works in response to environmental and competitive pressure, so it follows that a biomineral's form inevitably fits to its function, resulting in a host of interesting properties. The body of the brittle star species *Ophiocoma wendtii* is covered in refractive calcite microlenses that direct light to photoreceptor cells, an obvious adaptation to living in a dark and murky environment.[15] Far down the evolutionary tree to Chordata, mammalian bones combine the advantages of a collagen matrix, which gives flexibility and fracture resistance, and hydroxyapatite (a polymorph of calcium phosphate), which is hard and strong; these properties are highly advantageous to organisms like mammals that must maintain active and physically demanding lifestyles.[16] As a final microscopic example, magnetotactic bacteria form linear chains of magnetite single crystals that they use to navigate along magnetic field lines in search

of low-oxygen areas, a clever materials trick from organisms dwelling on the periphery of mud and water.[17]

1.2. Biomineral Applications and Inspired Technologies

In addition to beauty and natural aesthetics, biominerals have long provided serious research matter. The construction of materials with tailored properties including but not limited to crystallinity, solubility, and mechanical strength at room temperature, atmospheric pressure, and under physiological conditions is a feat envious to human engineering. Consequently, researchers study the fundamental properties governing biomineralization to enhance materials synthesis while scouring the biomineralizing phyla for engineering marvels to emulate. Direct use of, mimicry of, and bio-inspired engineering derived from biominerals have been used to enhance technology across fields as diverse as chemistry, biomedical engineering, electrical engineering, and materials science and engineering.

Many biominerals are readily transformed or functionalized for direct use in applications. Diatoms have been used in several such cases. Through artful chemistry, researchers have converted diatom frustules from the original silica into other compounds such as silicon, magnesium oxide, and titanium dioxide while retaining the nanofeatures and high porosity and surface area of the starting material.[18, 19] In the case of the silicon frustule, the material displayed measurable changes in electrical impedance from changes in nitrous oxide as small as 1 ppm, thus becoming a powerful gas sensor. In another group, researchers edited the genome of the diatom species *Thalassiosira pseudonana* to induce the organism to produce and incorporate the enzyme hydroxylaminobenzene mutase (which catalyzes the rearrangement of hydroxylaminobenzene to 2-aminophenol, a precursor for dyes and high-performance polymers)

into its frustule.[20] The protein was chemically stable and retained enzymatic activity while immobilized inside the biogenic silica, transforming the frustule into a potent catalyst. Another example of direct use of biominerals is stony corals. Researchers have long established that coral skeletons act as effective scaffolds in bone grafts owing to their macroporosity and solubility.[21] More recent work has demonstrated that the aragonite of stony corals can be transformed into calcium phosphate, which is chemically similar to bone and hence biocompatible, with high Mg and Sr substitution, which encourages osteogenesis.[22]

Understanding the structures of biominerals and how they relate to their superior properties makes possible the reverse engineering of similar materials. The Joester group recently characterized the tooth of the chiton species *Cryptochiton stelleri* and discovered a gradient of increasing mineral (in this case, santabarbarite and amorphous ferrous phosphate (AFP)) content and a corresponding gradient of mechanical hardness and elastic modulus that ranged over several orders of magnitude.[23] These nuanced and continuously graded mechanical properties found within a biomineral inspired the synthesis of chitosan-AFP composites with tunable hardness and elastic modulus and the ability to be 3D printed. Another group at Northwestern University similarly paid heed to mollusk biominerals and fabricated metal-ceramic "nacre" that consisted of alumina bricks sandwiched between thin layers of nickel.[24] The hybrid material gained many of the toughening mechanisms of natural nacre such as crack deflection and branching, making it suitable for structural applications requiring high damage resistance.

The fundamental pathways through which biominerals arise inform the design of analogous systems *in vitro*. The Joester group has studied nucleation and growth of calcium

carbonate minerals confined within synthetic liposomes, a concept derived from the enclosed vesicular spaces in which many biominerals form.[25-27] Confinement inside synthetic lipid bilayer membranes enabled stabilization of amorphous calcium carbonate (ACC), probably by altering the kinetics of formation of the crystalline phases of calcium carbonate. More recent work made use of microfluidic "droplet orchards" that grew tens to hundreds of ACC-bearing liposomes in parallel, a strategy that could open the path to mass synthesis of amorphous precursor materials that could be later crystallized with non-equilibrium forms and compositions.[28] In a similar vein of thinking, researchers at Harvard found inspiration in the biological control over polymorph and crystallographic orientation via organic molecules such as acidic proteins.[29] Using self-assembled monolayers (SAMs) of alkanethiols terminated with functional groups such as carboxylates, they achieved patterned and oriented growth of calcite and were even able to stabilize ACC that could later be crystallized.

1.3. The Sea Urchin

1.3.1. Sea urchin biomineralization

As researchers sampled nature's vast array of mineralizing organisms to study, the sea urchin emerged as a perennial favorite. Throughout their lifecycles, they are virtuosi of calcite ($CaCO_3$) mineralization, forming intricate exo- and endoskeletal tissues. Furthermore, because many sea urchin species are plentiful and relatively easy to keep alive in aquaria, they are an attractive organism for research laboratories.

The adult sea urchin primarily mineralizes three body parts: the test, the spines, and the teeth (the claw-like pedicellaria are only partially mineralized and will not be discussed here); all three comprise magnesium calcite with occluded organic matrix.[30-32] The test functions as the

carapace enclosing the animal's internal organs and is formed by interlocking plates; every plate behaves as a single crystal under polarized light and X-ray diffraction, excluding the rounded tubercles on which the spines attach in a ball-and-socket joint.[30] The spines protect the animal from predation through suicide mechanisms, stabbing predators and then usually breaking or autotomizing, and are thus able to regenerate.[33] Each whole spine diffracts and birefringes as a massive single crystal elongated in its *c*-axis.[30] The teeth of the animal are held inside the Aristotle's lantern feeding organ and are used to graze on algae. Certain regions of the tooth have very elevated (≥40%) magnesium ion substitution, resulting in high hardness.[31, 32]

The sea urchin embryo is a free-swimming larva that mineralizes two identical endoskeletal elements referred to as spicules. Like the adult's biomineralized structures, spicules are composed of magnesium calcite with a small (~0.1%) fraction of occluded organic matrix.[34] From a materials science perspective, the sea urchin spicule is remarkable in several ways. It birefringes and diffracts as a calcite single crystal, but instead of displaying the faceted rhombohedral geometry of synthetic and geological calcite, it is smooth and curved with species-specific morphology.[35] In addition, it has been shown that the spicule is significantly stronger than geological calcite.[36]

Sea urchin spiculogenesis is a convenient system to study biomineralization for several reasons. A single female can shed millions of eggs while spawning, so there is no difficulty in obtaining sufficient material. Sea urchin embryos develop rapidly (e.g., in *Strongylocentrotus purpuratus*, the spicule finishes growing within four days), setting the timescale of an experiment at several days, a significant advantage over mammalian studies. Finally, sea urchin embryos are optically transparent and amenable to experimental manipulation, so they are simple

to observe and work with under light microscopy and are preparable for other techniques such as cryogenic electron microscopy and transmission electron microscopy (TEM).

1.3.2. Sea urchin embryonic development and spiculogenesis

To contextualize the formation of the sea urchin spicule, a brief review of the relevant stages of embryonic development is warranted.[37, 38] At the 16-cell stage, uneven cell cleavage results in the formation of the micromeres (Figure 1.3A). They divide several times and by the early blastula stage differentiate into the primary mesenchyme cells (PMCs), which gather at the vegetal plate and migrate into the blastocoel in an epithelial to mesenchymal transition (EMT) (Figure 1.3B-C). During the gastrula stage, the PMCs form two mirror symmetric groups referred to as ventrolateral clusters (VLCs) (Figure 1.3D). Later, the PMCs migrate and pattern along the blastocoel, fuse their membranes to form the syncytium and syncytial cables, and extend thin filopodia (Figure 1.3D-E).

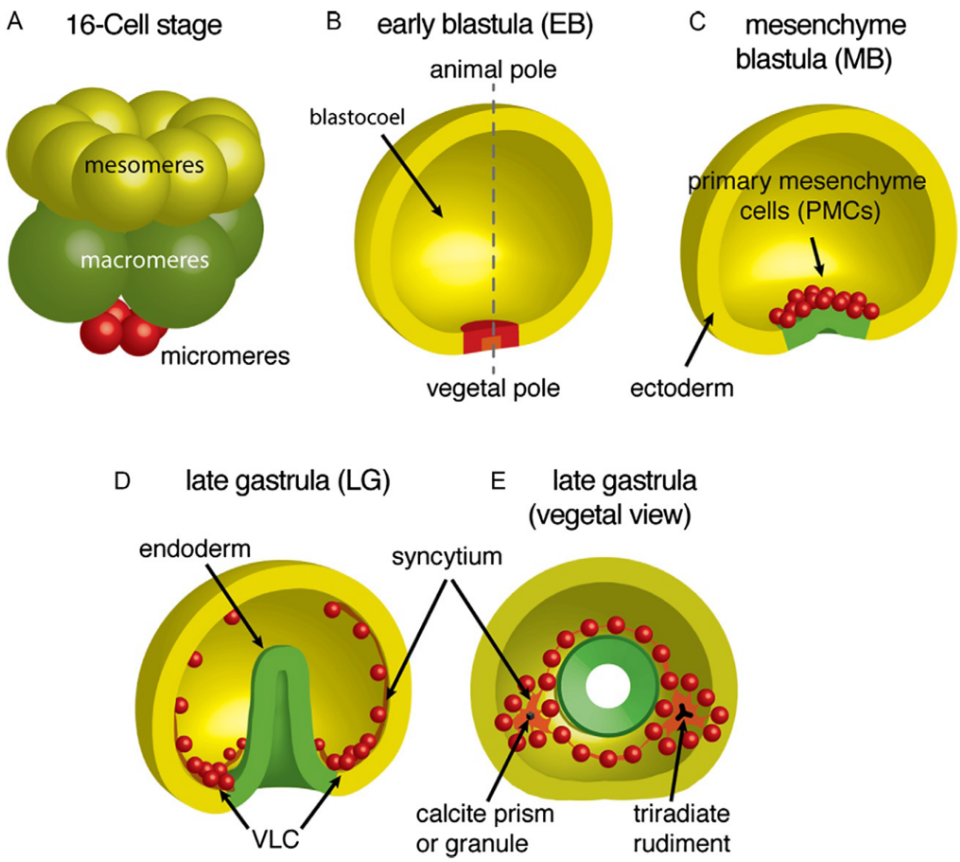

Figure 1.3. Embryonic development of *S. purpuratus* leading up to spiculogenesis. (A) Micromeres emerge at the vegetal pole of the embryo at the 16-cell stage. (B-C) By the early blastula stage, the micromeres differentiate into the PMCs, which by the late blastula stage ingress into the blastocoel in an EMT. (D) The PMCs group into two VLCs and fuse their membranes to form the syncytia. (E) The PMCs deposit a calcite granule within each VLC.

Spiculogenesis begins around the time of the late gastrula stage with the controlled deposition of a calcareous granule in each VLC (Figure 1.3E, Figure 1.4B). The granule grows along the three *a*-axes of calcite to form the triradiate rudiment (Figure 1.4C). One of the triradiate arms stops growing in the *a*-axis of calcite and forms the midventral rod (Figure 1.4D). During the prism stage, another triradiate arm switches directions 90° into the *c*-axis of calcite to form the postoral rod (Figure 1.4D). The remaining triradiate arm also turns 90° into the *c*-axis of calcite but grows in both the positive and negative directions to form the anterolateral rod and

the longer body rod (Figure 1.4D). These choreographed changes in growth and crystallographic direction result in the formation of the mature spicule of the pluteus (Figure 1.4E).

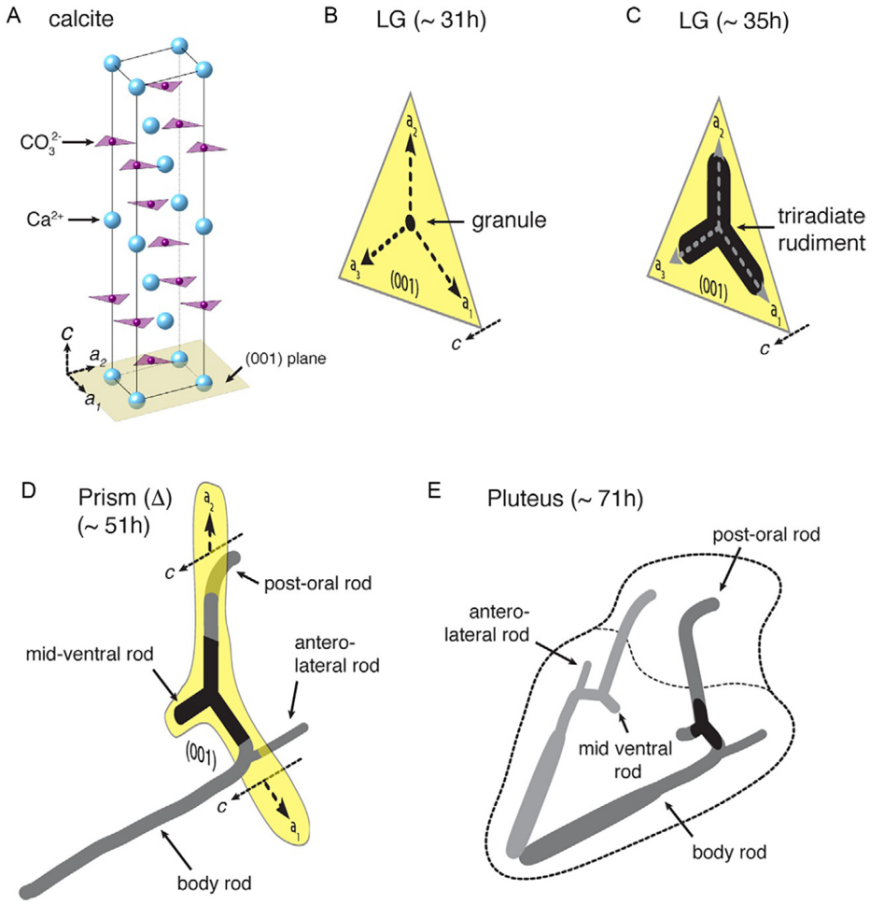

Figure 1.4. Crystallography of calcite in the sea urchin spicule. (A) Rendering of the calcite lattice; note the arrangement of Ca^{2+} and CO_3^{2-} ions in alternating planes along the *c*-axis. (B) Initial granule deposition during the late gastrula stage. (C) Triradiate growth along the *a*-axes during the late gastrula stage. (D) During the prism stage, one of the triradiate arms stops growing, and the other two switch direction 90° into the *c*-axis of calcite. (E) The mature endoskeleton within the pluteus embryo.

1.3.3. Spiculogenesis: a model system for biogenic single crystal growth

The formation of the sea urchin spicule is an archetype of biogenic single crystal growth and presents the chance to examine how organisms use their molecular toolkits to overcome environmental constraints and build complex minerals. For example, an obstacle faced by marine organisms is that for crystal growth to initiate, the constituent ion concentrations must be raised beyond supersaturation conditions. This challenge is thought to be at least partially overcome by

using transmembrane protein ion pumps to locally raise target ion concentrations: some of these proteins have been identified as important to spicule formation.[39, 40] As another example, many organisms shape the nascent mineral through addition of an amorphous precursor phase that later crystallizes, enabling far more complex crystal morphologies and control over solubility.[41] In the sea urchin embryo, it has been suggested that the early spicule comprises a large amount of ACC[42] and that spherical nanoparticles, possibly ACC, are present in vesicles near the growing spicule, likely trafficked there for deposition.[43, 44] Lastly, biomineralizing organisms typically secrete macromolecules such as proteins and polysaccharides into the mineralization compartment, where they assemble into matrices that help shape the mineral and possibly influence growth parameters such as the reversible work of nucleation.[45] These macromolecules often end up incorporated into the final mineral and alter material properties such as fracture mechanics.[46] In the sea urchin spicule, over 200 proteins are occluded in the spicule.[47] Some of them, when present in supersaturated calcium carbonate solution, stabilize ACC.[48] These same proteins also form hydrogels in solution, suggesting a role as an organic scaffold in which the spicule grows.[49]

Much can be learned about biomineral formation from experimenting with and observing the sea urchin embryo and spicule. However, another advantage of this system is that the sea urchin's gene regulatory networks (GRNs), including the spiculogenic micromere-PMC GRN, have been dissected in detail, and are possibly the most well-understood GRNs in all of biology[50, 51] (although much remains to be uncovered!). The sea urchin thus presents a unique opportunity to understand a biogenic crystal growth process at every stage from gene regulation, to cellular morphogenesis and biochemical reactions, to the nucleation and growth of crystal.

The potential to map genes to materials formation and properties would break barriers between scientific disciplines, indeed.

1.4. Thesis Overview

In this dissertation, the sea urchin's mineralizing PMCs were studied *in vitro* to elucidate the dynamics of spiculogenesis. Significant attention was spent on method development to enhance the capabilities of *in vitro* PMC culture beyond its original scope. Although the basis of the method had been previously established by Okazaki and Wilt, the technique was further developed to facilitate more consistent experimental results and adapted for use in confocal fluorescence microscopy, transmission electron microscopy, and RNA collection for sequencing (Chapter 2). The *in vitro* PMC culture system developed herein enables dissection of a model biomineralization system and can be leveraged for projects outside the scope of this thesis.

Macromolecules that indirectly (Chapter 3) or directly (Chapter 4) affect spiculogenesis were examined using the *in vitro* PMC culture system. In Chapter 3, the critical role of the VEGF-VEGFR signaling pathway was investigated to determine the relation between the temporal distribution of VEGF and spicule morphology. The timing of VEGF presence was demonstrated to be another signaling lever controlling crystal growth. In Chapter 4, the role of the cytoskeleton in directing spicule growth was studied using pharmacological inhibitors and fluorescence microscopy. Major cytoskeletal molecules actin and tubulin were demonstrated to play critical roles in spiculogenesis, whereas micropinocytosis-associated molecules dynamin and clathrin, as well as motor protein dynein, were shown to be unimportant to spiculogenesis.

The method of spicule blot previously developed by Kitajima was updated for characterization techniques such as confocal fluorescence microscopy and was used to study the

localization of matrix proteins within the spicule (Chapter 5). This method development enables higher resolution imaging of the organic matrix occluded within the spicule and a similar approach could be adapted for use in electron microscopy and with other biominerals produced by the sea urchin or different organisms.

In a detour, the biomineralizing organism *Crepidula fornicata* was studied in a collaborative project with another group at The University of California San Diego (Chapter 6). The animal's shell was studied both in terms of the gene regulatory network that governs its formation as well as its resulting microarchitecture; in this dissertation, the focus was on the latter. It was concluded that the shell comprises aragonitic crossed-lamellar microstructure, a common form among marine gastropods.

Chapter 2. Foundational Method Development

2.1. *In Vitro* Primary Mesenchyme Cell Culture

2.1.1. Introduction to and advantages of *in vitro* primary mesenchyme cell culture

What makes the sea urchin system truly unique is that the micromere-primary mesenchyme cell (PMC) lineage is largely autonomous in the construction of the skeleton.[52] While extrinsic factors do not have a significant influence on the early skeletogenic gene regulatory network,[53-55] local, ectoderm-derived factors play an integral part in patterning and spicule growth.[56-61] Several such factors, including VEGF, FGF, and Univin, have been identified.[57, 60, 62] In addition, a role for thyroid hormone and integrin signaling is emerging.[63] An important consequence of this high level of autonomy is that PMCs can be grown *in vitro*, outside their biological niche, and that they retain the capability to synthesize spicules in culture.[64, 65] In fact, cell behavior, including micromere division, differentiation into PMCs, migration, fusion to form the syncytium, deposition of the granule, and subsequent spicule growth all occur at the same time as the same events in the whole embryo.[65] This autonomy is a highly desirable, though exceedingly rare, feature for biomineralizing tissues and has enabled bio-engineering single crystal growth.[66] *In vitro* culture of PMCs is furthermore poised to help dissect signaling pathways, the role of effector genes, and the molecular mechanisms of skeletogenesis.

It can be fundamentally challenging to separate, in the embryo, the impact of signaling on cell differentiation from the effect on cellular behavior such as motility, directed migration, skeletal patterning, and spiculogenesis.[67] Inhibition of signaling may have indirect effects, such as gene expression and differentiation that is the consequence of perturbed cellular motility, and

vice versa. Experiments using PMCs *in vitro* offer the advantage of eliminating such indirect effects. In addition, it is much more straightforward to control concentrations of signaling factors, inhibitors, and extracellular matrix components, and study the impact of spatial or temporal gradients of these factors.

For example, prior work documented the effect of cytoskeletal inhibitors on PMC filopodia, and the migration of PMCs toward extracellular matrix obtained from mesenchyme blastulae.[68] More recently, other groups used inhibitors to take a closer look at the role of actin in filopodia number and length.[69] Researchers have also used Ca^{2+} channel blockers to study ion trafficking in PMC cultures.[70] The Joester group discovered that VEGF has a dramatic concentration-dependent effect on the shape of spicules deposited by PMCs *in vitro*: triradiates (closely resembling those initially deposited in the embryo) require a threshold concentration of VEGF, and below this concentration, markedly different spicule shapes are formed.[71] Remarkably, the change in shape is accompanied by a change in the crystallographic growth direction of the spicule.

In many cases, signaling will use canonical pathways and therefore involve gene products that are not PMC-specific. The ability to selectively read out the cellular response of *in vitro*-grown PMCs with high sensitivity, by transcriptomic, proteomic, or metabolomic approaches is therefore a powerful addition to conventional analysis of cellular behavior and spatiotemporal expression in the embryo. By definition, however, *in vitro* experiments are only ever approximations to the physiological situation and require *in vivo* work to validate proposed mechanisms.

2.1.2. Background and alternatives

Large scale isolation and culture of micromeres and their differentiation into mineralizing PMCs was first reported by Kayo Okazaki in a series of seminal papers.[64, 65] The original protocol was adapted to several North American species, further refined, and taught to many researchers by Fred Wilt.[72-74] Alternatively, differentiated PMCs can be isolated by dissociation of embryos at later stages of development.[75] Rather than taking advantage of the difference in cell size at the 16-cell stage that is integral to the Okazaki-Wilt protocol, this approach uses the selective adhesion of PMCs to substrates coated with wheat germ agglutinin (WGA). In this dissertation, spiculogenesis was found to be more robust in PMCs generated by the micromere isolation route, presumably because the dissociation of 16-cell stage embryos can be performed under much gentler conditions.

More recently, it has been shown that fluorescence-activated cell sorting (FACS) can be used to isolate PMCs from dissociated embryos that express a cell type specific reporter transgene.[76] This, however, required heroic effort, as a low total average yield of 1.5% (~5800 cells) required injecting 12,000 embryos per replicate. It is not known whether PMCs so isolated will produce spicules *in vitro*. Micromeres and PMCs can further be isolated in small numbers by micromanipulation, as shown by Ettensohn, McClay, and others.[52, 77, 78] While this approach is most often used to transplant PMCs from one embryo to another, it has recently been demonstrated that fusion and migration of explanted PMCs can be studied *in vitro*.[67] Obviously, the number of cells that can be explanted in this fashion is limited. Finally, opening the double repressor gate that controls PMC specification, by injection of *pmar1* mRNA or *hesC* morpholino antisense oligonucleotide into the fertilized egg, results in production of several

thousand PMCs per embryo.[79, 80] Spiculogenesis can, at least to some degree, be induced in *P. lividus* PMCs generated by this route by co-injection of *vegf3* mRNA.[57] While this approach could be very useful in that it allows genetic manipulation or the introduction of reporter genes, it has not been explored as a means to generate PMCs for further experiments.

2.1.3. Overview and general remarks

Where larger numbers of cells are required, the Okazaki-Wilt protocol remains the most reliable access to PMCs *in vitro*. The protocol herein is presented with some modifications that have worked well for us with *S. purpuratus*. Key steps of this protocol are the dissociation of 16-cell stage embryos and separation of micromeres from larger cells by sedimentation on a sucrose gradient. Note that all steps are carried out at 15 °C in a climate-controlled room, and that developmental times reported here are thus based on this temperature.

This protocol requires at least 6-8 mL of eggs (packed, before fertilization). Depending on the quality of animals and time of the breeding season, intracoelomic injection of 2-3 females may not provide a sufficient volume; we typically obtained ~1 mL of eggs per female after KCl injection. Therefore, we opted to instead remove the Aristotle's lantern and squirt KCl directly into the body cavity to induce spawning, which can result in as much as 15 mL of eggs per female. This procedure sacrifices approximately 5 animals per micromere isolation experiment (2-3 females and 1-2 males to ensure genetic diversity), thus the need for a continuous supply of animals must be taken into consideration.

In this chapter, the volume of artificial seawater (ASW) used to culture the embryos is specified, as well as the initial volume of fertilized eggs. These volumes are convenient to work with and the protocol will generate a number of micromeres (approximately 300,000 micromeres

per mL of eggs) that facilitates their isolation. Volumes can be adjusted, but it is important to maintain the same ratio of ASW to eggs because adjusting the embryo density can alter development times.

It is imperative that the preparation of sucrose gradients is completed prior to dissociation of the embryos. Each gradient takes 30-45 min to pour. It is recommended to set up the gradient mixer and peristaltic pump to begin making the first gradient at least an hour before fertilization. Subsequent gradients can be set up between development points or while waiting for the embryos to sediment. Gradients are stable for several hours at 15 °C, and longer when stored on ice (~4 °C). We observed superior band separation when gradients were stored and used on ice.

Note that to induce spiculogenesis, the media is typically supplemented with horse serum (HS), ideally starting around 24-26 hpf.[54] Not all horse sera are equally effective, and sera from other vertebrates oftentimes do not induce spiculogenesis. It is not known what factor(s) in HS is required. In the presence of recombinant Lp-Vegf3 (rVEGF), we have observed spiculogenesis in cultures of *S. purpuratus* PMCs treated with fetal bovine serum (FBS).[71] Matrigel has been reported as an alternative to HS,[81] but we found inconsistent success using it; it is also rather expensive.

In terms of culture substrates, cell culture plastic works very well. The elastomer PDMS, used frequently in microfluidic systems, is well tolerated.[66] Glass substrates preferable for high resolution, polarized, or fluorescent light microscopy can be problematic. An acid wash, described below, is frequently required. Adhesion and migration of PMCs on glass substrates can be further improved by coating with fibronectin, but we generally find it unnecessary.[67, 68, 82]

Microcontact printing of WGA on glass substrates has been used successfully to pattern PMCs *in vitro*.[66]

Finally, a few words on contamination and purity. Contamination with bacteria, primarily from the gastrointestinal microbiota, is inevitable, but can usually be managed by sterile filtering of solutions and use of antibiotics. Media have occasionally been observed to turn cloudy with growth of filamentous microorganisms, most likely fungi. Contaminated serum is a suspect. Given that this does not happen very often, and in view of possible side effects, the use of antifungal agents is not recommended. While not required, it is a good idea to set aside some embryos for a control culture. Monitoring developmental progress and timing *in vivo* is a useful way to identify issues that arise from poor quality of embryos rather than from improper technique or bacterial/fungal contamination. In terms of cell purity, Wilt estimated that preparations contain 5-15% non-PMC cells from the sea urchin embryo. Based on a preliminary analysis of RNA-seq data and comparison of absolute expression levels, it is estimated that with the protocol presented herein, the fraction of non-PMC cells is likely below 1% (Figure 2.1).

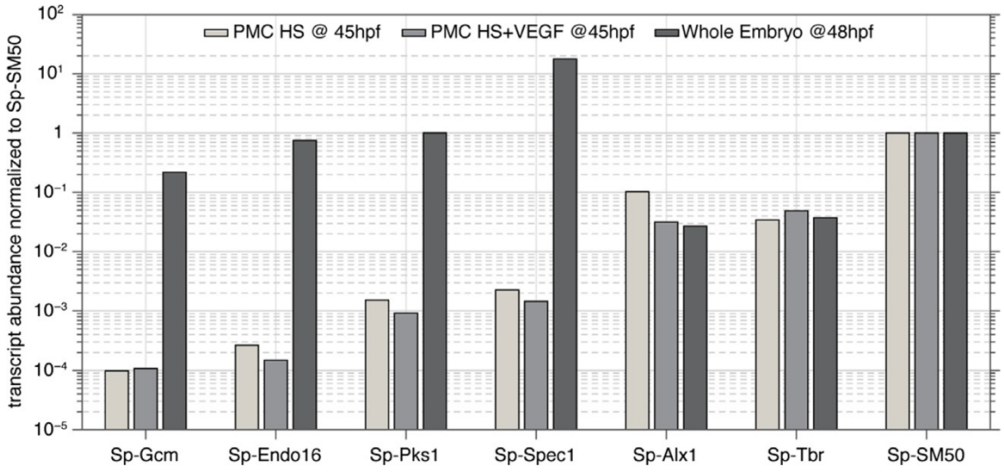

Figure 2.1. Comparison of the abundance of selected transcripts in PMCs *in vitro* (unpublished data) and in whole sea urchin embryos.[83] Markers for endoderm (*Sp-Endo16*), mesoderm (*Sp-Gcm*), aboral ectoderm (*Sp-Spec1*), and pigment cells (*Sp-Pks1*) are depleted by at least 3 orders of magnitude *in vitro*, while PMC markers (*Sp-Alx1*, *Sp-Tbr*, *Sp-SM50*) are present at comparable abundance. Note that abundance (in FPKM) was normalized to that of *Sp-SM50*.

2.1.4. Materials

Chemicals and Disposables:

Unless otherwise noted, all reagents were stored at room temperature (22 °C). Ethanol (200 proof) (Decon Laboratories Inc., King of Prussia, PA); concentrated bleach (8.25% NaClO) (The Clorox Company, Oakland, CA); NaCl (≥99.5%), $MgSO_4$ (anhydrous, 99.5%), $CaCl_2 \cdot 2H_2O$ (≥99%), $NaHCO_3$ (≥99%), concentrated HCl (35-37%), Na_2SO_4 (anhydrous, ≥99%), *p*-aminobenzoic acid (PABA, ≥99%, stored at 4 °C), sucrose (≥99.5%), gentamicin sulfate (≥590 $\mu g \cdot mg^{-1}$, stored at 4 °C), penicillin + streptomycin (100× stock, 10,000 $U \cdot mL^{-1}$ penicillin + 10,000 $\mu g \cdot mL^{-1}$ streptomycin in 0.85% NaCl, 0.1-µm sterile filtered, stored at -20 °C) (Sigma-Aldrich, St. Louis, MO); $MgCl_2 \cdot 6H_2O$ (≥99%), KCl (≥99%) (Avantor, Radnor, PA); NaOH (≥99%), horse serum (HS, sterile, heat inactivated, stored at -20 °C, Gibco (Cat #26050)/Thermo Fisher Scientific (Cat # 26050088)) (Thermo Fisher Scientific, Waltham, MA); Instant Ocean® sea salt (Instant Ocean, Blacksburg, VA).

Sterile Falcon tubes (15-mL, 50-mL), Corning sterile poly(ether sulfone) filter units (0.22-µm, 1-L), polystyrene weighing boats, Cellvis tissue culture dishes (29-mm^2 with 20-mm^2 #1.5 glass bottom insert), rubber pipette bulbs (1-mL) (Thermo Fisher Scientific, Waltham, MA); sterile polystyrene serological pipettes (10-, 20-mL) (TPP, Trasadingen, Switzerland); sterile low-binding pipette tips (1-20-, 100-1,000-µL,) (Midwest Scientific, Valley Park, MO); rubber bands, disposable glass Pasteur pipettes (2-mL), disposable graduated polyethylene pipettes (1-mL) (VWR, Radnor, PA); Scotch tape (3M, Maplewood, MN); dialysis tubing Spectra/Por (12,000-14,000 kDa molecular weight cut-off) (Repligen, Waltham, MA).

Equipment:

Beakers (50-, 400-, 600-mL), screw top bottles (1-, 3-L), graduated cylinders (100-, 500-, 1,000-, 2,000-mL), gradient mixer (two 250-mL reservoirs connected by Teflon stopcock, one of the reservoirs equipped with an outflow fitted with another Teflon stopcock), LDPE carboys with polypropylene spigot (4-L), plastic tray (35 cm × 15 cm × 35 cm), plastic ice buckets (2-L), polypropylene plastic squirt bottle (300-mL), RS-5883 surgical grade scissors (Thermo Fisher Scientific, Waltham, MA); Dumoxel® tweezers (120 mm length) (Electron Microscopy Sciences, Hatfield, PA); single-channel adjustable volume pipettes (2-20-, 20-200-, 100-1,000-µL), centrifuge 5810R (with temperature control, swing-bucket rotor with four 500-mL buckets, conical 50- and 200-mL inserts) (Eppendorf, Hamburg, Germany); mini incubator (VWR, Radnor, PA); Nylon mesh (55-µm) (Sefar, Buffalo, NY); cell counting chamber (Hausser Scientific Partnership, Horsham, PA); Portable Pipet-Aid® XP2 Pipette Controller (Drummond Scientific, Broomall, PA); Pumpdrive 5201 peristaltic pump, MR Hei-Mix L magnetic stir plate (Heidolph, Schwabach, Germany); dimpled bottom spinner flasks (500-mL), Dura-Mag nine-position digital stirrer (Chemglass Life Sciences, Vineland, NJ); vacuum aspirator with trap (Sigma-Aldrich, St. Louis, MO).

Solutions:

Unless otherwise noted, all aqueous solutions were prepared with ultra-pure water (UPW, $\rho = 18.2$ M·Ω·cm) dispensed by a Barnstead NanoDiamond UF + UV purification unit and stored at 15 °C.

A solution of 0.50 M KCl was prepared by dissolving 18.6 g KCl in 500 mL UPW. 70% ethanol was prepared in UPW. A stock solution of 250 mM PABA was prepared by dissolving

17.1 g PABA in UPW, adjusting the pH to ~8.0 by addition of NaOH while stirring, and bringing the final volume to 500 mL with addition of UPW; this solution was kept in the dark. A stock solution of 0.75 M sucrose was prepared by dissolving 89.9 g sucrose in 350 mL UPW. A stock solution of 1 $mg \cdot mL^{-1}$ gentamicin sulfate was prepared in UPW.

All seawater solutions were filtered with 0.22-μm Corning filter. ASW was prepared with the following final concentrations: 0.48 M NaCl, 0.10 M $CaCl_2 \cdot 2H_2O$, 0.01 M KCl, 0.03 M $MgSO_4$, 0.027 M $MgCl_2 \cdot 6H_2O$, and 0.002 M $NaHCO_3$. Calcium free artificial seawater (CFSW) was prepared with the following final concentrations: 0.48 M NaCl, 0.01 M KCl, 0.03 M $MgSO_4$, 0.027 M $MgCl_2 \cdot 6H_2O$, and 0.002 M $NaHCO_3$. Calcium and magnesium free artificial seawater (CMFSW) was prepared with the following final concentrations: 0.48 M NaCl, 0.01 M KCl, 0.06 M Na_2SO_4, and 0.002 M $NaHCO_3$. "Heavy" sucrose solution was prepared by diluting 300 mL (1 part) sucrose stock solution in 900 mL (3 parts) CFSW and adding 12 mL (1% (v/v)) gentamicin sulfate stock solution. "Light" sucrose solution was prepared by diluting 30 mL (1 part) sucrose stock solution in 570 mL (19 parts) CFSW and adding 6 mL (1% (v/v)) gentamicin sulfate stock solution.

A volume of 100 mL HS was dialyzed twice against 1 L ASW overnight at room temperature (molecular weight cutoff = 12,000-14,000 kDa), sterile filtered with a 0.22-μm Corning filter, and separated into 4 mL-aliquots that were stored at -20 °C.

2.1.5. Methods

Adult animals:

Sea urchins were purchased from Marinus Scientific (Long Beach, CA) and South Coast Bio-Marine LLC (San Pedro, CA) and maintained in Instant Ocean® seawater at 15 °C.

Sucrose gradient preparation:

Both stopcocks of the gradient mixer were closed. Six 250-mL beakers were partially filled with 100 mL of the heavy solution (the "cushion" of the gradient). 90 mL of the heavy solution and a magnetic stir bar were placed into the gradient mixer reservoir with one inflow and one outflow and 90 mL of the light solution was placed into the other reservoir. The stirrer was turned on, a tube was connected to the outflow of the gradient mixer, and this tube was taped to the side of one of the 250-mL beakers with a heavy solution cushion. The connecting and outflow stopcocks of the gradient mixer were opened, and the peristaltic pump was turned on (4 $mL \cdot min^{-1}$) to create a gradient on top of the cushion. After completion (~45 min) the gradient was gently put on ice and, using a pair of tweezers, a square 2 cm × 2 cm plastic baffle cut from a weighing boat was placed on top of the gradient. Gradient layering was repeated for each of the 250-mL beakers with a heavy solution cushion.

Gamete collection:

Animals were held in one hand with the mouth facing up while the other hand used scissors to cut a circle around the ring of soft tissue between the perignathic girdle and the teeth. The Aristotle's lantern was pulled out with a pair of tweezers and the coelomic fluid was discarded. A squeeze bottle was used to squirt 2-3 mL of KCl solution into the body cavity and the animal was swirled to wet the gonads. After shedding began (~10-30 s), females were placed upside down on 50-mL beakers filled *to the brim* with ASW, and males on empty 50-mL Falcon tubes on ice. Shedding finished after 10-20 min.

Fertilization:

3 spinner flasks were filled with 400 mL ASW and placed on the stir plate. 8 mL of PABA stock solution was added to each spinner flask (final PABA concentration ~5 mM) and the stir plate was turned on (60 rpm). Eggs were washed by transferring from beakers to 50-mL Falcon tubes, centrifuging (100 × *g*, 2 min), removing supernatant, resuspending in ASW, and allowing to settle at 1 × *g*; this was repeated once. 2 mL of eggs were added to each spinner flask (~0.5 mL eggs per 100 mL ASW + PABA), using a plastic Pasteur pipette. 40 µL of sperm were diluted in 40 mL ice-cold ASW (~1:1000) and, using a glass Pasteur pipette, 10-15 mL of this solution were added to each spinner flask. Using a light microscope, fertilization was confirmed by the appearance of the fertilization membrane.

Weakening the hyaline membrane:

At 0.5 hpf, each embryo culture was passed through a 55-µm Nylon mesh into 600-mL glass beakers. Using a light microscope, it was confirmed that at least 90% of embryos were stripped of the fertilization membrane; else, the culture was passed through the mesh again. Cultures were allowed to settle at 1 × *g* for 20 min. Two-thirds of the supernatant were removed by suction and replaced with an equivalent volume of CFSW to lower the calcium concentration from 10 mM to 3.3 mM. Each culture was returned to its flask on the stir plate.

At the 4-cell stage (approximately 2.5-3 hpf), embryo cultures were centrifuged (100 × *g*, 2 min). Supernatant was removed by suction and embryos were gently resuspended in 400 mL of CFSW. Each embryo culture was returned to its flask on the motor plate.

Embryo dissociation:

At the 16-cell stage (approximately 4.5-5 hpf), each culture was divided into two equal volumes (e.g., two 200-mL Falcon tubes) for centrifugation (100 × *g*, 2 min). Supernatant was removed by suction and each pellet was resuspended in 50 mL CFSW and transferred to 50-mL Falcon tubes. Embryos were collected by centrifugation (100 × *g*, 2 min), supernatant was removed by suction, and embryos were resuspended in 50 mL CMFSW and put on ice. Embryos were collected by centrifugation (450 × *g*, 2 min) and supernatant was reduced to 10 mL by suction. Embryos were resuspended and triturated with a 10-mL serological pipette. Dissociation of at least ~80% of the embryos was confirmed using a light microscope; else, trituration was repeated. Embryos were immediately resuspended in 50 mL CFSW per separate 50-mL Falcon tube. Dissociated embryos were collected by centrifugation (450 × *g*, 5 min). Supernatant in each tube was reduced to 10 mL by suction and embryos were resuspended using a 10-mL serological pipette.

Micromere isolation:

Gradients were removed from ice. 10 mL of suspended cells were gently layered over the plastic baffle so that the gradient was not disrupted; this was repeated for each gradient. Cells were allowed to settle at 1 × *g* for 20-30 min, after which the micromere band was visible several millimeters beneath the top of the gradient. 35-40 mL of solution were collected from the micromere band of each gradient by suction (10-15 mL at a time, each gradient allowed 3-5 min to reform). One volume of 1.0 M $CaCl_2$ was added per 100 volumes of collected micromere suspension and the Falcon tube was immediately capped and inverted. Micromeres were collected by centrifugation (450 × *g*, 5 min). 30 mL of supernatant was collected and set aside

for potential cell dilution. The remaining supernatant in each Falcon tube was reduced by suction to 7.5 mL. Micromeres were resuspended by trituration using a 10-mL serological pipette and all micromere suspensions were collected into one 50-mL Falcon tube.

Micromere and PMC culture

Micromere density was determined using a hemocytometer. Cell density was adjusted, if necessary, to 50,000-75,000 cells·mL^{-1} (to dilute, the appropriate volume of previously collected supernatant was added and gently mixed; to concentrate, micromeres were collected by centrifugation (450 × *g*, 5 min), supernatant was reduced to the desired volume, and cells were gently resuspended using a 10-mL serological pipette). Cells were plated approximately 100,000 cells per 29-mm^2 Petri dish and additional ASW was added to bring the total volume to 2 mL, if necessary. Petri dishes were covered with lids and micromeres were allowed to settle and adhere for 1 h.

ASW was supplemented with gentamicin sulfate (1 µg·mL^{-1}, 1:100 dilution of stock) and penicillin + streptomycin (1×, 1:100 dilution of stock) (this solution is henceforth referred to as ASWGPS). Each plate was washed with ASWGPS (2×, 2 mL). To wash, media were removed by suction using a 10-20 µL disposable pipette tip on tubing connected to an aspirator, and 2 mL of ASWGPS was added gently from the side of the plate while rotating the plate so as not to dislodge the micromeres in one area. At 24 hpf, plates were washed with ASWGPS (2×, 2 mL). This time, plates were gently swirled before aspirating media to collect debris and detached cells in the middle of the plate. At 26 hpf, plates were washed (2×, 2 mL) with the cell culture media of choice (e.g., 4% (v/v) HS in ASWGPS) and incubated in these media.

Cells were cultured to the desired timepoint. Typically, granule deposition began at 31-32 hpf (Figure 2.2A), spicule rudiments appeared at 38 hpf (Figure 2.2B), and spicules were well-developed by 48 hpf (Figure 2.2C). Cultures were viable to 96-108 hpf but then turned morbid. Different media were added later if required by the experiment. The cell culture medium was switched simply by washing with ASWGPS (2×, 2 mL) and the desired media (2×, 2 mL), or only the desired media.

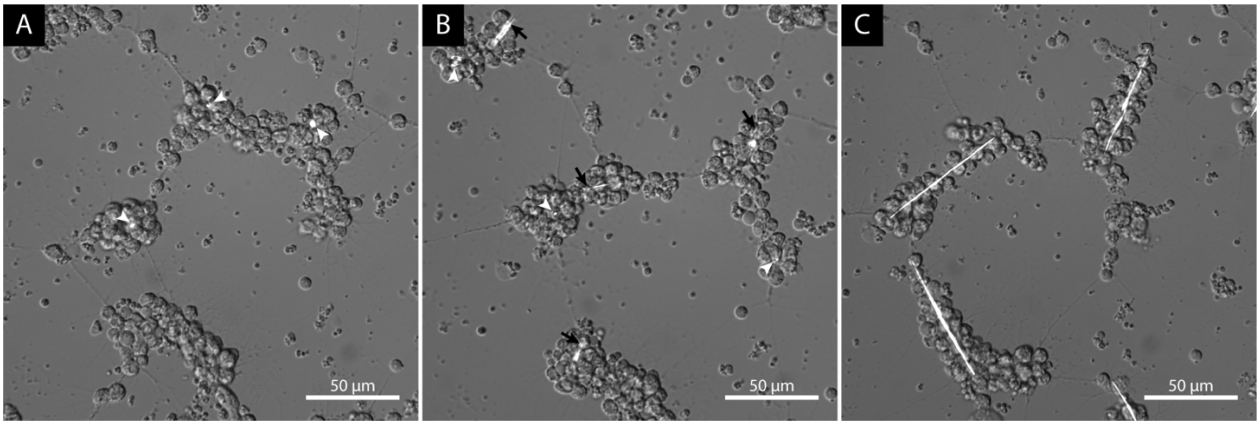

Figure 2.2. PMC cultures at progressive stages of development. (A) At 32 hpf, PMCs have clumped together. Small granules several microns in diameter (white arrowheads) are visible inside the cell clusters. (B) At 38 hpf, the granules have elongated along the *c*-axis of calcite to form small linear spicule rudiments (black arrows). (C) By 48 hpf, large (>50 µm) linear spicules have formed. Images taken from a time lapse series in the same x-y position; differences in PMC location are due to cell migration and misalignment between figure frames. Images are overlays of differential interference contrast (DIC) and polarized light (pol).

2.2. Optical and Fluorescence Microscopy of Primary Mesenchyme Cell Cultures

2.2.1. Background and overview

Fluorescence staining is critical for analysis of the time course and localization of proteins in cells and tissues. It has been widely used on whole embryos and most methods that work on embryos can be adapted to PMC cultures. Nuclear stains such as DAPI or Hoechst 33342, membrane stains such as the FM or DiI series of dyes, cytoplasmic stains such as calcein-AM, and phalloidin-based stains of filamentous actin have all been used successfully.[78, 84] Primary antibodies raised against endogenous proteins of the sea urchin embryo are frequently

used; examples include monoclonal antibodies against MSP-130,[85] and antibodies against SM50, SM30, and PM27.[86] The specificity and binding of antibodies raised against highly conserved vertebrate proteins should be validated, but there are examples where such antibodies, for instance against actin or tubulin, work well.[69] Finally, stains such as calcein and fluorescent conjugates of wheat germ agglutinin and dextran have been used to track endocytotic vesicles and biomineralization.[43, 44, 87, 88]

Fluorescently tagged fusion proteins generated by microinjection of engineered mRNAs into the embryo are fairly routine to study protein localization *in vivo*. This technique has only rarely been used to study PMCs in culture, because it currently requires extraction of small numbers of PMCs by microsurgery.[89]

Here, a procedure for fixation and permeabilization of PMC cultures is discussed in the example of staining with an Alexa Fluor® conjugate of phalloidin to image filamentous actin. Procedures for working with antibodies are then discussed with the example of staining with antibodies against MSP-130 and an Alexa Fluor®-conjugated secondary antibody to image cell membranes. Nuclei staining with Hoechst 33342 is also covered; we remark that we typically observed superior signal-to-noise ratios using Hoechst dyes than with DAPI.

As there are a great number of fluorescent labels that can be used in many combinations, here the focus is on general aspects of preparing PMC cultures for fluorescent staining. Very generally, one differentiates between stains that are compatible with live cells (e.g., calcein, calcein-AM, Hoechst 33324, FM and DiI) and those where cells must be fixed and permeabilized (e.g., antibodies against intracellular proteins, phalloidin, DAPI). The choice of fixative, permeabilization method, and the sequence in which dyes are applied when multiplexing is

desired are important and depend strongly on the specific dyes used. Many times, manufacturers will give recommendations that will serve as a good starting point, but optimization is necessary. Finally, when analyzing mineralizing PMCs and depending on the application, it is sometimes desirable to avoid dissolving the spicule or completely dissolve it. Spicules can be dissolved by lowering the pH (≤6) or supplementing the media with EDTA or EGTA. Spicule dissolution is avoided by maintaining a high pH (~8) and depressing calcite solubility by addition of calcium ions or by saturating wash solutions with calcium carbonate.

2.2.2. Materials

Chemicals and disposables:

Unless otherwise noted, all reagents were stored at room temperature (22 °C). Methanol (≥99.9%), concentrated HCl (35-37% (w/w)), glycine (≥99%), saponin (8-25% sapogenin), bovine serum albumin (BSA, ≥98%, stored at 4 °C) (Sigma Aldrich, St. Louis, MO); NaOH (≥99.1%), paraformaldehyde (PFA, 16% (w/v)), phalloidin Alexa Fluor® 568 conjugate (phalloidin-CF®568, stored in the dark at -20 °C), goat anti-mouse IgG IgM IgA (H + L) secondary antibody Alexa Fluor® 488 conjugate (goat anti-mouse CF®488, 2 $mg \cdot mL^{-1}$ in 5 mM NaN_3, stored in the dark at 4 °C), Hoechst 33342 (10 $mg \cdot mL^{-1}$, stored in the dark at 4 °C) (Thermo Fisher Scientific, Waltham, MA).

Sterile Falcon tubes (15-, 50-mL), Cellvis 29-mm^2 tissue culture dishes with 20-mm^2 #1.5 glass bottom insert, (Thermo Fisher Scientific, Waltham, MA); sterile polystyrene serological pipettes (10-mL, 20-mL) (TPP, Trasadingen, Switzerland); sterile low-binding pipette tips (100-1000 µL, 1-20 µL) (Midwest Scientific, Valley Park, MO); Eppendorf® tubes (1.7-mL, 0.5-mL) (Eppendorf, Hamburg, Germany).

Equipment:

Volumetric flask (250-mL), beakers (250-, 400-mL), graduated cylinders (50-, 100-mL) (Thermo Fisher Scientific, Waltham, MA); mini-incubator (VWR, Radnor, PA); single-channel adjustable volume pipettes (20-200-, 100-1,000 µL) (Eppendorf, Hamburg, Germany).

Solutions:

Unless otherwise noted, all aqueous solutions were prepared with ultra-pure water (UPW, $\rho = 18.2$ M·Ω·cm) dispensed by a Barnstead NanoDiamond UF + UV purification unit and stored at 15 °C.

A solution of 2.5 M NaOH was prepared by dissolving 50 g NaOH in 500 mL UPW. A solution of 1.0 M HCl was prepared by diluting 20.75 mL concentrated HCl in a 250-mL volumetric flask with UPW.

To avoid spicule dissolution, the pH of all solutions incubated with cell cultures was checked and adjusted to ~8.0 by titration with 2.5 M NaOH, if necessary. The fixative of 4% PFA was prepared in ASW. A 300 mM glycine solution was prepared by dissolving 1.12 g glycine in 50 mL ASW. A 0.30% (w/v) saponin permeabilizing solution was prepared by dissolving 45 mg saponin in 15 mL ASW. A 0.05% (w/v) saponin solution was prepared by diluting the 0.30% (w/v) saponin solution 1:6 in ASW. 300 units (U) of phalloidin-CF®568 were dissolved in 1.5 mL of methanol to produce a 200 $U \cdot mL^{-1}$ stock solution, which was aliquoted and stored in the dark at -20 °C. A stock solution of 100 $\mu g \cdot mL^{-1}$ Hoechst 33342 was prepared in ASW and stored in the dark at 4 °C.

The anti-MSP-130 mouse monoclonal antibody cell supernatant (referred to as 6a9) was synthesized according to an established protocol[85] by Dr. Charles Ettensohn and provided as a gift. 6a9 solution was stored at 4 °C.

2.2.3. Methods

Preparation of glass bottom plates:

Glass bottom plates were filled with 3 mL 1.0 M HCl, covered with lids, and incubated for 12 hours at 55 °C. HCl was decanted from the plates. They were then washed with deionized water (3×, 2 mL), UPW (2×2 mL), ASW (1×, 2 mL), and stored containing 2 mL of ASW for 4-7 days prior to use in cell culture.

Cell culture and treatment:

Micromeres were isolated as described in section 2.1.5. Cells were seeded at a density of ~100,000 cells per glass bottom dish. Cells were washed and cultured in the media of choice to the desired stage of development as described in section 2.1.5.

Fixation:

For gradual fixation, half of the culture media was removed, an equivalent volume of 4% (v/v) PFA in ASW was added, and cells were incubated for 3 min. In a second step, all culture media were removed, an equivalent volume of 4% (v/v) PFA in ASW was added, and cultures were incubated for 25 min at 15 °C. Cultures were then washed with ASWGPS (2×, 2 mL). Washes of any one individual plate were separated by 3-5 min.

Residual fixative was quenched by incubating the cells in 2 mL of 300 mM glycine in ASW for 5 min at 15 °C. Cultures were then washed with ASWGPS (2×, 2 mL).

Permeabilization:

Cultures were permeabilized by incubating in 0.3% (w/v) saponin in ASW for 15 min at 15 °C. Cultures were then washed with 0.05% (w/v) saponin in ASWGPS (2×, 2 mL) (note that saponin permeabilization is reversible, so media used after this step was supplemented with 0.05% (w/v) saponin).

Phalloidin staining:

The phalloidin stock solution was allowed to reach room temperature and was diluted 1:40 by adding 5 µL of the phalloidin stock to 195 µL 0.05% (w/v) saponin in ASW. All media were removed from the cultures and 200 µL of the working phalloidin solution were gently layered on top of the cells. Cultures were incubated for 25 min at 15 °C in the dark and then washed with ASWGPS (2×, 2 mL).

Antibody staining:

Media were removed from the cultures and 200 µL of 0.3% (w/v) BSA in 0.05% (w/v) saponin in ASW were gently layered onto each plate. Cultures were incubated in this solution for 60 min at 15 °C to block nonspecific antibody binding and were then washed with 0.05% (w/v) saponin in ASWGSP (3×, 2 mL). The 6a9 solution was diluted 1:10 in 0.3% (w/v) BSA in 0.05% (w/v) saponin in ASW. All media were removed from the cultures and 200 µL of the working antibody solution were gently layered onto each plate. Cultures were incubated overnight at 4 °C and then washed with 0.05% (w/v) saponin in ASW (3×, 2 mL). A working solution of goat anti-mouse-CF®488 was prepared by diluting the antibody stock solution 1:500 in 3% (w/v) BSA in 0.05% (w/v) saponin in ASW. Media were removed and 200 µL of this solution were gently

layered on top of each plate. Cultures were incubated in the dark for 1 hr at 15 °C and washed with ASWGSP (3×, 2 mL).

Nuclei counterstaining:

Cell nuclei staining with Hoechst does not require permeabilized membranes and was typically performed last, after staining with other fluorophores. A working solution of 5 $\mu g \cdot mL^{-1}$ Hoechst 33342 was prepared by diluting 100 µL of the Hoechst stock solution in 2 mL ASW. Using a pipette, media were removed from cell cultures and 2 mL of the Hoechst 33342 working solution were gently layered on top of the cells. Cultures were incubated in the dark for 5 min at 15 °C and washed with ASWGPS (1×, 2 mL).

Fixed and stained cell cultures were stored at 4 °C in the dark for up to 24 h before imaging; same day imaging was preferred in most cases.

Imaging:

Cell cultures were imaged using standard light microscopy techniques, using bright field illumination (BF), polarized light (pol), differential interference contrast (DIC), and fluorescence contrast. Polarized light was particularly useful if interested primarily in the biomineral since the single crystalline granules and spicules were birefringent. DIC resolved cells and filopodia well. Fluorescence contrast highlighted specific molecules, such as membrane or cytoskeleton elements stained with fluorescently conjugated dyes. Confocal fluorescence microscopy was usually preferred over widefield because it allowed higher resolution imaging with less background fluorescence, enabling capture of both precise single z-axis planes and z-stacks. In most cases, imagine using several illumination modes was performed for each image frame to collect different types of data. In the examples given in this chapter section, PMCs and spicules

were clearly resolved using BF illumination (Figure 2.3A,C). Nuclei stains such as Hoechst 33342 allowed distinguishing individual cells in the masses of membrane-fused PMCs (Figure 2.3B,D). Staining for actin (Figure 2.3B) or MSP-130 (Figure 2.3D) revealed microscopic features such as submicron-thick filopodia.

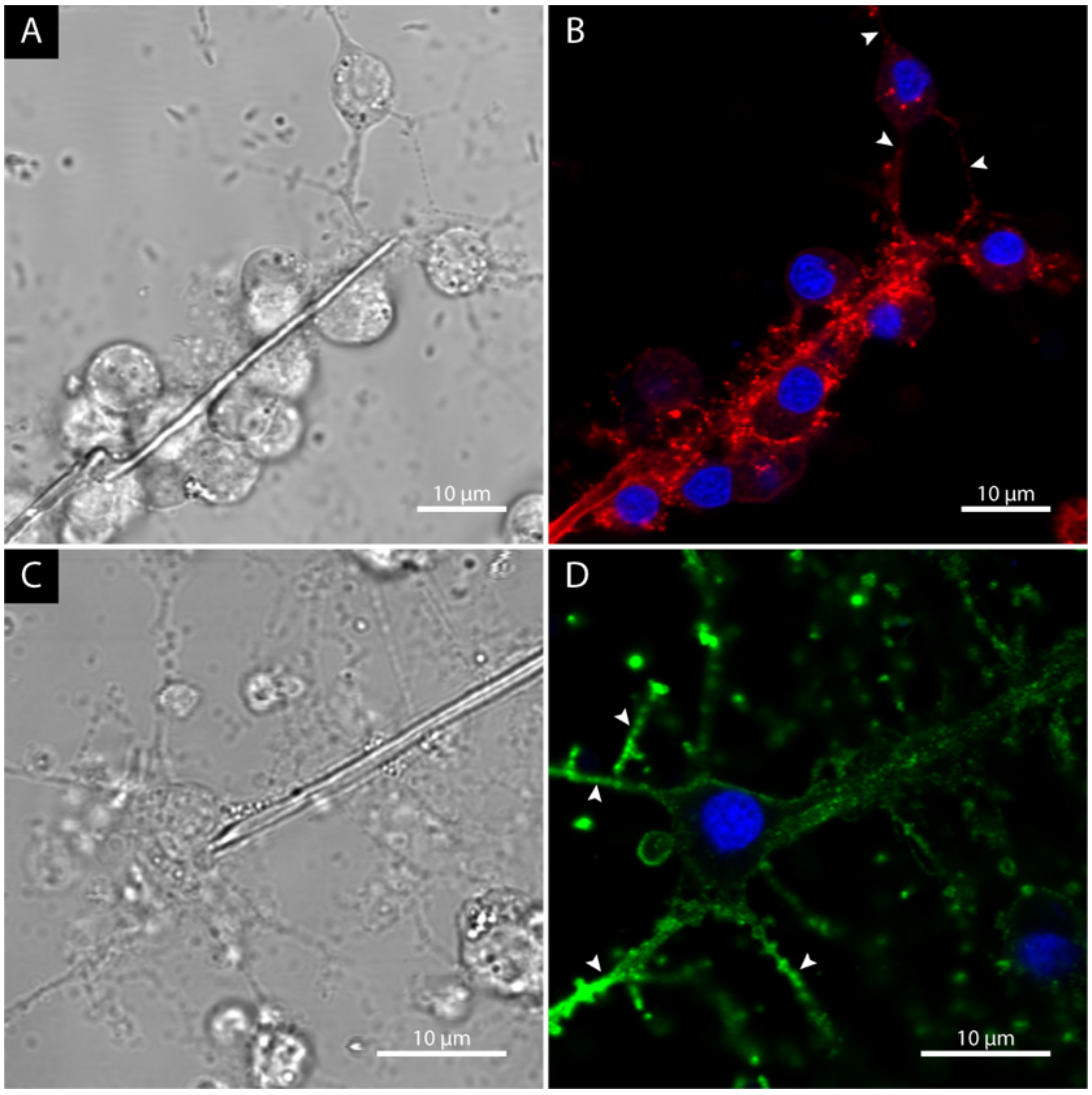

Figure 2.3. Examples of fluorophores used successfully to image microscopic structures in PMCs. (A-B) PMCs stained with phalloidin-CF®568 (red) and Hoechst 33342 (blue). (C-D) PMCs stained with 6a9 and goat anti-mouse-CF®488 (green) and Hoechst 33342 (blue). (A,C) are BF illumination, (B, D) are fluorescence channels. Filopodia (B,D, white arrowheads) are resolved by both stains.

2.3. Transmission Electron Microscopy of Primary Mesenchyme Cell Cultures

2.3.1. Background and overview

The dramatic morphogenetic events during the epithelial-mesenchymal transition (EMT) in early development in the sea urchin embryo made it an attractive target for early ultrastructural studies using transmission electron microscopy (TEM).[90-94] Research driven by developmental and cell biological questions, specifically the ingression of PMCs, their adhesion to and migration on the basal lamina, and the formation of a syncytium by cell fusion, continued to fuel investigation of PMC ultrastructure *in vivo*.[95-98]

Rising interest in structural and mechanistic aspects of biomineralization then shifted focus toward spiculogenesis in PMCs,[99, 100] and calcification by other cell types in adult sea urchins.[101-104] Around the same time, careful analysis of the behavior, structure, and skeletogenesis *in vitro* established cultured PMC as a powerful model system. For instance, the role and localization of MSP-130, the aforementioned cell surface glycoprotein involved in calcium transport, has been explored by immuno-TEM.[105]

Vesicular trafficking of proteins and mineral building blocks has been an area of interest since the very beginning.[91] The SM50 and the SM30 family of spicule matrix proteins travel along the secretory pathway and are delivered to the spicule compartment.[106] Interestingly, they show differential localization within the spicule compartment.[106, 107] More recently, uptake and transport of calcium, membrane-impermeable dyes, and of several proteins in the plasma membrane (including MSP-130) to the spicule compartment has been demonstrated using a combination of fluorescence microscopy and ultrastructural analysis by focused ion beam-scanning electron microscopy (FIB-SEM) at cryogenic temperatures.[87, 88]

Taken together, there is a long history and strong present interest in ultrastructural analysis of PMCs by electron microscopy. With functional immunolabeling of specific molecules being well established for TEM, and because of its wide availability, here sample preparation for conventional TEM is the focus. However, cryo-fixation and cryo-imaging arguably reveal any sample in its most pristine state and may well be required for projects where preservation of very delicate structures or highly soluble materials is essential.

Sample preparation for ultrastructural TEM involves fixation, staining (post-fixation), dehydration, resin embedding, and sectioning. Optionally, sections can be stained further. Chemical fixation is generally straightforward, but care must be taken to match the osmotic strength of the fixative to that of seawater (~1,000 $mOsm \cdot L^{-1}$).

Biominerals easily dissolve during these processing steps and in the resulting TEM micrographs there simply remains an "empty" (resin-filled) space with the same morphology as the biomineralized structure. In most instances, de-mineralization is favorable, as hard and brittle biominerals shatter easily during ultramicrotomy and tend to tear thin sections. Fixation in the presence of chelators such as EDTA, EGTA, or a slightly acidic pH is usually sufficient to dissolve spicules deposited by PMCs *in vitro*. However, with proper attention to pH and calcium concentration in all aqueous solutions, it is possible to preserve the biomineral. To avoid loss of mineral during ultramicrotomy, it is advisable to float sections on a $CaCO_3$-saturated solution or anhydrous glycerol. In the protocol discussed herein, spicules dissolve completely.

Cryofixation followed by freeze-substitution can improve sample preservation

and prevent loss of highly soluble organic and inorganic components.[101] While cryo-fixation of whole embryos requires high pressure freezing, PMCs cultured directly on TEM grids can be plunge frozen as well.[105] Vitreous water is then exchanged for an organic solvent supplemented with fixative and stains at low temperature during freeze substitution.[102] Finally, the solvent is replaced with a resin and the resin is cured. Further processing by ultramicrotomy can be carried out at ambient temperature. Unfortunately, sectioning of such samples can be problematic because of the hard-soft contrast between the embedded soft tissue and the biomineral. Sectioning and imaging of cryo-frozen samples by cryo-FIB/SEM,[88] or by the cryo-TIGM process developed in the Joester group[108, 109] circumvents these issues and offers supreme sample preservation, albeit at the price of reduced contrast and the inability to functionally label samples.

2.3.2. Materials

Chemicals and disposables:

Unless otherwise noted, all reagents were stored at room temperature (22 °C). Ethanol (200 proof) (Decon Laboratories Inc., King of Prussia, PA); NaCl (≥99.5%), $MgSO_4$ (anhydrous, ≥99.5%), $CaCl_2 \cdot 2H_2O$ (≥99%), Na_2SO_4 (anhydrous, ≥99%), $MgCl_2 \cdot 6H_2O$ (≥99%), KCl (≥99%) (Avantor, Radnor, PA); NaOH (≥99.1%), acetone (≥99.5%), paraformaldehyde (PFA, 16% (v/v), EM grade), glutaraldehyde (25% (v/v), EM grade, stored at 4 °C), OsO_4 (4% (v/v), stored at 4 °C), uranyl acetate (≥98%), sodium citrate dihydrate ($Na_3C_6H_5O_7 \cdot 2H_2O$, ≥99%), $Pb(NO_3)_2$ (≥99%) (Thermo Fisher Scientific, Waltham, MA); EMbed 812 resin (EMS, Hatfield, PA).

Nunc™ Thermanox™ coverslips (13 mm diameter round), PES sterile filter units (0.2-µm, 1-L), plastic Petri dishes (29 mm, 90 mm), pipette tips (10-100-µL), serological pipettes (5-

mL) (Thermo Fisher Scientific, Waltham, MA); BEEM® embedding capsules (size 00), formvar-coated copper 150 mesh TEM grids (EMS, Hatfield, PA); Parafilm, Whatman filter paper #4 (Sigma-Aldrich, St. Louis, MO).

Equipment:

Cover slip holder for 9-13 mm cover slips (Tousimis, Rockville, MD); beakers (50-mL), volumetric flasks (10-, 50-mL), pH meter, Lab-Line® model 3608 oven, dewar for liquid nitrogen, cryogenic gloves, hot plate (Thermo Fisher Scientific, Waltham, MA); S4 E stereomicroscope, Ultracut S ultramicrotome (Leica, Allendale, NJ); Ultra 35° diamond knife (DiATOME, Hatfield, PA), single-channel adjustable volume pipettes (20-200-, 100-1,000-µL) (Eppendorf, Hamburg, Germany).

Solutions:

Unless otherwise noted, all aqueous solutions were prepared with ultra-pure water (UPW, $\rho = 18.2\ M{\cdot}\Omega{\cdot}cm$) dispensed by a Barnstead NanoDiamond UF + UV purification unit and stored at room temperature.

The fixative of 2% (v/v) PFA and 2.5% glutaraldehyde was prepared in ASW. A solution of 2% (v/v) OsO_4 was prepared in UPW. A solution of 2% (w/v) uranyl acetate was prepared by dissolving 0.3 g uranyl acetate in 15 mL UPW. Acetone solutions of 30% (v/v), 50% (v/v), and 70% (v/v) were prepared in UPW. EMbed 812 solutions of 33% (v/v), 50% (v/v), and 66% (v/v) were prepared in acetone. Degassed H_2O was prepared by boiling 750 mL UPW for 30 min.

Reynold's lead citrate ($C_{12}H_{10}O_{14}Pb_3$) was prepared as follows. 1.33 g of lead nitrate was suspended in 30 mL of degassed H_2O in a 50 mL volumetric flask with a stopper. 1.76 g sodium citrate was added to this suspension and the flask was shaken vigorously for 2 min. The solution

turned milky white and was allowed to stand for 30 min with occasional inversion. 8 mL of 1.0 M NaOH was added, and the solution was mixed slowly by inversion. The solution cleared and was brought to 50 mL with UPW, covered with aluminum foil, and kept in the dark.

Methods

Cell culture and fixation:

Micromeres were isolated as described in section 2.1.5. 13 mm diameter Thermanox® coverslips were placed in the bottom of 29 mm diameter plastic Petri dishes. Micromeres were seeded at a density of approximately 100,000 cells per plate. As described in section 2.1.5. cells were washed and cultured with the media of choice (e.g., 4% HS (v/v) in ASW) to the chosen stage of development.

At the desired time after fertilization, plates were fixed, taking care to keep the cells submerged in some liquid, as meniscus forces can strip the cells off the plate. Media was gradually replaced with freshly made fixative: 1/3 of the volume of media were removed, then fixative was added equal to the volume removed by pipetting down the side of the plate. The plate was swirled gently to mix. Next, two-thirds of the media were removed and replaced with an equal volume of fixative. Finally, all media were removed from the plate and replaced with 3 mL fixative. Cells were incubated in fixative for 1 h at 15 °C and then stored in fixative at 4 °C overnight until processing for TEM.

Processing for TEM:

Coverslips were removed from their plates and stacked in a coverslip holder. The holder was placed in a 10-mL glass beaker. Coverslips were washed with deionized water (3×), incubating in the wash solution for 1 h each time. After the final wash, the holder was transferred

a 10-mL glass beaker containing 8 mL 2% aqueous OsO_4 and incubated 1 h at room temperature. Samples were washed with deionized water (3×), incubating in the wash solution for 1 h each time. To dehydrate samples, the sample holder was transferred to a beaker containing 30% (v/v) acetone in deionized water and allowed to incubate for 30 min. This step was repeated with 50% (v/v) acetone once, 70% (v/v) once, 90% (v/v) once, and 100% (v/v) twice

To infiltrate samples with EMbed 812 (the resin), the sample holder containing the coverslips was transferred to a 10-mL glass beaker containing a freshly made solution of 33% (v/v) resin in acetone and incubated for 1 h. This step was repeated using freshly made solutions of 50% (v/v) resin for 2 h, 66% (v/v) overnight, and 100% (v/v) for 1 hr, each time transferring the samples to a new beaker. The final step was repeated three times.

Coverslips were placed, cell side up and on top of paper labels, in a Petri dish (90 mm, plastic) lined with aluminum foil. BEEM® embedding capsules (size 00) were filled with fresh resin and rapidly inverted onto each of the coverslips. The Petri dish was transferred into an oven and cured at 60 °C for 24 h.

The blocks were submerged in liquid nitrogen for several minutes. Wearing cryo-gloves, the blocks were removed from liquid nitrogen and coverslips were immediately snapped off by hand.

Regions of interest were identified using a stereomicroscope. The block face was trimmed for sectioning using a razor blade. Ultra-thin sections were created using a Leica Ultracut S ultramicrotome with an Ultra 35° diamond knife. Sections floated on a water bath and picked up on formvar-coated copper 150 mesh grids.

If post-staining was desired, grids were floated, section side down, on 50-µL drops of 2% (w/v) uranyl acetate on Parafilm for 10 min. Grids were then rinsed with deionized water. If lead staining was desired, a plastic Petri dish was prepared containing 5 NaOH pellets at the periphery of the plate to create a CO_2-free atmosphere. The grids were floated, section side down, on 50-µL drops of Reynold's lead citrate on Parafilm within the dish for 7 min. Excess moisture was wicked away using filter paper and grids were washed with CO_2-free deionized water and air dried.

Imaging:

Images were collected on a JEOL 1230 TEM operating at 80 kV with brightfield contrast, and images were collected using a Hamamatsu ORCA side-mounted camera and a bottom mount Gatan Orius CCD camera. PMC cultures prepared as described in this chapter section displayed resin-filled holes left behind by dissolved spicules, surrounded by the thin membranous spicule compartment (Figure 2.4). TEM resolution enabled imaging of submicron features, such as residual organic material left behind after spicule dissolution (Figure 2.4B,D).

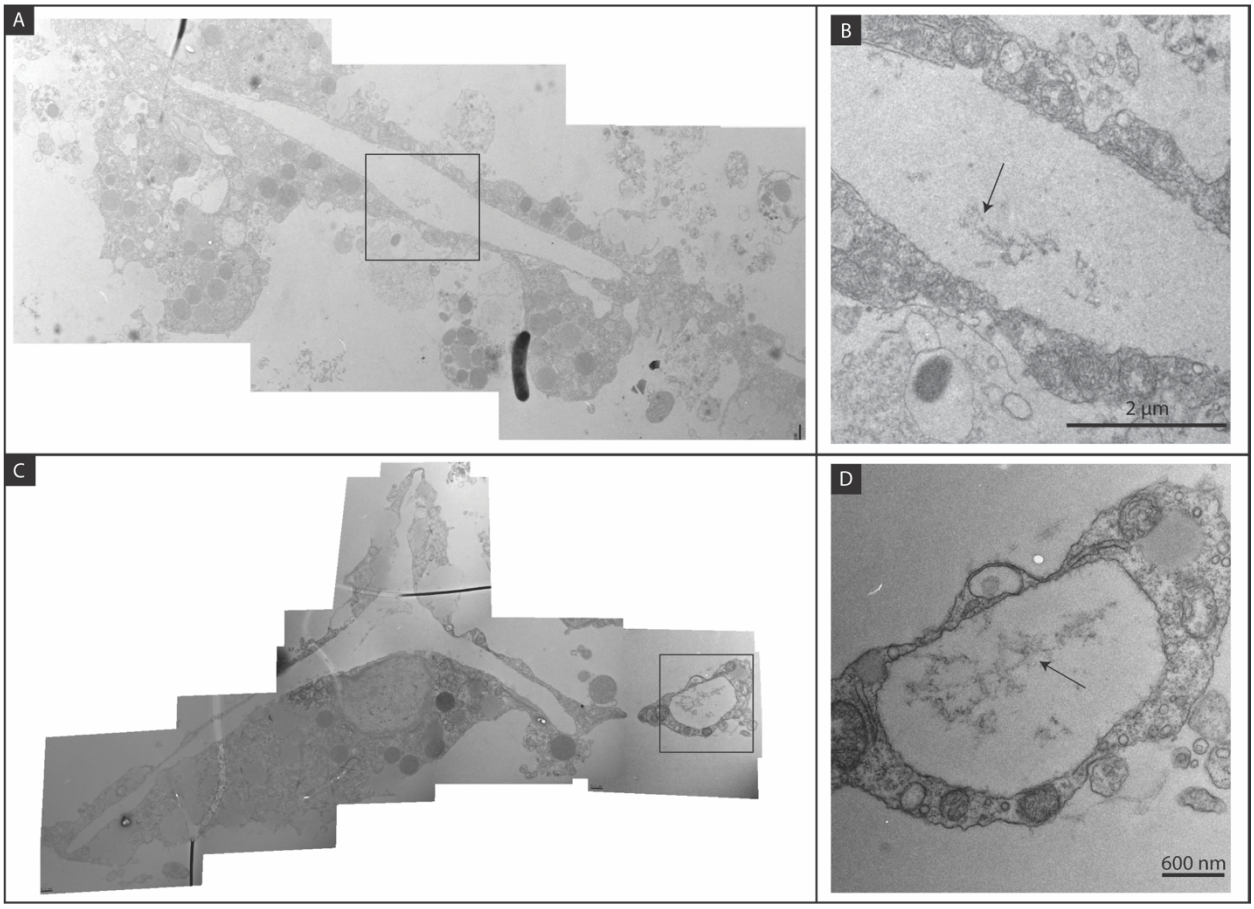

Figure 2.4. TEM images of PMC cultures. PMCs were incubated in (A-B) 4% (v/v) HS in ASW or (C-D) 4% (v/v) HS in ASW supplemented with 1.2 µg·mL^{-1} rVEGF, from 26 hpf and fixed at 56 hpf. Residual organic material (B,D, black arrows) indicated. Images taken using BF contrast. Reproduced from reference 110.[110] For more information on rVEGF treatment of PMCs, refer to Chapter 3.

2.4. Transcriptomic Analysis of Primary Mesenchyme Cell Cultures

2.4.1. Background and overview

In an early breakthrough, researchers extracted mRNA from micromere and embryo cultures and demonstrated that micromere mRNA is distinct from that of the 16-cell embryo.[111] Later, another group created a cDNA library from polyadenylated RNAs isolated from PMCs *in vitro* and discovered a number of transcripts specific to PMCs.[112] Transcripts followed similar temporal expression patterns, thus providing further evidence of a unique skeletogenic transcriptome and regulation by transcript abundance.[113] Later, researchers extracted mRNA

from PMC cultures, generating a library of expressed sequence tags (ESTs).[114] The sequencing of the genome of *S. purpuratus* transformed the field and was quickly followed by the first transcriptomic analysis of the embryo in different developmental stages.[115] A transcriptome of PMC isolated by FACS followed soon after but required an extraordinary effort.[76] We have recently completed an RNA-seq analysis, comparing PMC treated *in vitro* with 4% (v/v) HS in ASW, resulting in predominantly linear spicules, to PMC treated with 4% (v/v) HS + 1.2 μg·mL^{-1} rVEGF, resulting in triradiates (unpublished). As shown below, the amount of effort required for two treatment groups and four timepoints was miniscule compared to the FACS experiment by Barsi and colleagues. However, while costs have come down considerably over the last 5 years, they are still substantial.

This protocol is quite straightforward and uses a readily available kit optimized for small samples. In experiments we performed, a yield of 2-3 μg of total RNA per 100,000 cells seeded was typical. RNA integrity was typically very high (RIN = 10). The amount of RNA recovered was sufficient to run many qPCR experiments (after reverse transcription to cDNA). At the current state of technology, 250 ng to 1.5 μg total RNA is sufficient to perform an RNA-seq analysis.

2.4.2. Materials

Chemicals and disposables:

NucleoSpin RNA XS Kit (Macherey-Nagel, Duren, Germany); pipette barrier tips (200-μL), RNase-free Eppendorf tubes (1.5 mL) (Midwest Scientific, Valley Park, MO).

Equipment:

Single-channel adjustable volume pipettes (20-200 µL) (Eppendorf, Hamburg, Germany); SP Vortex Mixer (Baxter, Deerfield, IL); vacuum aspirator with trap (Sigma-Aldrich, St. Louis, MO).

2.4.3. Methods

RNA isolation:

After culturing PMCs in the appropriate medium to the desired stage of development as described in section 2.1.5. all cell culture media were removed by suction (incomplete removal of cell culture medium reduces effectiveness of lysis buffer). 200 µL of lysis buffer were directly added to each plate and plates were swirled. Using a 200 µL pipette, the buffer was aspirated and expelled several times to dislodge cells from the bottom of the plate. The solution of buffer and cells was transferred to an RNase-free 1.5 mL Eppendorf tube and vortexed vigorously for 2-5 s. RNA was isolated according to the manufacturer's instructions.

2.5. Conclusions

Herein we have developed and refined a versatile technique for the mass generation and culture of sea urchin embryo micromeres and PMCs. When followed correctly and under optimal conditions, this protocol generated millions of micromeres and thus provided massive amounts of data per run, enabling large-scale experiments with isolated biomineralizing cells. In addition, we have developed methods for preparation of isolated PMCs cultured *in vitro* for fluorescence microscopy, TEM, and transcriptomic analysis. PMCs prepared for fluorescence microscopy as described in this chapter were successfully stained with nuclear dyes, phalloidin conjugates, and antibodies specific for macromolecules such as membrane proteins. The technique has proved to

be as robust and consistent across animal batches as the method of micromere isolation and is certainly amenable to adaptation with other fluorescent dyes not discussed in this dissertation. The method of preparation of *in vitro* cultured PMCs for TEM enabled high resolution imaging of micro- and nanofeatures associated with the spicule mineralization process and was compatible with the typical TEM contrast stains. Furthermore, the transcriptomics approach developed here offers a relatively simple way to collect mass transcripts of PMCs grown *in vitro*. Transcriptome data collected from cell cultures complements imaging data and provides more functional explanations of observed changes in cell phenotype or biomineral morphology.

Overall, the methods of isolating micromeres and culturing, experimenting with, and characterizing PMCs detailed in this chapter form a platform to dissect a fundamental biomineralization process across length scales. It is expected that they can be adapted for projects across fields, ranging from developmental biology to materials science and engineering, where examining the biomineralizing cells of the sea urchin embryo is of key interest. In addition, these techniques constitute the basis of experimentation within this thesis and will provide a useful reference from this chapter on.

Chapter 3. VEGF-Mediated Branching Morphogenesis

3.1. Introduction

The formation of the sea urchin embryo's endoskeletal spicule is a remarkable case of biology effecting a complex single crystal growth process. As described in Chapter 1. after ingression into the blastocoel in an epithelial-to-mesenchymal transition (EMT) during the late gastrula stage, the primary mesenchyme cells (PMCs) gather into two mirror symmetric ventrolateral clusters (VLCs), fuse their membranes to form two syncytia, and deposit one calcite granule in each syncytium.[37, 38] The granules elongate along each of the three *a*-axes of calcite to become the triradiate rudiments. One of the triradiate arms ceases growth as the midventral rod, another continues growing in the *a*-axis as the postoral rod, and the last switches directions 90° into the *c*-axis of calcite as the body rod. Later branching into the *c*-axis completes the mature pluteus spicule. Spicule growth occurs within an enclosed space delineated from the external environment[99] and quite rapidly (5-13 $\mu m \cdot h^{-1}$).[116]

The spicule's intricate species-specific shape stems from the PMCs' ability to choreograph precise changes in crystallography at specified points in development. The micromere-PMC gene regulatory network is autonomous,[37, 52] so the PMCs retain their capability to form spicules when isolated and cultured *in vitro*.[65] However, PMCs raised *in vitro* in the presence of typical culture media such as horse serum (HS) produce simple linear spicules elongated along the *c*-axis of calcite rather than the complex branching spicules elaborated within the embryo. It follows that some aspects of spicule formation (e.g., *a*-axis growth) require signaling cues from other cells within the embryo. This hypothesis was heavily supported by studies demonstrating that PMCs microsurgically transplanted between embryos will migrate

along the blastocoel wall and form normal spicules, indicating that biochemical signaling within the embryo guides PMC behavior.[58, 77]

The ectoderm was later singled out as playing a particularly intimate role in regulating PMC migration and skeletogenesis. Treatment with $NiCl_2$ (which ventralizes the embryo, thus moving the ectoderm cells from their normal locations) resulted in rearranged PMC patterning and excessive formation of triradiate spicules,[56, 117] as well as altered PMC expression of the gene for spicule matrix protein SM30.[116] Later work using *in situ* hybridization to visualize gene expression revealed that during spiculogenesis, expression of specific ligands in the ectoderm, including fibroblast growth factor (FGF) and vascular endothelial growth factor (VEGF), is mirrored by expression of the corresponding receptor proteins in the PMCs, providing further evidence of ectoderm regulation of spicule formation.[57, 60] FGF signaling was shown to be upstream of SM30 and SM50 in PMCs and knockdown of FGF expression in the embryo disrupted PMC patterning and spicule formation,[60] although this effect was inconsistent between species and research groups.[67] In the case of VEGF, overexpression resulted in extraneous spicule branching whereas knockdown halted PMC migration and spicule formation and altered the expression of many biomineralization genes.[57, 67] More recently, TGF-β signaling via receptor Alk4/5/7 and ectoderm-derived ligand Univin was shown to be critical for anterior skeleton formation in *L. variegatus*.[62]

We have previously demonstrated that *in vitro* cultured PMCs respond to increasing concentrations of recombinant VEGF (rVEGF) by producing linear, branched, and finally triradiate spicules closely resembling those of the late gastrula.[71] This remarkable discovery established that VEGF acts as a molecular switch controlling *c*- and *a*-axis crystallographic

orientation, adding it to the very brief list of known proteins, such as Starmaker in the zebrafish otolith[118] and N16 and Pif in the pearl oyster shell,[119, 120] inducing a specific effect on biomineral formation (although unlike in those cases, VEGF is a signaling molecule and not a biomineralization protein, so the control is *indirect*). VEGF concentration is clearly a lever exerting control over spicule morphology, but it remains a question if the VEGF-VEGF receptor (VEGFR) signaling system contains other such levers.

Heterogeneous distribution of growth factors, in the form of concentration and spatiotemporal gradients, is well-documented across biological phyla as a means to guide development,[121, 122] so it is logical to assume that the sea urchin embryo also tightly controls the density, location, and timing of growth factors to effect morphogenic events such as spicule formation. In fact, prior work has indeed found spatial and temporal distribution of growth factors in the sea urchin embryo to be heterogeneous. For example, expression of FGF begins when the PMCs ingress into the blastocoel, peaks during the gastrula stage in the regions of ectoderm near the VLCs and spicule branching, and largely shuts off by the mid pluteus stage.[60] In the case of VEGF, expression begins at the swimming blastula stage in the ectoderm and is maintained at relatively constant expression until the pluteus stage, when it drops off.[57]

As previously stated, we have already established that varying VEGF concentration alters spicule morphology, so we opted to move onto other control levers such as timing and localization. Inspired by the aforementioned studies demonstrating that the timing of VEGF signaling is tightly controlled in the embryo,[57] we decided to examine the temporal aspect of the VEGF-VEGFR signaling system, that is, to determine if the timing of VEGF is another mechanism to control spicule morphogenesis. We took advantage of our *in vitro* PMC culture

system combined with purified rVEGF, pharmacological inhibitors, and optical microscopy to explore the relation between the timing of VEGF signaling and spicule morphology. We found that the temporal dimension is crucial for spicule branching morphogenesis, solidifying it as a major lever exerting control over spicule formation.

3.2. Results and Discussion

3.2.1. VEGF concentration series

Before we could explore the temporal distribution of VEGF as a potential lever to control spicule growth, we needed to calibrate our purified rVEGF. That is, we needed to find the threshold rVEGF concentration that would cause the PMCs to form triradiate spicules (viz., the concentration of rVEGF that induces *a*-axis growth). To assay rVEGF concentration vs. spicule morphology, we incubated cell cultures from 26 hpf in 4% (v/v) HS or 4% (v/v) HS supplemented with an ascending concentration series of rVEGF. As expected, we found that incubation with 4% (v/v) HS alone caused the PMCs to form majority linear spicules (Figure 3.1A), so we used it as the *c*-axis growth culture medium. Supplementing the media with 0.4 $\mu g \cdot mL^{-1}$ or 0.8 $\mu g \cdot mL^{-1}$ VEGF caused the PMCs to form branched spicules with some *a*- and *c*-axis growth (Figure 3.1B-C). Supplementing the media with 1.2 $\mu g \cdot mL^{-1}$ rVEGF induced the PMCs to form almost exclusively triradiate spicules (Figure 3.1D), establishing this rVEGF concentration as the threshold to induce *a*-axis growth in HS media. By exchanging between HS or HS supplemented with this threshold concentration of rVEGF, a high degree of VEGF-VEGFR signaling corresponding to triradiate formation could be turned on and off, thus theoretically enabling switching the PMCs between *a*- and *c*-axis growth modes at different time points.

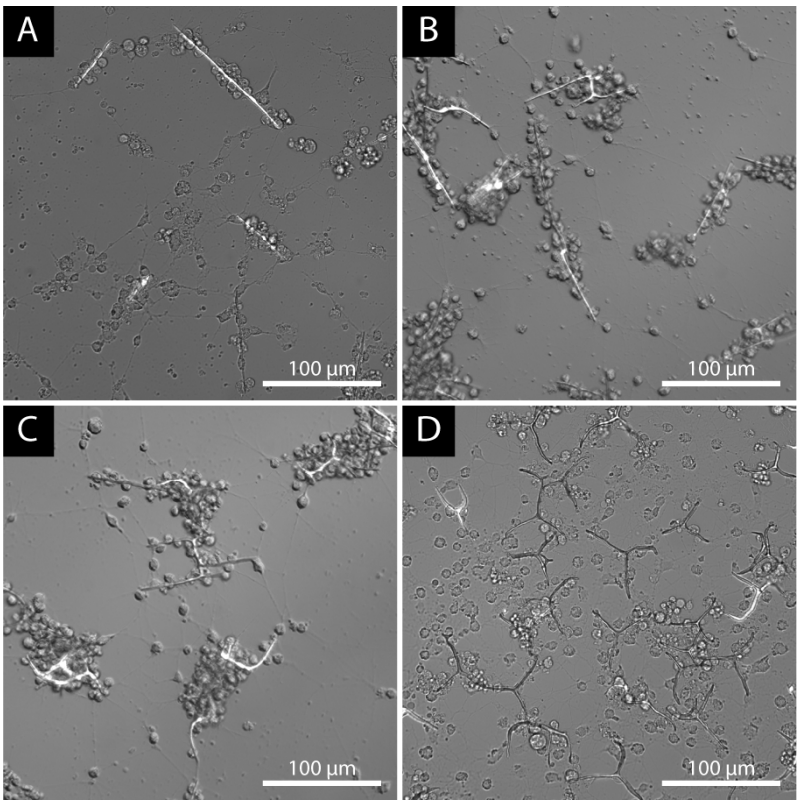

Figure 3.1. Threshold rVEGF concentration for triradiate formation in PMC cultures treated with HS. Cultures were incubated from 26 hpf to 56 hpf with (A) 4% (v/v) HS or 4% (v/v) HS supplemented with (B) 0.4 µg·mL^{-1} rVEGF, (C) 0.8 µg·mL^{-1} rVEGF, and (D) 1.2 µg·mL^{-1} rVEGF. Imaged at 56 hp; (A, D) overlays of BF and pol; (B-C) overlays of DIC and pol.

Although HS always caused PMCs to produce majority linear spicules, spicule branching within PMC cultures treated with HS varied from batch to batch and was not exceedingly rare. Exchanging HS and HS supplemented with rVEGF was ideal for experiments comparing large relative switches in *a*- and *c*-axis growth modes, but for examining more minute differences in the degree of VEGF signaling and resulting spicule shape, we needed another serum that would induce lower background levels of spicule formation and branching. We chose to use fetal bovine serum (FBS) as the base media for these experiments, because by itself it induces very little spicule formation and almost never results in branched spicules.[71] To calibrate rVEGF concentration vs. spicule morphology in FBS, we incubated cell cultures from 26 hpf in 4% (v/v) FBS supplemented with an ascending concentration series of rVEGF. The control specimens

incubated in only 4% (v/v) FBS formed a small number of long linear spicules (Figure 3.2A). Supplementing the media with 0.2 $\mu g \cdot mL^{-1}$ rVEGF resulted in an increased density of linear spicules that were also shorter than those of the control plates (Figure 3.2B). As the concentration of rVEGF was increased to 0.4 $\mu g \cdot mL^{-1}$, the spicules were still dense and linear (Figure 3.2C). 0.8 $\mu g \cdot mL^{-1}$ rVEGF was observed as the threshold concentration to induce significant branching (Figure 3.2D). Increasing the rVEGF concentration to 1.2 $\mu g \cdot mL^{-1}$ rVEGF did not result in a significant change from 0.8 $\mu g \cdot mL^{-1}$ rVEGF (Figure 3.2E). For 2.8 $\mu g \cdot mL^{-1}$ rVEGF, the overwhelming majority of spicules were triradiates (Figure 3.2F), so this concentration was determined to be the threshold rVEGF concentration that induces the highest degree of *a*-axis growth in FBS media.

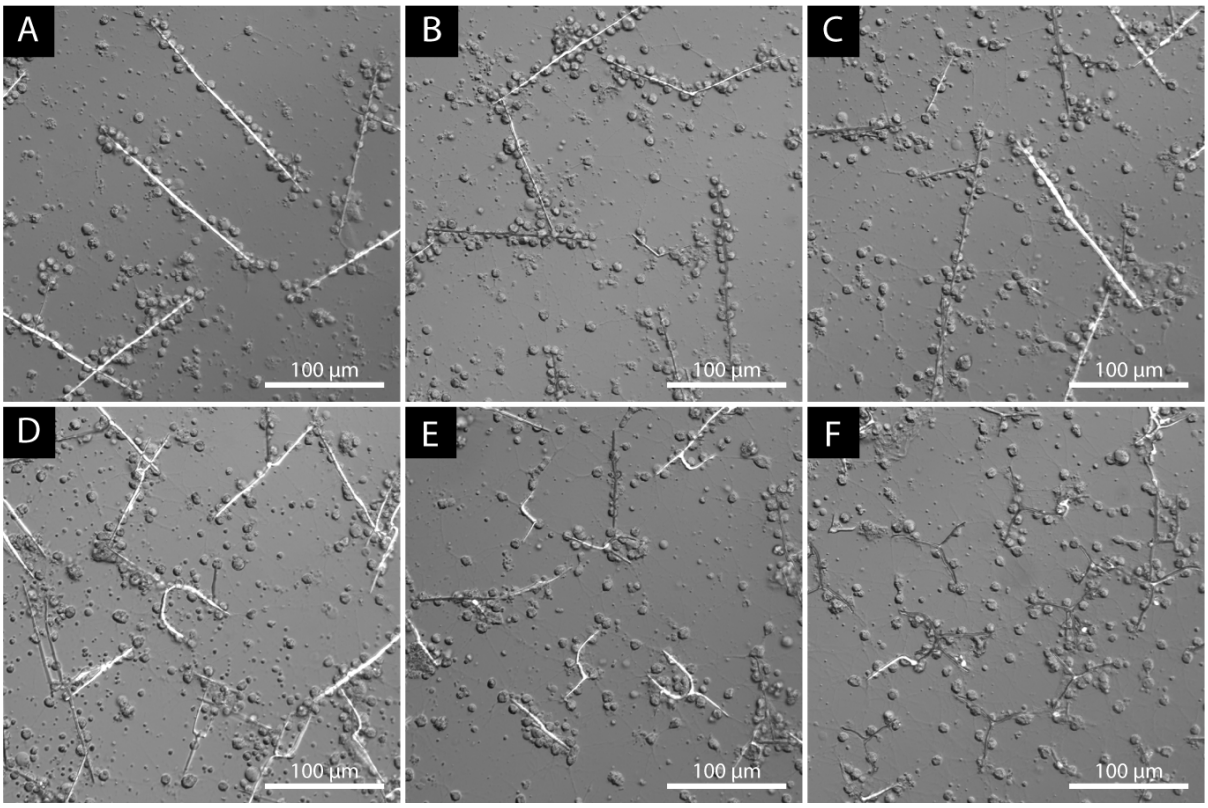

Figure 3.2. Concentration series for rVEGF treatment of PMCs. Cultures were treated from 26 hpf to 56 hpf with (A) 4% (v/v) FBS or 4% (v/v) FBS supplemented with (B) 0.2 $\mu g \cdot mL^{-1}$, (C) 0.4 $\mu g \cdot mL^{-1}$, (D) 0.8 $\mu g \cdot mL^{-1}$, (E) 1.2 $\mu g \cdot mL^{-1}$, and (F) 2.8 $\mu g \cdot mL^{-1}$. Imaged at 56 hpf (frames are overlays of DIC and pol).

In the rVEGF concentration assays for HS and FBS, we validated results first observed by Knapp *et al*., i.e., a shift from linear to branching and triradiate spicule shape with increasing rVEGF concentration.[71] As an experimental aside, we note that we achieved this result with rVEGF concentrations that were ~100 times lower. A possible reason for this discrepancy is that instead of the rVEGF-expressing bacterial lysate they used, we used purified rVEGF. This finding demonstrates the experimental superiority of using purified rVEGF in PMC cultures.

3.2.2. Time series: switching VEGF signaling on and off

After calibrating our purified rVEGF in culture media, we had a means to turn VEGF signaling on. To thoroughly control the temporal distribution of VEGF signaling, we also needed a means to turn VEGF signaling off. We chose to use the tyrosine kinase inhibitor axitinib, a small molecule that has been used extensively to interfere with tumor angiogenesis.[123] Axitinib has also been successfully used to study VEGF signaling in the sea urchin embryo, and is known to shut down spicule formation in embryos if added to the growth media from fertilization.[67] By introducing rVEGF or axitinib to *in vitro* PMC cultures, we were thus able to turn VEGF signaling on and off during chosen time intervals, allowing complete temporal control over VEGF signaling.

To probe the time-dependence of VEGF signaling, cell cultures were incubated from 26 hpf in 4% (v/v) HS supplemented with rVEGF or were incubated in this medium and later treated with 50 nM axitinib. Control cultures continuously incubated in rVEGF-containing media without inhibitor overwhelmingly formed triradiate spicules (Figure 3.3A). Treatment with axitinib at 48 hpf did not have a significant effect on spicule morphology (Figure 3.3B). In contrast, treatment with axitinib at 38 hpf resulted in a strong loss in triradiate character, with

many branched “h”-shaped and forked spicules forming instead (Figure 3.3C). However, most or half of the crystal growth was still along the *a*-axis. Treatment with axitinib at 32 hpf caused the strongest reduction in triradiate and branched character, as most spicules that formed were linear and branched but had majority *c*-axis growth (Figure 3.3D).

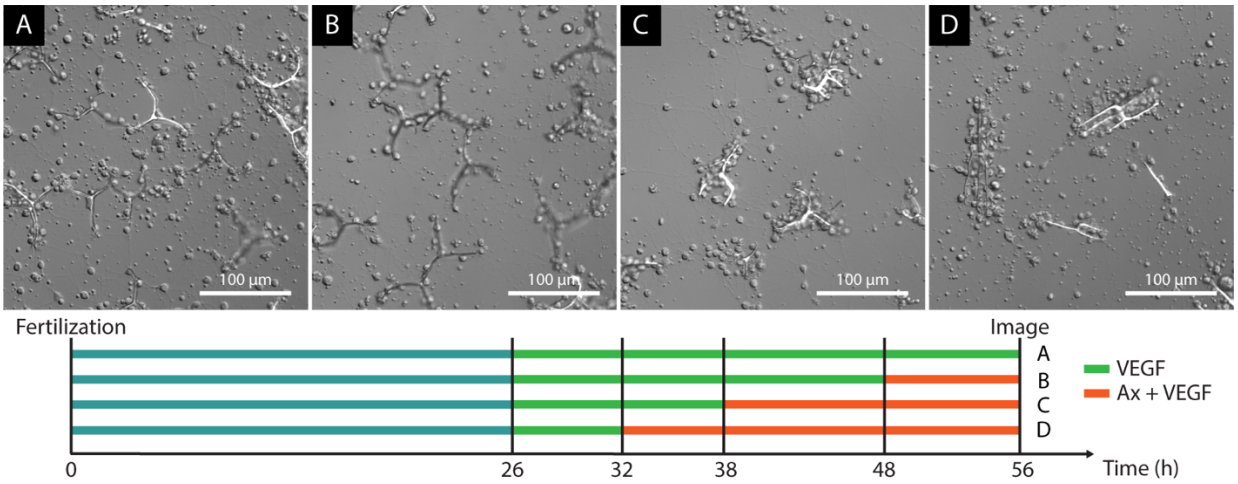

Figure 3.3. Time-dependent inhibition of VEGF-VEGFR signaling reduces spicule branching. Cultures were treated from 26 hpf to 56 hpf with 4% (v/v) HS supplemented with 1.2 µg·mL^{-1} rVEGF (A) continuously or treated with 50 nM axitinib at (B) 48 hpf, (C) 38 hpf, and (D) 32 hpf. Imaged at 56 hpf (frames are overlays of DIC and pol).

It is interesting to compare our results with those of Adomako-Ankomah and Ettensohn, who observed different spicule morphologies depending on when axitinib was added to the culture media.[67] They found that early treatment with axitinib (fertilization to early gastrula stage) completely shut down spicule formation, whereas later treatment (mid gastrula stage onwards) selectively prevented growth of the postoral and anterolateral rods, which requires branching. Our earliest timepoint of axitinib addition (32 hpf) corresponds to the late gastrula stage of the embryo, so our finding that axitinib treatment does not shut down spicule growth, and instead prevents triradiate formation and encourages longitudinal *c*-axis growth, agrees with their results. These data demonstrate that VEGFR inhibition during the mid-late gastrula stage

(i.e., early spicule formation) prevents triradiate formation *in vitro* and later spicule branching *in vivo*, suggesting that continuous VEGF signaling is necessary for sustained *a*-axis growth.

Treatment with a pharmacological inhibitor can affect signaling pathways besides the one being targeted, resulting in indirect changes in observed phenotype. As such, another experiment was designed in which VEGF signaling was lowered without using axitinib by simply switching the media from 4% HS (v/v) supplemented with rVEGF to 4% (v/v) HS without added rVEGF. The results essentially phenocopied the previous experiment that used axitinib, with the cessation of triradiate formation and return to *c*-axis growth becoming more severe with earlier switches to 4% (v/v) HS (Figure 3.4). We can thus conclude that our observed reduction in triradiate formation and *a*-axis growth stems from turning off VEGF signaling and is not due to indirect signaling effects from axitinib.

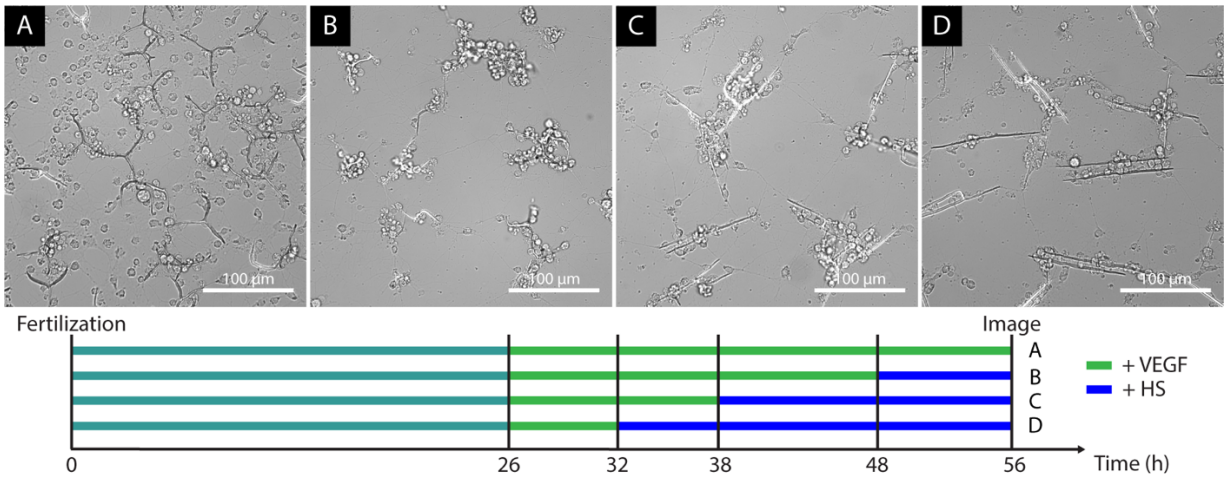

Figure 3.4. Time-dependent removal of VEGF reduces spicule branching. Cultures were treated from 26 hpf to 56 hpf with 4% (v/v) HS supplemented with 1.2 µg·mL^{-1} rVEGF (A) continuously or switched to 4% (v/v) HS without supplemented rVEGF at (B) 48 hpf, (C) 38 hpf, and (D) 32 hpf. Imaged at 56 hpf (frames are overlays of BF and pol).

In a perpendicular set of experiments, we turned VEGF signaling on at selected time points by incubating cell cultures in 4% (v/v) HS and later supplementing the media with rVEGF. Control cultures continuously incubated in 4% (v/v) HS formed overwhelmingly linear

spicules (Figure 3.5A). Cell cultures switched to media supplemented with rVEGF at 48 hpf did not appear significantly different from the control cell cultures other than forming slightly shorter spicules (Figure 3.5B). Cell cultures switched to rVEGF-supplemented media at 38 hpf formed spicules that branched with significant growth in both the *a*- and *c*-axes (Figure 3.5C). Cell cultures switched to media supplemented with rVEGF at 32 hpf formed spicules with primarily triradiate morphology and *a*-axis growth (Figure 3.5D).

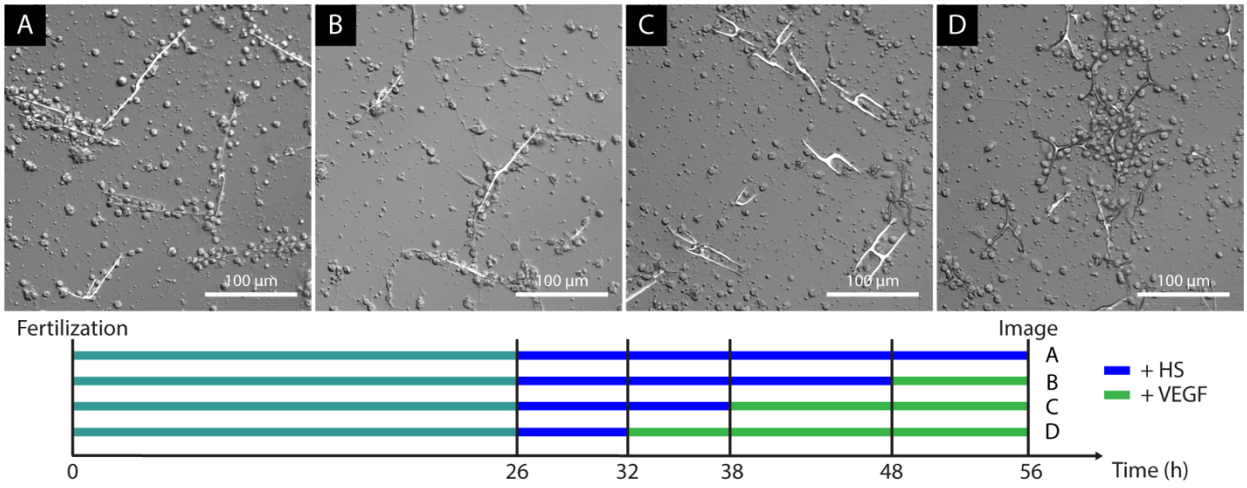

Figure 3.5. VEGF induction of spicule branching is time dependent. Cultures were treated with 4% (v/v) HS (A) continuously or supplemented with 1.2 µg·mL^{-1} rVEGF at (B) 48 hpf, (C) 38 hpf, and (D) 32 hpf. Imaged at 56 hpf (frames are overlays of DIC and pol).

By 56 hpf, the cell cultures switched at 48 hpf to rVEGF-supplemented media had formed spicules that did not differ significantly in shape from the control plates. However, when we imaged again at 76 hpf, we observed many extraneous branches growing off the main body rods of the spicules (Figure 3.6). These “hyperbranched” spicules changed crystallographic direction at a relatively late timepoint, although *a*-axis growth appeared to be unstable since the branchpoints quickly reverted to *c*-axis growth parallel to the main body rod of the spicule. This finding is analogous to prior work that found excessive branching of the pluteus spicule when embryos were induced to overexpress VEGF,[57] so it is curious that we achieved a similar

phenotype by turning VEGF signaling on at a later timepoint rather than by inundating the PMCs with excess VEGF.

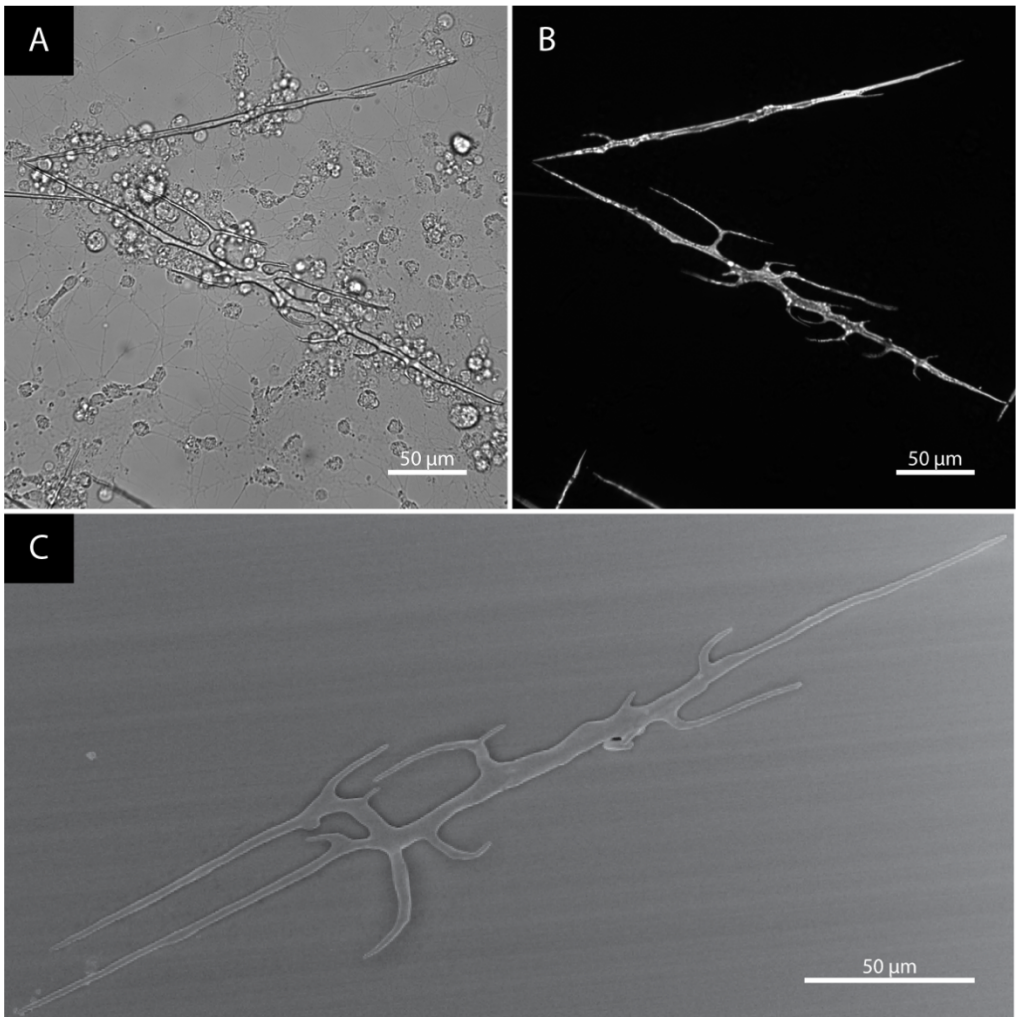

Figure 3.6. Late addition of rVEGF induces extraneous branching ("hyperbranching") on linear spicules. Spicules switched from 4% (v/v) HS to 4% (v/v) HS supplemented with 1.2 µg·mL^{-1} rVEGF at 48 hpf and imaged at 76 hpf. (A) BF illumination, (B) cross-polarized illumination, and (C) secondary electron contrast SEM micrograph.

3.2.3. Dynamics of hyperbranched spicules

The remarkable hyperbranched spicules that formed as a result of delayed VEGF signaling inspired us to simultaneously use the concentration and time levers in the VEGF signaling system. Specifically, we decided to vary the starting concentration of rVEGF and switch to a higher concentration of rVEGF at a later timepoint to determine if we could establish

an even higher degree of control over spicule branching. To do so, we chose FBS supplemented with rVEGF as our culture serum, since as we demonstrated earlier, this media combination affords more precise control over the degree of VEGF signaling and associated spicule branching.

We first sought to reproduce the hyperbranched spicules obtained by supplementing HS with rVEGF at a late timepoint, by switching between FBS media with different concentrations of added rVEGF. We attempted this by incubating PMC cultures from 26 hpf in 4% (v/v) FBS supplemented with 0.4 $\mu g \cdot mL^{-1}$ rVEGF and increasing the rVEGF concentration to 2.8 $\mu g \cdot mL^{-1}$ at 48 hpf; for comparison, in separate plates, we also cultured cells continuously in FBS supplemented with either concentration of rVEGF. Cell cultures incubated in 0.4 $\mu g \cdot mL^{-1}$ rVEGF formed long and linear spicules (Figure 3.7A) whereas cell cultures incubated in 2.8 $\mu g \cdot mL^{-1}$ rVEGF formed branched or triradiate spicules (Figure 3.7B). Cell cultures switched from 0.4 $\mu g \cdot mL^{-1}$ rVEGF to 2.8 $\mu g \cdot mL^{-1}$ rVEGF formed spicules with hyperbranched morphology identical to the hyperbranched spicules we first observed, with many branches sprouting from the main body rods of the spicules (Figure 3.7C-E). We were thus able to successfully induce PMCs cultured in FBS to form hyperbranched spicules, so we could then probe other rVEGF concentration changes.

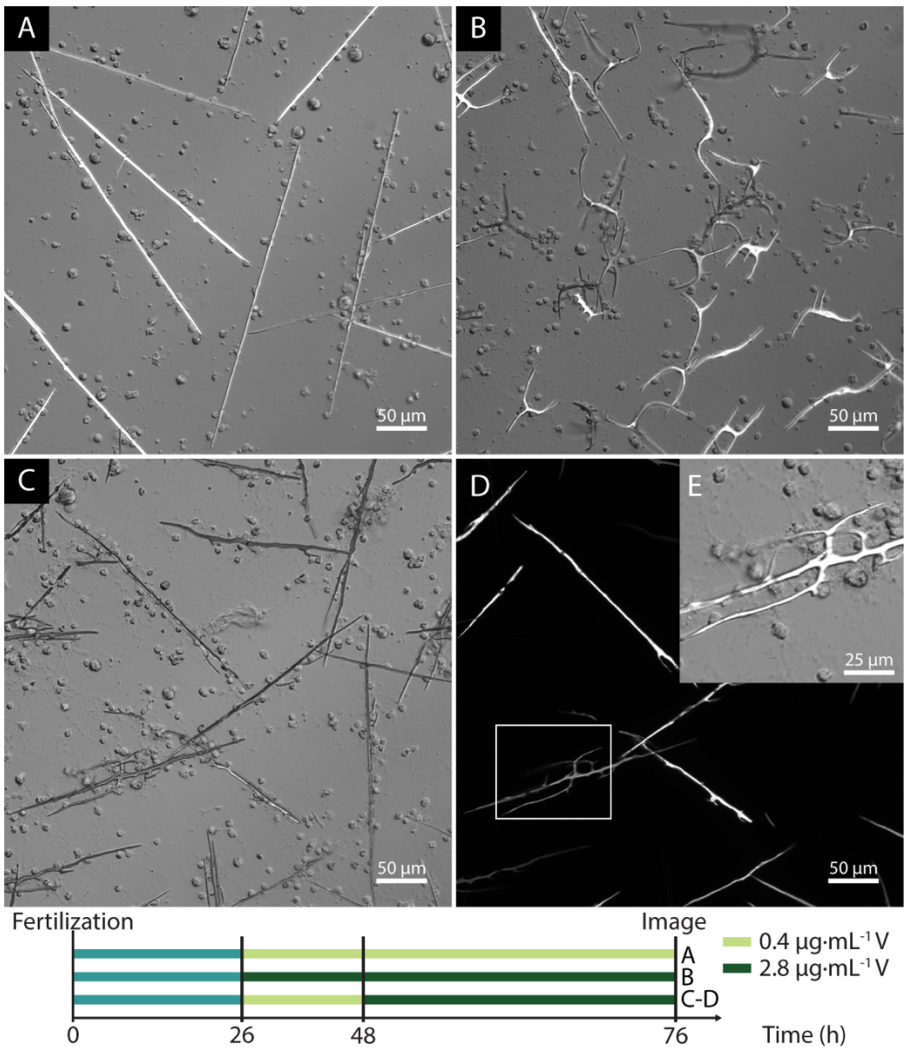

Figure 3.7. Cultures incubated from 26 hpf to 76 hpf in 4% (v/v) FBS supplemented with (A) 0.4 µg·mL^{-1} or (B) 2.8 µg·mL^{-1} rVEGF (V), or (C-E) incubated in 4% (v/v) FBS supplemented with 0.4 µg·mL^{-1} rVEGF from 26 to 48 hpf and 2.8 µg·mL^{-1} rVEGF from 48 hpf to 76 hpf. Images taken at 76 hpf; (A,B,E) overlays of DIC and pol, (C) DIC, and (D) pol; (E) is the area demarcated by the white rectangle in D.

In the next experiment, we changed rVEGF concentration from "medium-low" to "high," that is, from a concentration that typically induces a moderate degree of branching to one that induces triradiate formation. We incubated PMC cultures from 26 hpf in 4% (v/v) FBS supplemented with 0.8 µg·mL^{-1} rVEGF and at 48 hpf increased the rVEGF concentration to 2.8 µg·mL^{-1}; as before, for comparison, we grew separate cultures incubated continuously in either concentration. Cell cultures incubated in 0.8 µg·mL^{-1} rVEGF formed linear and branched

spicules with majority *c*-axis growth (Figure 3.8A), whereas cell cultures incubated in 2.8 $\mu g \cdot mL^{-1}$ rVEGF formed branched spicules ("H" and fork shapes) with majority or half *a*-axis growth (Figure 3.8B). Cultures switched from 0.8 $\mu g \cdot mL^{-1}$ to 2.8 $\mu g \cdot mL^{-1}$ rVEGF formed hyperbranched spicules similar to those formed by the cell cultures switched from 0.4 $\mu g \cdot mL^{-1}$ to 2.8 $\mu g \cdot mL^{-1}$ rVEGF, although not as many branches formed and they grew more in the *c*-axis parallel to the body rod (Figure 3.8C-E).

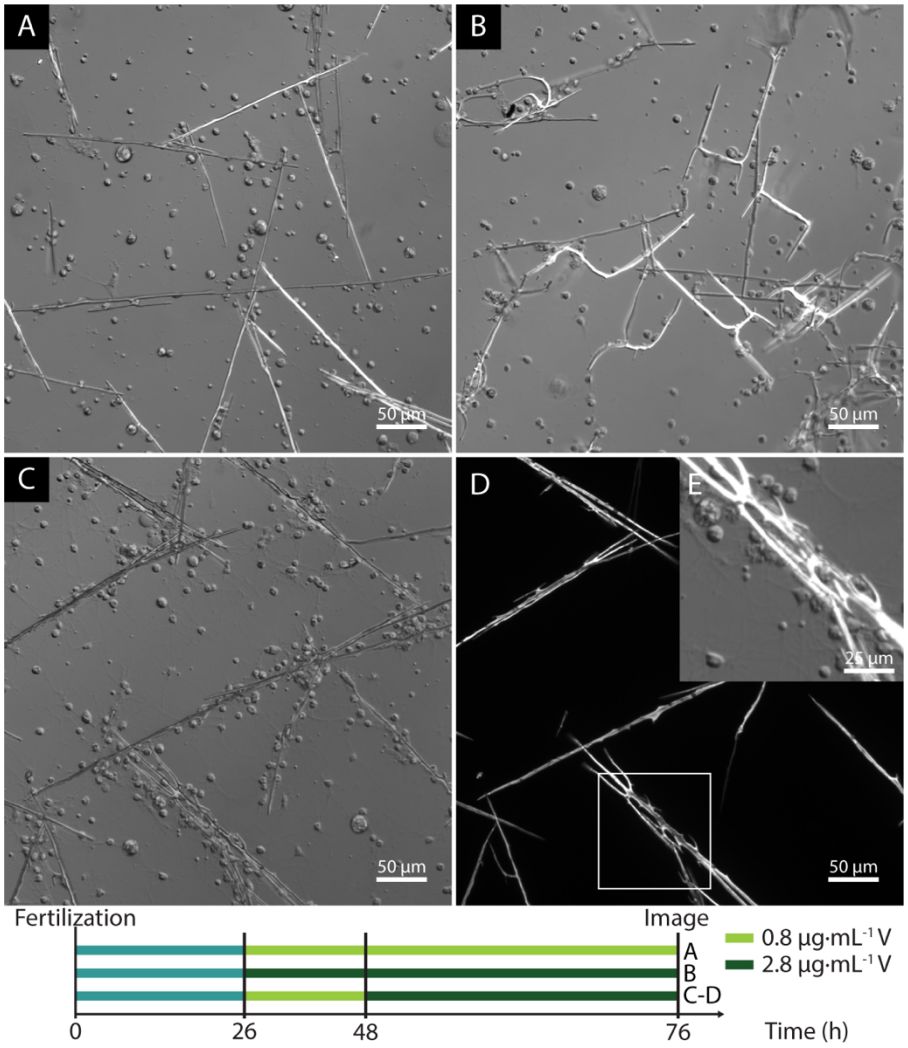

Figure 3.8. Cultures incubated from 26 hpf to 76 hpf in 4% (v/v) FBS supplemented with (A) 0.8 $\mu g \cdot mL^{-1}$ or (B) 2.8 $\mu g \cdot mL^{-1}$ rVEGF (V), or (C-E) incubated in 4% (v/v) FBS supplemented with 0.8 $\mu g \cdot mL^{-1}$ rVEGF from 26 to 48 hpf and 2.8 $\mu g \cdot mL^{-1}$ rVEGF from 48 hpf to 76 hpf. Images taken at 76 hpf; (A,B,E) overlays of DIC and pol, (C) DIC, and (D) pol; (E) is the area demarcated by the white rectangle in D.

Next, cell cultures were switched from “medium” to “high” rVEGF concentration (i.e., 1.2 $\mu g \cdot mL^{-1}$ to 2.8 $\mu g \cdot mL^{-1}$) and separate cultures were incubated in either concentration nonstop. Cell cultures incubated in 1.2 $\mu g \cdot mL^{-1}$ rVEGF formed mostly branched spicules with mixed *a*- and *c*-axis growth (Figure 3.9A), whereas cell cultures incubated in 2.8 $\mu g \cdot mL^{-1}$ VEGF formed mostly triradiates and branched spicules that were short and majority *a*-axis growth (Figure 3.9B). Cultures switched from 1.2 $\mu g \cdot mL^{-1}$ rVEGF to 2.8 $\mu g \cdot mL^{-1}$ rVEGF formed spicules with supernumerary branching, but most of the branches sprouted from the center of the spicule as opposed to homogenously along the body rod like in the case of the previously observed hyperbranched spicules (Figure 3.9C-E).

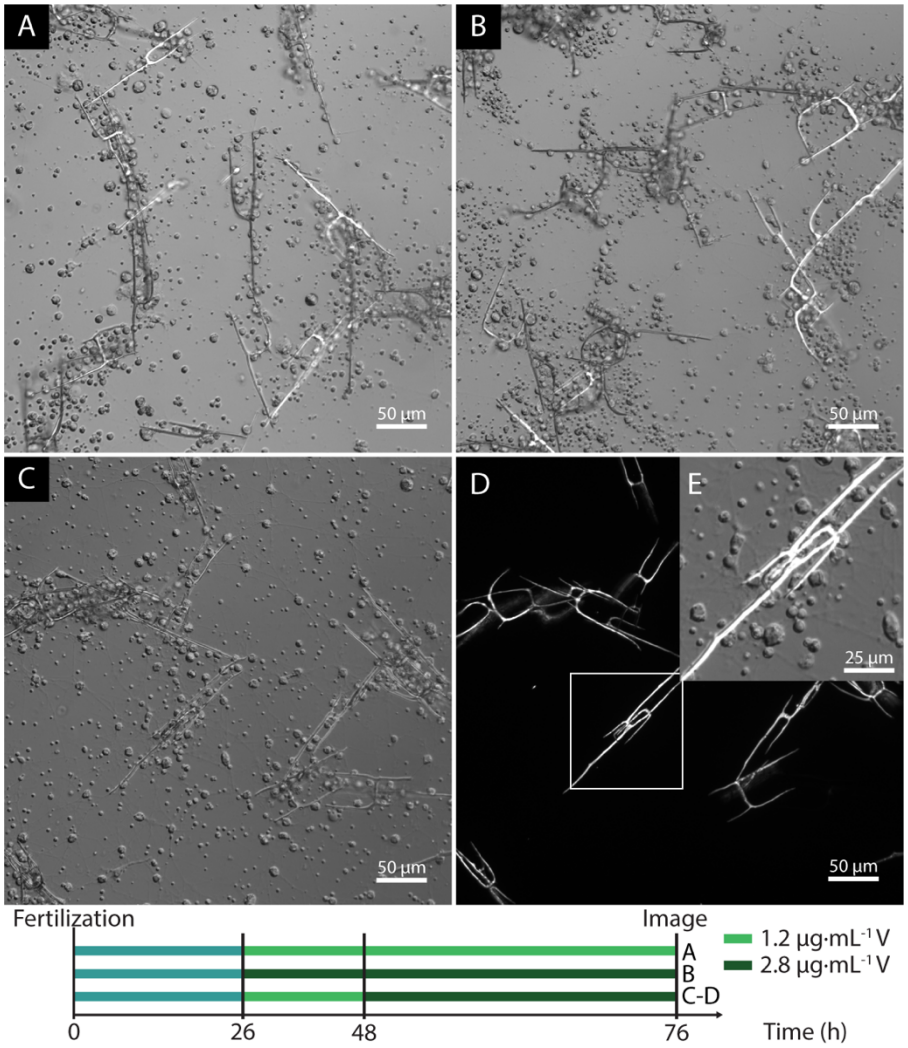

Figure 3.9. Cultures incubated from 26 hpf to 76 hpf in 4% (v/v) FBS supplemented with (A) 1.2 µg·mL^{-1} or (B) 2.8 µg·mL^{-1} rVEGF (V), or (C-E) incubated in 4% (v/v) FBS supplemented with 1.2 µg·mL^{-1} rVEGF from 26 to 48 hpf and 2.8 µg·mL^{-1} rVEGF from 48 hpf to 76 hpf. Images taken at 76 hpf; (A,B,E) overlays of DIC and pol, (C) DIC, and (D) pol; (E) is the area demarcated by the white rectangle in D.

In the last rVEGF switching experiment, cell cultures were switched from "very low" to "high" rVEGF concentration, i.e., from 0.2 µg·mL^{-1} to 2.8 µg·mL^{-1}; as before, separate cell cultures incubated continuously in either concentration were grown for comparison. Cell cultures incubated in 0.2 µg·mL^{-1} rVEGF formed a sparse number of long linear spicules (Figure 3.10A) whereas cell cultures incubated in 2.8 µg·mL^{-1} rVEGF formed branched and triradiate spicules (Figure 3.10B). Cell cultures switched from 0.2 µg·mL^{-1} VEGF to 2.8 µg·mL^{-1} VEGF formed

spicules that were linear but often bifurcated at the end points; in addition, many of the spicules appeared thicker than normal linear spicules (Figure 3.10C-E).

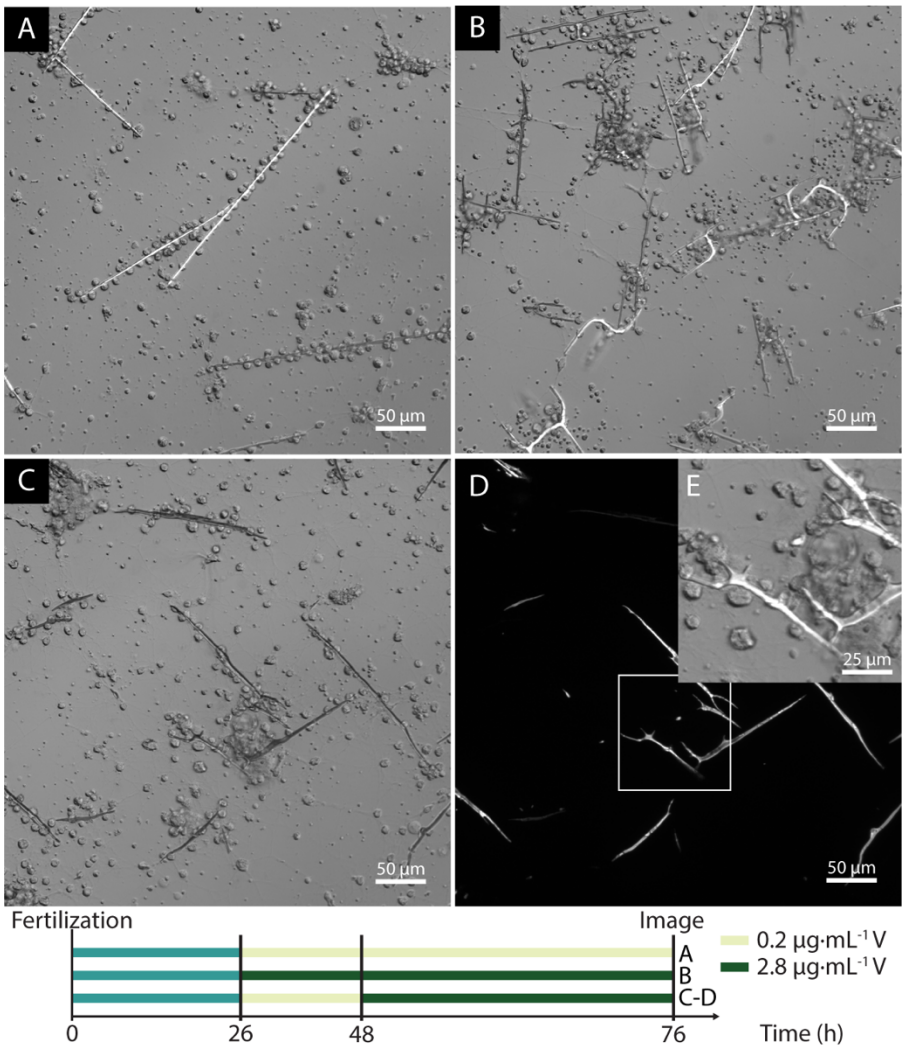

Figure 3.10. Cultures incubated from 26 hpf to 76 hpf in 4% (v/v) FBS supplemented with (A) 0.2 µg·mL^{-1} or (B) 2.8 µg·mL^{-1} rVEGF (V), or (C-E) incubated in 4% (v/v) FBS supplemented with 0.2 µg·mL^{-1} rVEGF from 26 to 48 hpf and 2.8 µg·mL^{-1} rVEGF from 48 hpf to 76 hpf. Images taken at 76 hpf; (A,B,E) overlays of DIC and pol, (C) DIC, and (D) pol; (E) is the area demarcated by the white rectangle in D.

Combining the VEGF time and concentration levers revealed that several additional spicule morphologies can be achieved. By varying the initial concentration of rVEGF and switching to a higher concentration at a later timepoint, we induced PMCs to form thick spicules with bifurcated tips, hyperbranched spicules with branchpoints homogeneously distributed

throughout the body rod, and hyperbranched spicules with branchpoints centered at the middle of the body rod (Figure 3.11). This is possibly related to the shape of the spicules that formed prior to the change in rVEGF concentration. For example, treatment with 1.2 $\mu g \cdot mL^{-1}$ rVEGF results in branched ("h" and fork shapes) spicule formation by 48 hpf; it is possible that the supernumerary branches forming after increasing the rVEGF concentration to 2.8 $\mu g \cdot mL^{-1}$ at 48 hpf sprout from the center of the spicule because there is already a branchpoint there. Spicule branching might also be initiated by swelling of a calcite or ACC "bud" on the rod, which would explain why the spicules formed after switching PMCs from 0.2 $\mu g \cdot mL^{-1}$ to 2.8 $\mu g \cdot mL^{-1}$ rVEGF appeared thicker. However, this hypothesis would need to be validated by closely examining spicules formed by PMC cultures switched from low to high rVEGF, via timelapses using high-resolution light microscopy or through electron microscopy of isolated spicules.

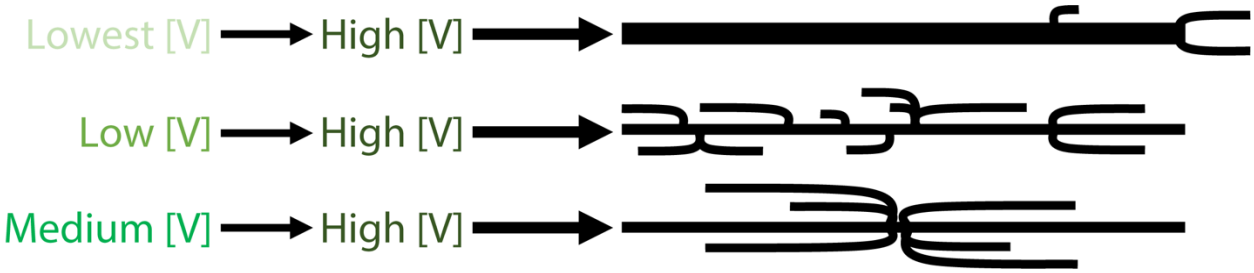

Figure 3.11. Different spicules morphologies achieved by varying the initial rVEGF concentration that is later increased.

These experiments reveal that, in *in vitro* PMC cultures, there exist design rules for effecting different terminal spicule morphologies. For example, sustained *a*-axis growth (such as that of the triradiates) requires continuous and high VEGF signaling, *c*-axis growth (such as that of the linear spicules) stems from a continuous low degree of VEGF signaling, and branched spicules with a high amount of both *a*- and *c*-axis growth result from a continuous medium degree of VEGF signaling or switching between high and low VEGF signaling. We suspect that similar principles also operate in the embryo, perhaps undertaken by ectoderm cells in different

regions secreting varying concentrations of growth factors during different time windows to control PMC patterning and the corresponding spicule elongation and branching. This provides a potential mechanistic explanation for the construction of very complex spicule morphologies, such as the fenestrated and decorated spicules of *Eucidaris tribuloides* (although in that species, the spicule-forming cells are not PMCs).[124]

3.2.4. Calcein staining of hyperbranched spicules

Cell cultures switched from a low to a high rVEGF concentration formed spicules with extraneous branching off the main body rod, positing the question of how the branches formed. Two pathways were possible: after the concentration of rVEGF is increased, 1. the branches sprout off of existing body rod that formed prior to the concentration spike, or 2. the body rod elongates, and branches form off of the new body rod. To elucidate the growth pattern of the hyperbranched spicules, we decided to use calcein. Calcein is a fluorescent Ca^{2+} chelator and has been used extensively to track the uptake of Ca^{2+} into the growing sea urchin spicule.[43, 44, 87, 88, 125] However, calcein staining only describes the growth that occurred during the incubation period, and in the case of the sea urchin spicule, differentiating between growth of new body rod (which occurs in both the longitudinal and radial directions) and thickening of older body rod (which occurs via radial growth) is problematic. Fortuitously, calcein is commercially available in many colors, and staining with two colors of calcein enables the observation of before and after growth and differentiation between elongation and thickening. To visualize how the hyperbranches form, we thus developed bichromatic pulse-chase staining using calcein red and calcein green, which have little fluorescence emission overlap when imaged.

To visualize growth prior to spicule branching, we incubated PMCs cultures in 4% (v/v) FBS supplemented with 0.4 $\mu g \cdot mL^{-1}$ rVEGF from 26 hpf and incubated cultures with calcein green at 48 hpf for 2 h (the green pulse). The rVEGF concentration was increased to 2.8 $\mu g \cdot mL^{-1}$ and cultures were incubated without fluorophore in these media for 22 h (the chase). Cultures were then pulsed with calcein red at 72 hpf for 2 h, chased in 4% (v/v) FBS supplemented with 2.8 $\mu g \cdot mL^{-1}$ rVEGF for 2 h, and fixed.

Two example spicules are shown. In both, calcein green was taken up during the pulse at 48 hpf and intense fluorescence of tip areas illuminated linear growth of the spicule associated with incubation in 0.4 $\mu g \cdot mL^{-1}$ rVEGF (Figure 3.12A,E). Radial growth was also observed via faint outlining of the length of the spicule. Calcein red was taken up during the 72 hpf pulse and illuminated later linear spicule growth as well as branching (Figure 3.12B,F). However, in some spicules, the branches sprouted off of mineral that had already grown by 48 hpf prior to switching to higher rVEGF concentration (Figure 3.12C-D), whereas in other spicules the branches sprouted off of new body rod that grew after the media was switched to a higher rVEGF concentration (Figure 3.12G-H). This demonstrates that both growth scenarios occur during spicule branching.

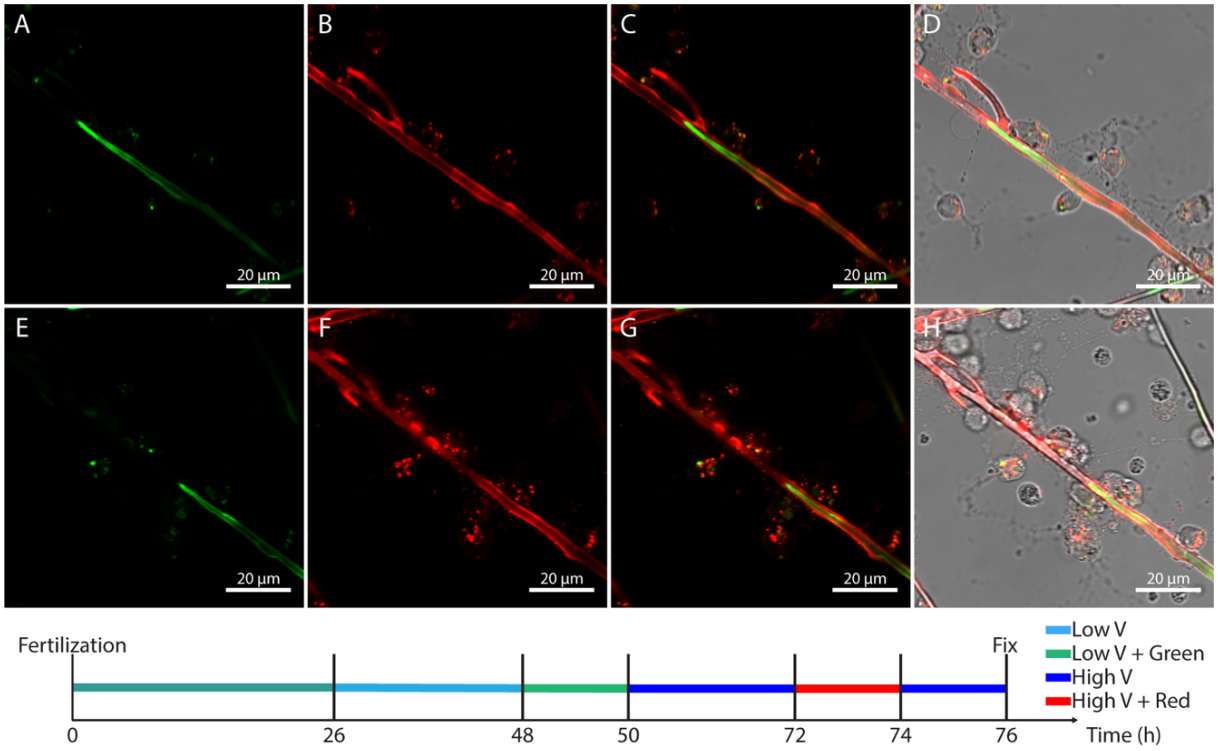

Figure 3.12. Bichromatic calcein staining of hyperbranched spicules. Cultures were incubated in 4% (v/v) FBS supplemented with 0.4 µg·mL^{-1} rVEGF from 26 hpf, treated with calcein green for 2 h at 48 HPF, and switched to and incubated in 4% (v/v) FBS supplemented with 2.8 µg·mL^{-1} rVEGF from 50 hpf. At 72 hpf cultures were treated with calcein red for 2 h, chased in 4% (v/v) FBS supplemented with 2.8 µg·mL^{-1} rVEGF for 2 hrs, fixed, and imaged using confocal microscopy. (A,E) Green channel (calcein green), (B,F) red channel (calcein red), (C,G) overlays of the red and green channels, and (D,H) overlays of the red and green channels and the brightfield channel shown.

3.3. Conclusions

Overall, we expanded upon previous work in our group to show that in addition to the rVEGF concentration lever, there also exists a VEGF timing lever. We validated prior results with our purified rVEGF to show that treating PMCs with an increasing concentration of rVEGF, in either HS or FBS, results in branched and then triradiate spicules. Using the inhibitor axitinib, we demonstrated that early inhibition of rVEGF signaling prevents triradiate formation and encourages *c*-axis growth, without totally shutting down spicule growth, indicating that sustained VEGF signaling is necessary for majority *a*-axis growth. Delayed introduction of VEGF signaling still produces branched or triradiate spicules, up until 48 hpf when it induces

hyperbranched spicule formation. By varying the initial rVEGF concentration and later switching to a higher rVEGF concentration, we demonstrated that several unique spicule morphologies can be achieved, thus revealing PMC skeletogenesis design rules. Furthermore, by innovating the use of bichromatic calcein staining, we showed that spicule branching occurs off of both previously formed body rod and off of simultaneously forming novel body rod. We believe that structural analyses, such as through TEM or cryo-SEM, will be able to elucidate the molecular mechanisms through which the PMCs control branching morphogenesis after responding to VEGF signaling cues.

3.4. Materials and Methods

3.4.1. Consumables and equipment

Chemicals and disposables:

Unless otherwise noted, all reagents were stored at room temperature (22 °C). Ethanol (200 proof) (Decon Laboratories Inc., Prince of Prussia, PA); concentrated bleach (8.25% NaClO) (The Clorox Company, Oakland, CA); $MgCl_2 \cdot 6H_2O$ (≥99%), KCl (≥99%) (Avantor, Radnor, PA); NaCl (≥99.5%), $MgSO_4$ (anhydrous, ≥99.5%), $CaCl_2 \cdot 2H_2O$ (≥99%), $NaHCO_3$ (≥99%), Na_2CO_3 (anhydrous, ≥99.5%), sucrose (≥99.5%), concentrated HCl (35-37%), glycine (≥99%), gentamicin sulfate (≥590 $\mu g \cdot mg^{-1}$, stored at 4 °C), penicillin + streptomycin (10,000 $U \cdot mL^{-1}$ penicillin, 10,000 $\mu g \cdot mL^{-1}$ streptomycin in 0.85% NaCl, 0.1-µm sterile filtered, stored at -20 °C), isopropyl β-D-thiogalactopyranoside (IPTG, stored at -4 °C) (Sigma-Aldrich, St. Louis, MO); NaOH (≥99.1%), tris-HCl (1 M, pH = 7.4, stored at 4 °C), EDTA disodium salt dihydrate (0.5 M, pH = 8.0, stored at 4 °C), paraformaldehyde (PFA, 16% (v/v)), dimethyl sulfoxide (DMSO, anhydrous, ≥99%), calcein (≥95%, stored in the dark at 4 °C), horse serum (sterile, heat

inactivated, stored at -20 °C, Gibco Cat #26050), fetal bovine serum (sterile, heat inactivated, stored at -20 °C, Gibco Cat #A3160501), Luria-Bertani broth (LB, sterile) (Thermo Fisher Scientific, Waltham, MA); calcein red™ (≥90%, stored at 4 °C), axitinib (≥98%, stored at -20 °C) (Cayman Chemical, Ann Arbor, MI); pMAL™ Protein Fusion & Purification System, amylose resin (in 20% (v/v) ethanol, stored at 4 °C) (New England Biolabs, Ipswich, MA); Quick Start™ Bradford protein assay kit (Bio-Rad Laboratories, Hercules, CA); Instant Ocean® sea salt (Instant Ocean, Blacksburg, VA).

Sterile Falcon tubes (15-mL, 50-mL), Corning sterile poly(ether sulfone) filter units (0.22-µm, 1-L), Cellvis 29-mm^2 tissue culture dishes with 20-mm^2 #1.5 glass bottom insert (Thermo Fisher Scientific, Waltham, MA); sterile polystyrene serological pipettes (10-mL, 20-mL) (TPP, Trasadingen, Switzerland); sterile low-binding pipette tips (1-20-, 100-1,000-µL,) (Midwest Scientific, Valley Park, MO); Eppendorf® tubes (0.5-, 1.7-mL) (Eppendorf, Hamburg, Germany); silicon wafers (Electron Microscopy Sciences, Hatfield, PA); dialysis tubing Spectra/Por (12,000-14,000-kDa molecular weight cut-off) (Repligen, Waltham, MA); Vivaspin® centrifugal concentrators (50-mL, 50-kDa molecular weight cut-off) (Sartorius, Göttingen, Germany).

Equipment:

Flasks (500-, 1,000-mL), beakers (250-, 500-mL), graduated cylinders (100-, 500-mL) (Thermo Fisher Scientific, Waltham, MA); Centrifuge 5424, centrifuge 5810R (with temperature control, swing-bucket rotor with four 500-mL buckets, conical 50- and 200-mL inserts), single-channel adjustable volume pipettes (2-20-, 20-200-, 100-1000-µL) (Eppendorf, Hamburg, Germany); Portable Pipet-Aid® XP2 Pipette Controller (Drummond Scientific, Broomall, PA);

vacuum aspirator with trap (Sigma-Aldrich, St. Louis, MO); NanoVue™ Plus Spectrophotometer (GE Healthcare, Chicago, IL).

Solutions:

Unless otherwise noted, all aqueous solutions were prepared with ultra-pure water (UPW, $\rho = 18.2$ M·Ω·cm) dispensed by a Barnstead NanoDiamond UF + UV purification unit and stored at 15 °C. A solution of 2.5 M NaOH was prepared by dissolving 50 g NaOH in 500 mL UPW. A solution of 1.0 M HCl was prepared by diluting 20.75 mL concentrated HCl in a 250-mL volumetric flask with UPW.

Column buffer (CB) was made with the following final concentrations: 20 mM Tris-HCl, 200 mM NaCl, and 1 mM EDTA.

Since acidic media dissolves the spicule, the pH of all solutions used with cell cultures was checked and adjusted to ~8.0 by titration with 2.5 M NaOH, if necessary. Artificial seawater (ASW) was prepared with the following final concentrations: 0.48 M NaCl, 0.10 M $CaCl_2 \cdot 2H_2O$, 0.01 M KCl, 0.03 M $MgSO_4$, 0.027 M $MgCl_2 \cdot 6H_2O$, and 0.002 M $NaHCO_3$. ASW was filtered with a 0.22-μm Corning filter.

A volume of 100 mL horse serum was dialyzed twice against 1 L ASW overnight at room temperature (molecular weight cutoff = 12,000-14,000 kDa), sterile filtered with a 0.22-μm Corning filter, and separated into 4 mL-aliquots that were stored at -20 °C. This process was repeated exactly for fetal bovine serum.

A 2 $mg \cdot mL^{-1}$ calcein stock solution was prepared by dissolving 100 mg calcein in 50 mL UPW and was stored in the dark at 4 °C (to avoid confusion with other calcein colors, calcein is henceforth referred to as calcein green). A 1 $mg \cdot mL^{-1}$ calcein red™ stock solution was prepared

by dissolving 1 mg calcein red™ in 1 mL UPW and was stored in the dark at 4 °C (calcein red™ is henceforth referred to as calcein red). A stock solution of 5 mM axitinib was prepared by dissolving 50 mg of axitinib in 25.87 mL of DMSO.

The fixative of 4% PFA was prepared in ASW. A 300 mM glycine solution was prepared by dissolving 1.12 g glycine in 50 mL ASW.

A solution of 85% (w/v) sucrose was prepared by dissolving 425 g sucrose in 500 mL UPW by gently stirring and heating (50 °C, 20 min). A stock solution of 300 mM Na_2CO_3 was prepared by dissolving 3.18 g Na_2CO_3 in 100 mL UPW. This was diluted 1:10 and 1:39 in UPW to make 30 mM and 7.7 mM solutions of Na_2CO_3. 25% (v/v), 50% (v/v), and 75% (v/v) ethanol solutions were prepared in UPW.

3.4.2. Generation and purification of rVEGF

The cloning and expression of rVEGF as a maltose binding protein (MBP) fusion construct was followed from a previously described protocol. All experiments in this project used high-purity rVEGF purified using amylose-Sepharose affinity chromatography as follows. A single bacteria colony was selected, inoculated in 50 mL LB, and grown overnight at 30 °C. The culture was transferred to 500 mL LB and grown at 30 °C while monitoring the optical density at 600 nm (OD600) with a spectrophotometer. When the OD600 reached 0.6 (~4 h), 0.42 g ITPG was added to the culture solution to achieve a concentration of 0.3 mM and the culture was incubated overnight at 20 °C. The bacterial suspension was centrifuged, supernatant was discarded, and cells were resuspended in 25 mL CB. Suspended cells were frozen in CB overnight at -20 °C. The frozen cell suspension was thawed in cold water the next day. The suspension was placed in an ice-water bath and sonicated in short pulses of 15 seconds for ~2-3

min total. The suspension was then centrifuged (20,000 x *g*, 20 min) and the supernatant was used for isolation of MBP-VEGF. The bacterial crude extract was diluted 1:6 with CB and reacted with 15 mL of the amylose resin in a 50-mL tube. The tube was rotated overnight at 4 °C, centrifuged (20,000 x *g*, 20 min), and supernatant was discarded.

The amylose resin with bound protein was poured into a 2.5-cm column. The column was washed with 12 column volumes of CB at a rate of 10 $mL \cdot min^{-1}$. The effluent was monitored for protein as follows. 1 mL of Bradford dye solution was diluted with UPW in a total volume of 5 mL and aliquots of 50 µL were mixed with 20 µL of protein sample. A sudden change of color from brown to blue signified the presence of protein in the fractions. The column was washed until no protein was detected. The column was then washed with CB containing 0.5 M NaCl until it was free of protein. The bound rVEGF fusion protein was eluted with CB + 10 mM maltose and 3 mL fractions were collected. The fusion protein eluted within the first 5 fractions. After the second fraction, the column was closed for 90 mins, after which elution was continued. 10-20 3-mL fractions were collected. Protein was easily detected by the Bradford protein assay (as above).

Protein-containing fractions were pooled together, and if necessary, concentrated in a 50-mL Vivaspin® centrifugal concentrator (50-kDa molecular weight cutoff filter). Using a spectrophotometer, the final rVEGF concentration was found to be 140 $\mu g \cdot mL^{-1}$.

3.4.3. Micromere isolation and *in vitro* primary mesenchyme cell culture

Sea urchins were purchased from Marinus Scientific (Long Beach, CA) and South Coast Bio-Marine LLC (San Pedro, CA) and maintained in Instant Ocean® seawater at 15 °C. Glass bottom plates used in PMC culture were acid washed as described in section 2.2.3. All

experiments involving cell culture were performed in a climate-controlled room at 15 °C. Micromeres were isolated and seeded at a density of 100,000 cells per glass bottom plate as described in section 2.1.5.

ASW used in PMC culture was supplemented with 100 $\mu g \cdot mL^{-1}$ gentamicin sulfate and 100 $U \cdot mL^{-1}$ penicillin + 100 $\mu g \cdot mL^{-1}$ streptomycin (ASWGPS). ASWGPS was supplemented with 4% (v/v) HS or 4% (v/v) FBS (for brevity, 4% (v/v) HS or FBS in ASWGPS are simply referred to as 4% (v/v) HS or FBS, the "in ASWGPS" implied). Immediately prior to use in cell culture, the rVEGF stock solution was thawed at room temperature and diluted 1:350, 1:175, and 1:115 in 4% (v/v) HS to achieve concentrations of 0.4 $\mu g \cdot mL^{-1}$, 0.8 $\mu g \cdot mL^{-1}$, and 1.2 $\mu g \cdot mL^{-1}$. Alternatively, rVEGF was diluted 1:700, 1:350, 1:175, 1:115, and 1:50 in 4% FBS to achieve concentrations of 0.2 $\mu g \cdot mL^{-1}$, 0.4 $\mu g \cdot mL^{-1}$, 0.8 $\mu g \cdot mL^{-1}$, 1.2 $\mu g \cdot mL^{-1}$, and 2.8 $\mu g \cdot mL^{-1}$. PMCs were washed with and cultured in these media as described in section 2.1.5.

3.4.4. Inhibitor treatment of PMC cultures

Immediately prior to use in experiments, the axitinib stock solution was thawed at room temperature and diluted 1:200 in 200 µL of DMSO to achieve a concentration of 25 µM. This solution was diluted 1:500 in 2 mL 4% (v/v) HS + 1.2 $\mu g \cdot mL^{-1}$ rVEGF to achieve a working concentration of 50 nM axitinib. Cell cultures were washed (1×, 2 mL) with and incubated in these media at 15 °C.

3.4.5. Spicule isolation and SEM imaging

At 76 hpf, media were removed from the plates via aspiration and 2 mL of 8.25% (v/v) bleach were added to each plate. Spicules were dislodged using gentle trituration with a pipette. Bleach containing spicules and organic material was transferred to 2-mL Eppendorf tubes, which

were then centrifuged (9,500 × *g*, 5 min). Supernatant was removed, and pellets of spicules and organic material were dispersed and collected in 2 mL of 8.25% (v/v) bleach. This suspension was incubated for 20 min at room temperature with gentle agitation and was then centrifuged (9,500 × *g*, 5 min).

Spicules were washed (i.e., suspended in 1 mL of solution and centrifuged (9,500 × *g*, 5 min)), in series, with 8.25% (v/v) bleach, 30 mM Na_2CO_3, and 7.7 mM Na_2CO_3, and were then dehydrated by washing, in series, with 25% (v/v), 50% (v/v) 75% (v/v), and 100% ethanol, the last wash repeated once. Spicules were stored for several days to weeks at -20 °C.

For electron microscopy, ~5 µL of spicules suspended in ethanol were pipetted onto silicon wafer fragments and air dried. These samples were mounted onto aluminum SEM stubs using double-sided carbon tape and coated with 20 nm of Au/Pd using a Denton Desk IV sputter coater (Denton Vacuum). Samples were imaged using a Hitachi SU8030 SEM equipped with a field emission source. Images were recorded at 2 keV acceleration voltage and a working distance of 8.0 mm, using secondary electron contrast.

3.4.6. Calcein staining of primary mesenchyme cell cultures

To achieve a working concentration of 150 µg·mL^{-1} calcein green, 150 µL of the calcein green stock solution was added to culture plates containing 2 mL culture media. Alternatively, 20 µL of the calcein red stock solution were added to achieve a working concentration of 10 µg·mL^{-1}. Plates were gently swirled to evenly distribute the solution and kept in the dark.

For bichromatic calcein staining, cultures were incubated with either calcein color (i.e., "pulsed") for 2 h at 15 °C, washed with ASWGPS (2×, 2 mL) and culture media (2×, 2 mL), incubated 60 min in culture media (i.e., "chased") for 22 h, pulsed with the other calcein color

for 2 h, washed with ASWGPS (2×, 2 mL) and culture media, chased in culture media for 2 h, and fixed according to the protocol in section 2.2.3.

3.4.7. Optical and confocal fluorescence imaging

Cell cultures were imaged on an inverted Leica DM6000b light microscope with polarized and differential interference contrast (DIC) illumination capabilities. Bright field (BF) and DIC illumination were used to image cells and spicules, whereas cross-polarized illumination was used to identify birefringent spicules and granules. 10× and 20× objective lenses were used. For fluorescently labeled samples, high resolution imaging was performed on a Leica TCS SP8 laser scanning confocal microscope using a 63× oil immersion objective lens. Calcein green fluorescence was obtained with an excitation wavelength of 488 nm and capture of 500-570 nm bandwidth. Calcein red fluorescence was obtained with an excitation wavelength of 552 nm and capture of 560-650 nm bandwidth. Images were adjusted for brightness and contrast using ImageJ (NIH, Bethesda, Maryland).

Chapter 4. Role of the Cytoskeleton in Spiculogenesis

4.1. Introduction

PMC morphogenesis leading up to spiculogenesis has been extensively researched and includes an epithelial-to-mesenchymal transition (EMT), choreographed cell migration, extension of filopodia, and fusion of the cell membranes to form the syncytium in which the spicule grows.[126, 127] These critical events require motile cells and thus necessitate cytoskeleton involvement. Spiculogenesis itself comprises initial nucleation of the calcite crystal, rapid elongation along the calcite *a*-axes to form the triradiate spicule, and a sudden change in crystallographic direction from *a*- to *c*-axis growth to form the body rods.[34, 35] The syncytium enclosing the spicule must be continuously reshaped during these processes because the membrane tightly wraps around the spicule[99, 105], further necessitating intimate participation of the cytoskeleton. From these observations, it should follow that the cytoskeleton plays a critical role not only in early PMC development, but also in the spicule forming processes.

Previous studies have investigated possible roles of the cytoskeleton components actin microfilaments and microtubules in early PMC morphogenesis. Fluorescence microscopy of embryos stained with fluorescent f-actin labels revealed high concentrations of actin in ingressing PMCs, while small molecule inhibition of microfilament contraction delayed PMC ingression into the blastocoel and prevented later events, including migration from the ventrolateral clusters (VLCs), patterning along the blastocoel, and spicule formation.[128] PMC filopodia, which are thought to guide cell movement by sensing chemotactic cues[78, 82, 129, 130], are destroyed by treatment with actin depolymerizing inhibitors, indicating that these structures primarily comprise actin microfilaments.[68] Microtubule inhibition failed to delay or stop the

EMT, but completely arrested migration and stereotyped patterning of the PMCs, suggesting that microtubules are important for PMC motility.[131] This was further supported by electron micrographs that showed microtubule localization in PMC cytoplasmic extensions.[91]

More recent studies have probed other molecules associated with the cytoskeleton. Knockdown and inhibition of Cdc42, a member of the Rho family of small GTPases, resulted in PMCs that failed to form the syncytium, extend filopodia, migrate out of the VLCs, or construct spicules.[69] Inhibition of cytoskeletal factors downstream of Cdc42, including formins and the Arp2/3 complex, also resulted in PMCs that could not form well-defined VLCs, extend filopodia, or develop spicules. Taken together, these experiments strongly indicate that Cdc42 and its downstream molecules lead to patterning and movement of PMCs that is essential for spicule formation.

Although prior research has demonstrated general functions of the cytoskeleton in early PMC development, these studies focused on PMC behavior leading up to skeletogenesis. As such, the role of the cytoskeleton in building the mineral remains relatively unexplored. Furthermore, since these studies dealt with the whole embryo, subtle effects from other cell types also subject to inhibitor perturbation while interacting with the PMCs cannot be discounted. Fortuitously, as has been already discussed, the micromere-PMC gene regulatory network (GRN) is autonomous to the cell line[52], enabling *in vitro* culture of PMCs to study processes such as spiculogenesis outside the complex biochemical signaling environment of the embryo.[65] As an added benefit, *in vitro* culture allows for fine spatiotemporal control over PMC interaction with inhibitors, making possible experiments that would require complex gene knockdown experiments *in vivo*.

We thus investigated the role of the cytoskeleton in spiculogenesis using *in vitro* culture of PMCs. We probed the role of the two main cytoskeletal elements, actin microfilaments and microtubules, using the small molecule inhibitors latrunculin A and nocodazole. We examined the cytoskeleton and the effects of cytoskeletal inhibition on spicule growth, calcium uptake into the spicule, and vesicle uptake using optical and fluorescence microscopy. In addition, we investigated the possible roles of clathrin-mediated endocytosis and motor protein transport along microtubules in spicule growth using small molecule inhibitors. Our results indicate a macropinocytosis-driven mechanism for spiculogenesis.

4.2. Results and Discussion

4.2.1. Fluorescence imaging of actin and tubulin

We first sought to elucidate the form and function of the cytoskeleton during spiculogenesis by determining what structures are present and where they localize. Accordingly, we imaged the cytoskeleton using confocal fluorescence microscopy combined with fluorescently conjugated cytoskeleton stains, which together enable precise characterization of microscopic features such as filaments. We fixed cells immediately after treatment with 4% (v/v) HS (26 hpf), at the time of granule deposition (32 hpf), after the elongation of spicules (48 hpf), and stained for actin or tubulin, and nuclei.

To visualize actin microfilaments, we used an Alexa Fluor® conjugate of the toxin phalloidin, which binds to F-actin and has been used to image actin in sea urchin embryos and PMC filopodia.[78, 128] At all timepoints we observed filamentous actin but not necessarily in the form of stress fibers (Figure 4.1A-C). At 26 hpf, actin was present in the cell membrane, cytoplasm surrounding the nuclei, and some short filopodia (Figure 4.1A). At 32 hpf, actin

staining became pronounced in the syncytial cables forming between cells, and in the filopodia and pseudopodia extensions that spread across the plates (Figure 4.1B). As spicules elongated, actin labeling became especially intense at the growing tips, in what we referred to as "actin hot spots" (Figure 4.1C, Figure 4.2).

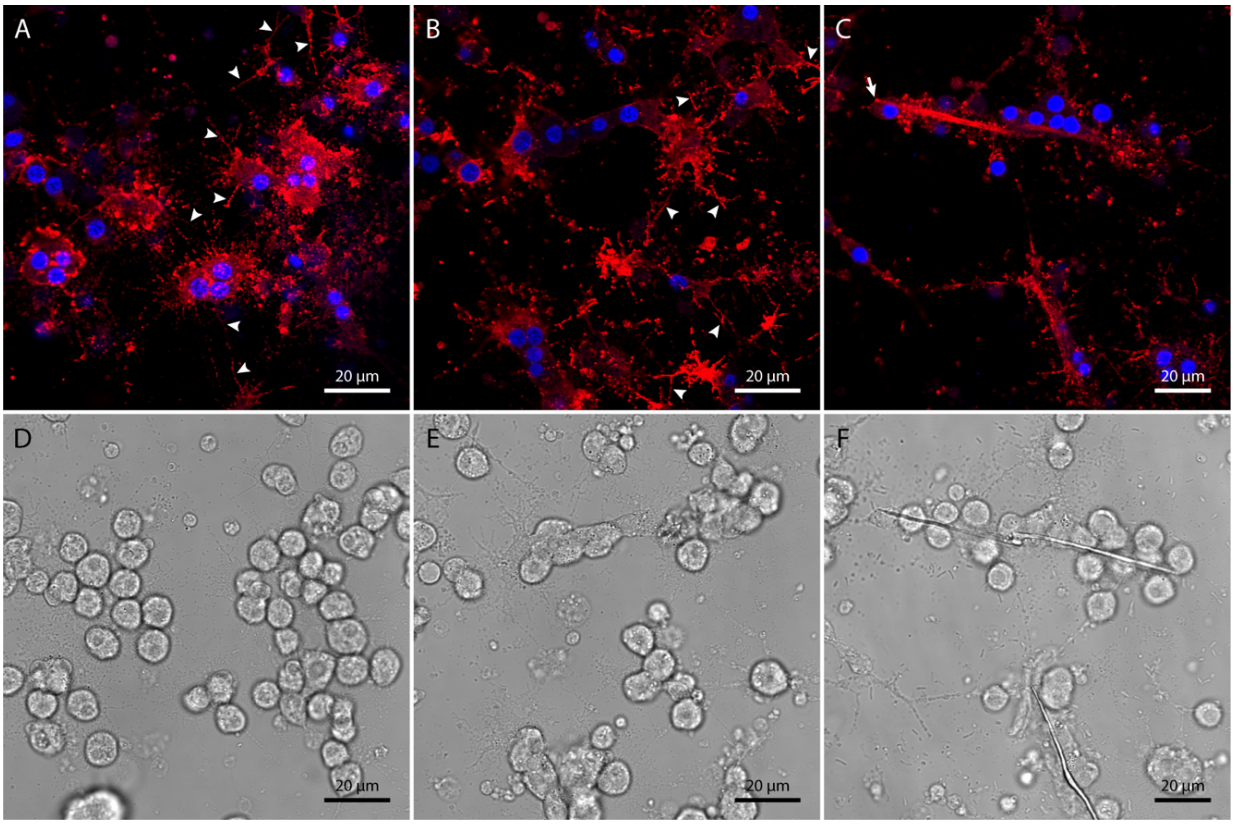

Figure 4.1. Actin distribution during spiculogenesis. Cultures were stained with phalloidin-CF®568 (red) to visualize actin microfilaments and counterstained for nuclei with Hoechst 33342 (blue). Imaged using confocal microscopy. Cultures were fixed at (A,D) 26 hpf, (B,E) 32 hpf, and (C,F) 48 hpf. (A-C) Red and blue channels and (D-F) BF shown. Filopodia (arrowheads, A-B) and actin hotspot at the growing tip of a spicule (arrow, C) indicated.

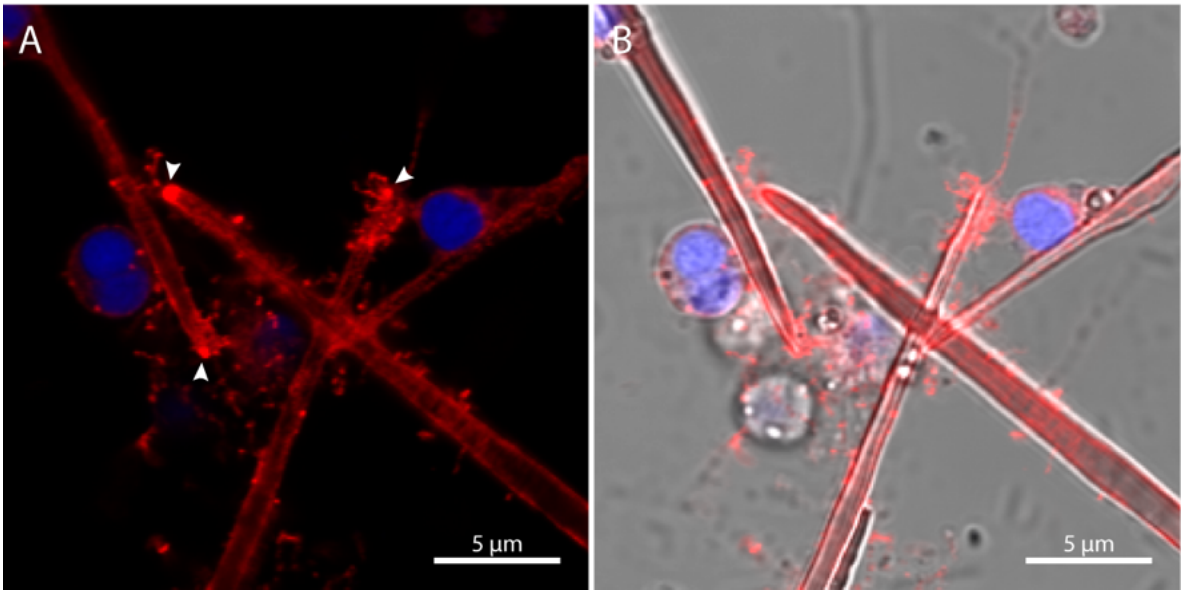

Figure 4.2. Actin hotspots. Cultures were stained with phalloidin-CF®568 (red) to visualize actin hotspots and counterstained for nuclei with Hoechst 33342 (blue). Imaged using confocal microscopy. (A) Red and blue channels and (B) overlay of red, blue, and BF. Actin hotspots (arrowheads, A) indicated.

To image microtubules, we immunostained cultures with the primary antibody DM1α, which is specific for α-tubulin, and an Alexa Fluor® conjugate of a secondary antibody. Tubulin was present at all timepoints in the cytoplasm and near the cell membranes (Figure 4.3A-C). At 26 hpf, tubulin was observed in the cytoplasm surrounding the nuclei and in some short thin strands connecting cells (Figure 4.3A). By 32 hpf, tubulin distribution grew slightly in complexity, with the thin strands between cells becoming well-defined (Figure 4.3B). At 48 hpf, tubulin had assumed a more stereotypical microtubule-like morphology, with long intertwining strands connecting cells and extending beyond the syncytia (Figure 4.3C).

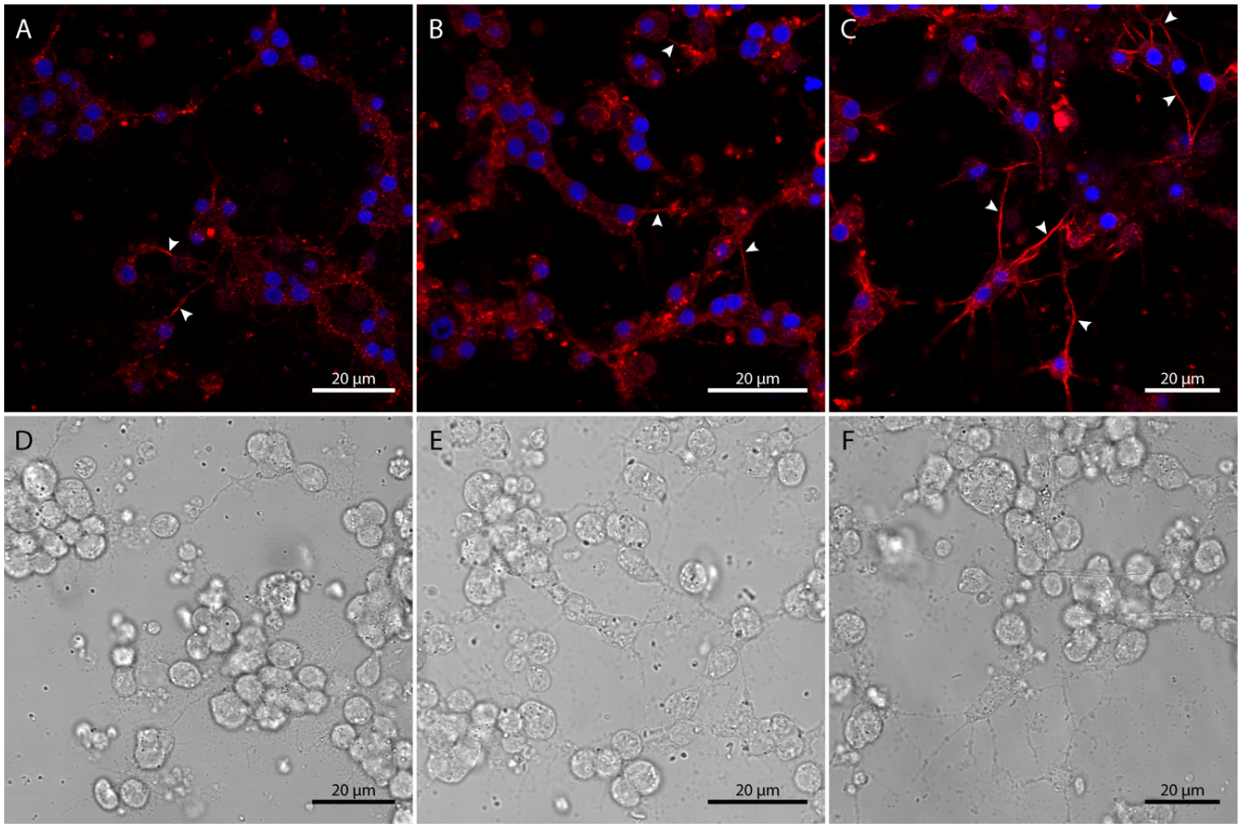

Figure 4.3. Microtubule distribution during spiculogenesis. Tubulin was tagged with DM1α and stained with the secondary antibody goat anti-mouse CF®633 (red); cultures were also counterstained for nuclei with Hoechst 33342 (blue). Imaged using confocal microscopy. Cultures were fixed at (A, D) 26 hpf, (B,E) 32 hpf, and (C,F) 48 hpf. (A-C) Red and blue channels and (D-F) BF; strands of tubulin (arrowheads, A-C) indicated.

Fluorescence imaging of both molecules revealed predicted structures: filopodia in the actin-labeled cultures and thin microtubule strands in the tubulin-labeled cultures. These results agree with current understanding that filopodia comprise actin microfilaments and microtubule strands comprise tubulin. The actin masses in pseudopodia extensions at all timepoints were also expected, as actin is critical for cell adhesion and motility. However, of great interest were the actin hotspots consistently observed at the growing tips of the spicules. Elongation of the spicule must be accompanied by a corresponding growth of the membranous spicule compartment, which is then filled with mineral. We postulate that there exists an actin growth front at the tip of the growing spicule, hence the existence of the actin hotspots. A similar feature does not appear

in the tubulin-stained images, suggesting that microtubules do not localize at the growing tip. It is likely that actin and tubulin organize into different microstructures and assume vastly different roles in spicule formation.

4.2.2. Concentration series: inhibition of actin and tubulin

After using fluorescence microscopy to reveal the form of the cytoskeleton, the next step was to uncover its function in spicule formation. A common method to study the role of a macromolecule is to perturb its normal activity using pharmacological inhibitors. This approach has been widely used to dissect pathways in sea urchin embryonic development ranging from early cell differentiation to PMC morphogenesis.[56, 128] In this vein of thinking, we developed an assay to establish the dose-response relationship for actin and tubulin inhibitors.

To disrupt actin structures, we used latrunculin A, which depolymerizes actin microfilaments. In control plates incubated with only 4% (v/v) HS, most crystals observed were spicules (i.e., linear mineral longer than 2-3 μm) and there were few granules (i.e., small deposits of mineral less than 2 μm) (Figure 4.4A, Figure 4.5). Treatment with 12.5 nM latrunculin A at 32 hpf caused both the number of spicules and granules to increase (~30%, 50%) (Figure 4.5), although the spicules grew shorter (~30%) (Figure 4.4B, Figure 4.6). Treatment with 25 nM latrunculin A caused the number of granules to increase (~70%) from the previous concentration and the number of spicules to plummet (~60%) (Figure 4.5), and the average spicule length to shrink (~40%) (Figure 4.6). Treatment with 50 nM latrunculin A caused the number of spicules to reach zero and the number of granules to slightly decrease (~15%) from the previous concentration (Figure 4.6). The number of spicules remained zero from 50 nM to 100 nM,

whereas the number of granules remained constant from 50 nM to 75 nM and decreased (~25%) from 75 nM to 100 nM (Figure 4.6).

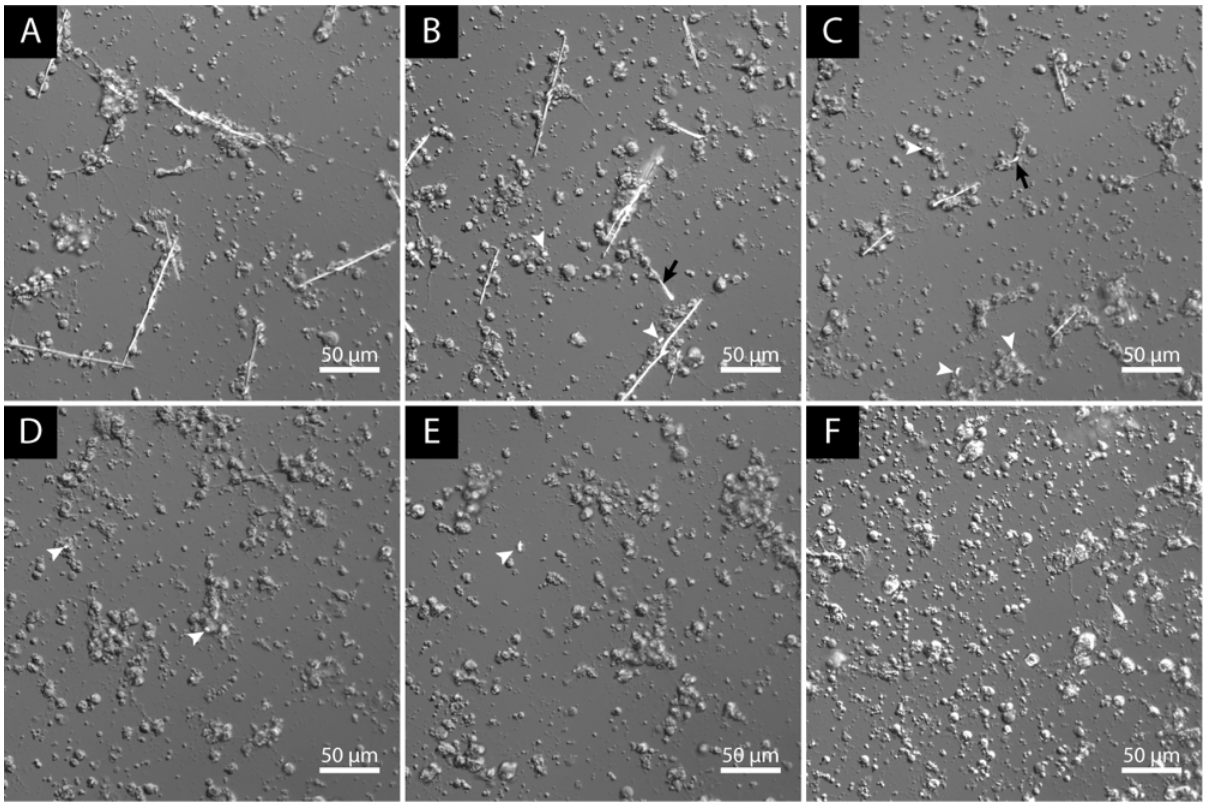

Figure 4.4. Dose-response of PMCs to latrunculin A inhibition of actin. Cultures were treated from 32 to 32.5 hpf with (A) 0 nM latrunculin A, (B) 12.5 nM latrunculin A, (C) 25 nM latrunculin A, (D) 50 nM latrunculin A, (E) 75 nM latrunculin A, and (F) 100 nM latrunculin A and were imaged at 56 hpf (frames are overlays of differential interference contrast (DIC) and pol). Small spicules (black arrows, B-C) and granules (white arrowheads, B-E) indicated.

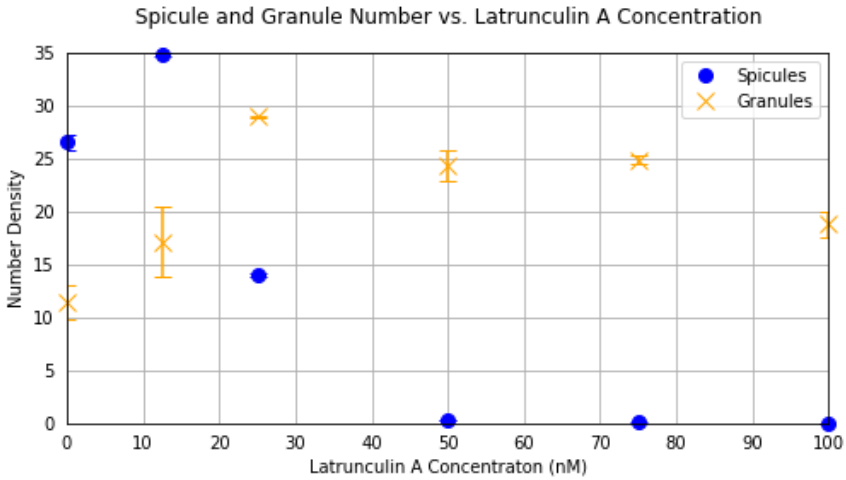

Figure 4.5. Dose-response for treatment of PMCs with latrunculin A. Plot of the average number of spicules (circle) and granules (x) observed per image frame (0.44 mm^2) vs. concentration of latrunculin A. Error bars indicate +/- one standard deviation of the mean (n = 10). PMCs were treated with latrunculin A from 32 to 33.5 hours hpf and observed at 56 hpf.

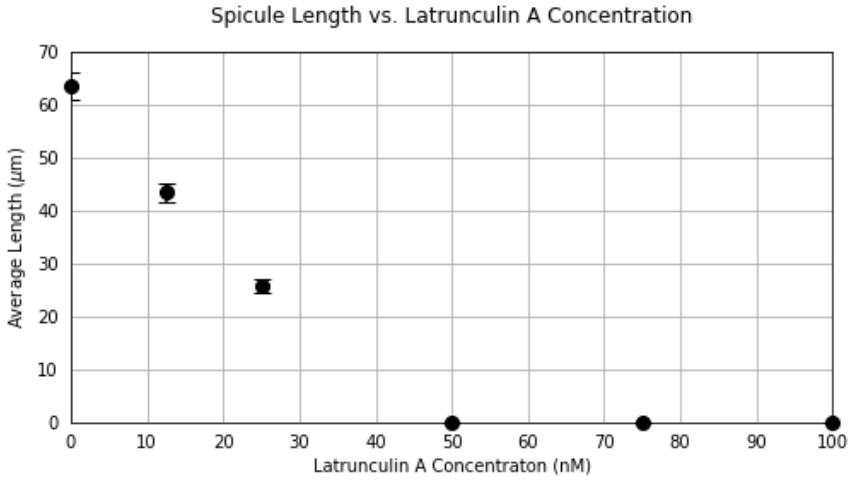

Figure 4.6. Dose-response for treatment of PMCs with latrunculin A and effect on spicule length. Plot of the average spicule length observed. Error bars indicate +/- one standard deviation of the mean. PMCs were treated with latrunculin A from 32 to 33.5 hours hpf and observed at 56 hpf. No measurable spicules were observed beyond 25 nM latrunculin A.

For tubulin inhibition, we used nocodazole, which depolymerizes microtubules and has been used to study the PMC EMT.[131] In control plates, most spicules observed were linear (Figure 4.7A, Figure 4.8). Treatment with 2.5 μM nocodazole at 32 hpf resulted in the number of spicules decreasing (~40%) and the number of granules massively increasing (~360%) (Figure 4.8), and the average spicule length plummeting (~75%) (Figure 4.7B, Figure 4.9). Treatment

with 5 μM nocodazole resulted in the number of spicules decreasing (~40%) from the previous concentration and the number of granules increasing (~15%) (Figure 4.8), and the average spicule length slightly decreasing (~10%) (Figure 4.9). Increasing the concentration to 10 μM, 15 μM, and 20 μM did not significantly affect the number of spicules or the average spicule length, although the number of granules fluctuated slightly (Figure 4.8).

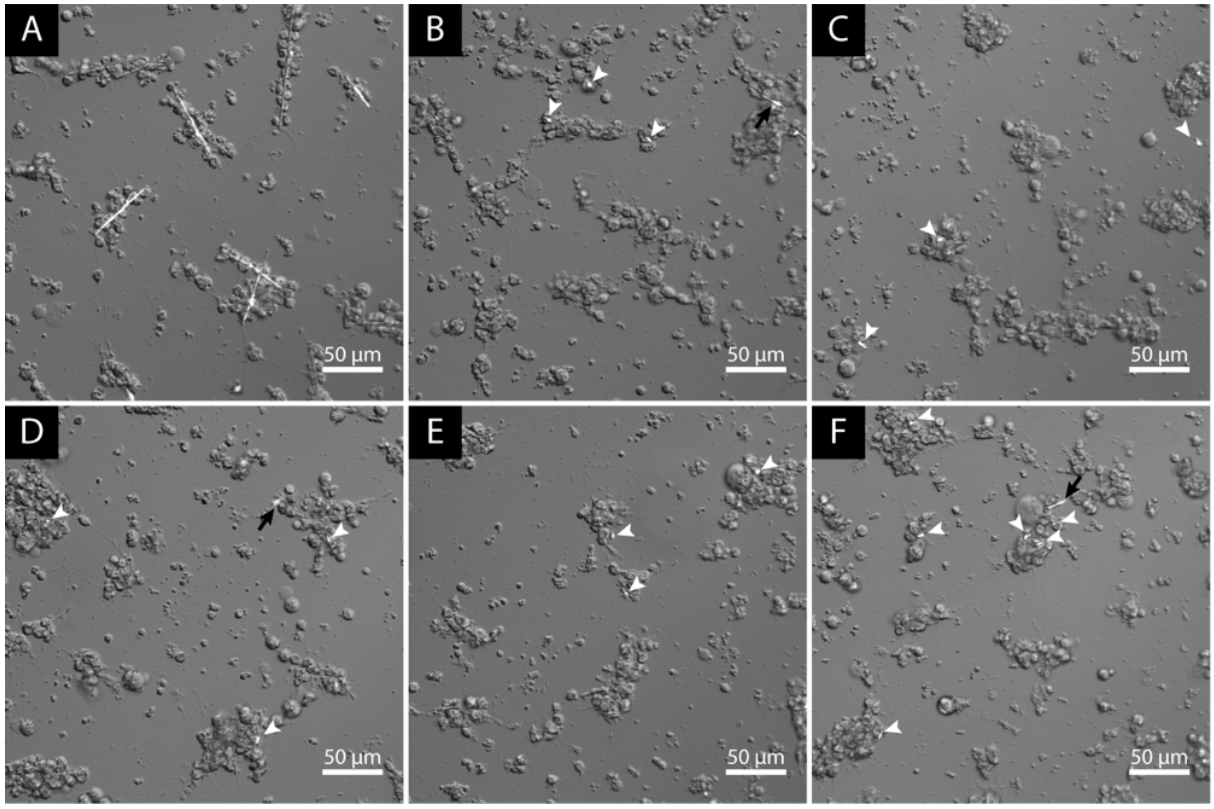

Figure 4.7. Dose-response of PMCs to nocodazole inhibition of tubulin. Cultures were treated from 32 hpf to 56 hpf with (A) 0 μM nocodazole, (B) 2.5 μM nocodazole, (C) 5 μM nocodazole, (D) 10 μM nocodazole, (E) 15 μM nocodazole, (F) and 20 μM nocodazole and observed at 56 hpf (frames are overlays of DIC and pol). Small spicules (black arrows, B,D,F) and granules (white arrowheads, B-F) indicated.

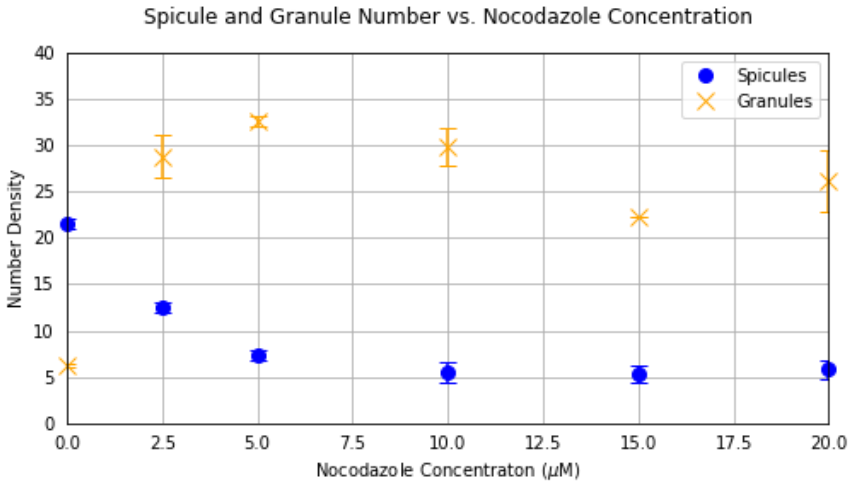

Figure 4.8. Dose-response for treatment of PMCs with nocodazole. Plot of the average number of spicules (circle) and granules (x) observed per image frame (0.44 mm^2) vs. concentration of nocodazole. Error bars indicate +/- one standard deviation of the mean (n = 10). PMCs were treated with nocodazole from 32 to 56 hours hpf and observed at 56 hpf.

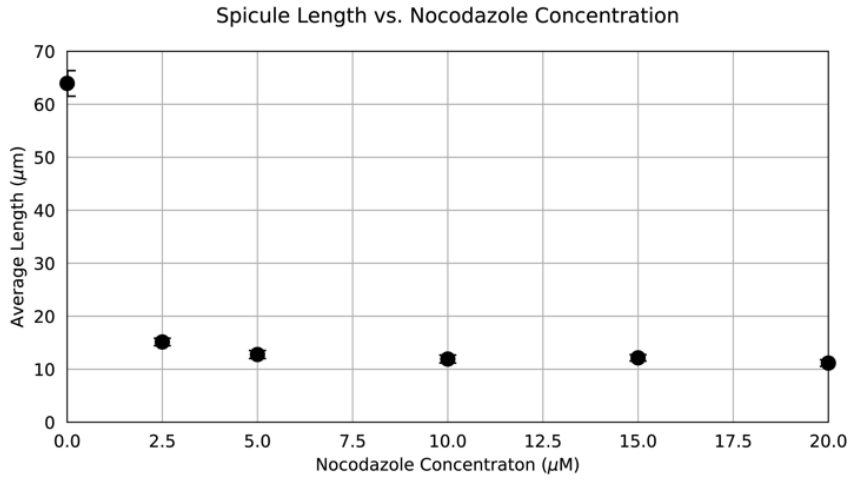

Figure 4.9. Dose-response for treatment of PMCs with nocodazole and effect on spicule length. Plot of the average spicule length observed. Error bars indicate +/- one standard deviation of the mean. PMCs were treated with nocodazole from 32 to 33.5 hours hpf and observed at 56 hpf.

4.2.3. Time series: inhibition of actin and tubulin

The dose-response assays demonstrated that higher concentrations of latrunculin A or nocodazole corresponded with increasingly severe reductions in the number of spicules formed and average spicule length and increases in the number of granules formed. Granule formation seemed independent of actin or tubulin function, whereas elongation of granules into linear

spicules depended heavily on actin and tubulin function, suggesting that growth, not nucleation, depends on the cytoskeleton.

We established a strong relationship between the degree of cytoskeleton disruption and spicule growth. We next sought to determine whether there exists a temporal relation between cytoskeleton inhibition and reduction in spicule growth: viz., we hypothesized that the cytoskeleton is more important for spicule formation at some timepoints than at others. To investigate this hypothesis, we treated cell cultures with latrunculin A or nocodazole at the beginning of spicule formation (32 hpf), at a middle point of spicule growth (38 hpf), after the presence of larger spicules (48 hpf), and imaged at 56 hpf.

In control cell cultures incubated in only 4% (v/v) HS, many linear spicules were visible at 56 hpf (Figure 4.10A, Figure 4.11). Treatment with latrunculin A at 48 hpf slightly decreased (~10%) the number of spicules and increased (~75%) the number of granules (Figure 4.10B, Figure 4.11); in addition, the average spicule length significantly decreased (~45%) (Figure 4.10B, Figure 4.12). Treatment with latrunculin A at 38 hpf resulted in a more severe reduction in the number of spicules (~40%) compared to the previous treatment time and a large increase in the number of granules (~160%) (Figure 4.10C, Figure 4.11), and a large reduction (~50%) in the average spicule length (Figure 4.12). Earlier treatment with latrunculin A at 32 hpf resulted in a decrease (~30%) in the number of spicules from the previous treatment time and no significant change in the number of granules (Figure 4.11), or the average spicule length (Figure 4.12).

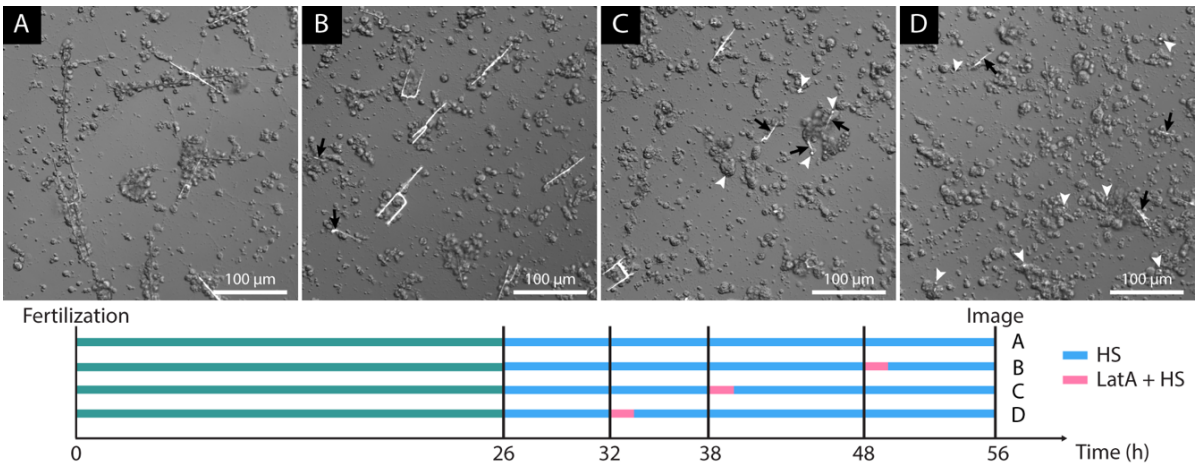

Figure 4.10. Time-response of PMCs to inhibition of actin with latrunculin A. Cultures were incubated from 26 hpf to 56 hpf in (A) 4% (v/v) HS or incubated from 26 hpf to 56 hpf in 4% (v/v) HS and also treated with 50 nM latrunculin A at (B) 48 hpf, (C) 38 hpf, and (D) 32 hpf for 1.5 h. Cultures were imaged at 56 hpf (frames are overlays of DIC and pol). Small linear spicules (black arrows, B-D) and granules (white arrowheads, C-D) indicated.

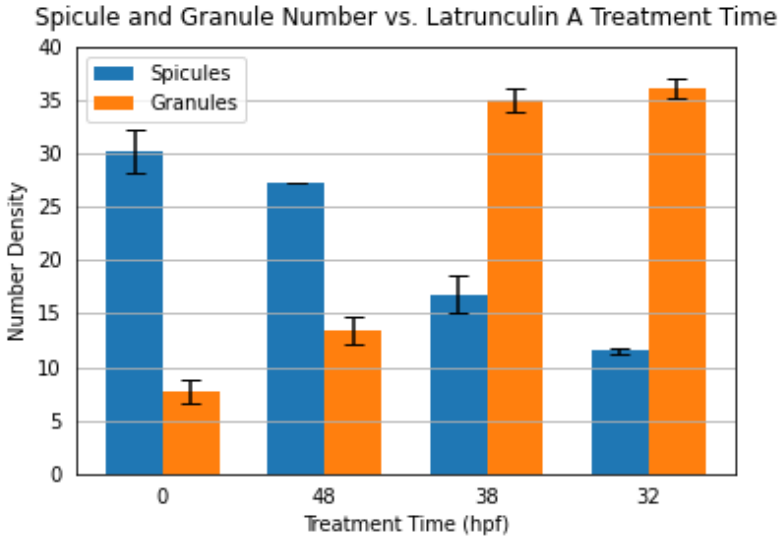

Figure 4.11. Time-response for treatment of PMCs with latrunculin A. Bar plot of the average number of spicules (blue) and granules (orange) per image frame (0.44 mm^2) vs. time of latrunculin A treatment. Error bars indicate +/- one standard deviation of the mean (n = 10). PMCs were treated with latrunculin A for 1.5 h starting at 48, 38, or 32 hpf. Controls were not treated. All cultures were observed at 56 hpf.

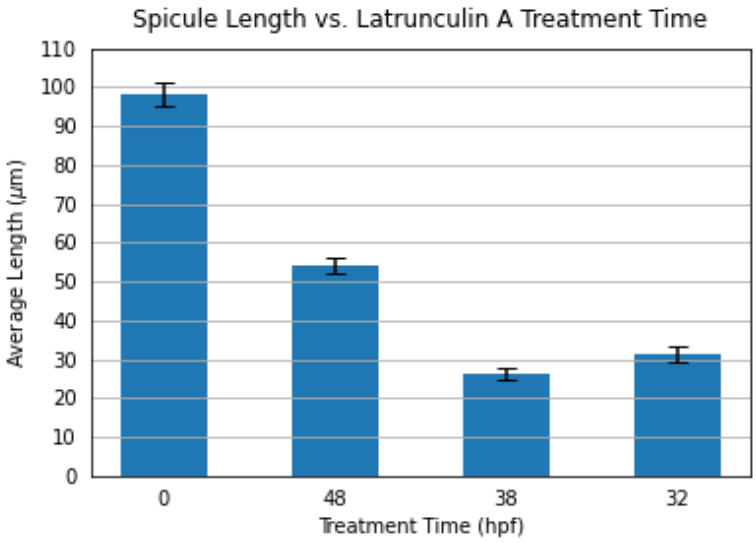

Figure 4.12. Time-response for treatment of PMCs with latrunculin A and effect on spicule length. Bar plot of the average spicule length vs. time of latrunculin A treatment. Error bars indicate +/- one standard deviation of the mean. PMCs were treated with latrunculin A for 1.5 h starting at 48, 38, or 32 hpf. Controls were not treated. All cultures were observed at 56 hpf.

Treatment with nocodazole caused a decrease in the number of spicules like latrunculin A treatment (Figure 4.13, Figure 4.14). As with the latrunculin A series, the control cultures had mostly linear spicules (Figure 4.13A). Treatment with nocodazole at 48 hpf resulted in little decrease (~5%) in the number of spicules and a large increase (~290%) in the number of granules (Figure 4.14), as well as a modest decrease (~5%) in average spicule length (Figure 4.15). Treatment with nocodazole at 38 hpf resulted in a small (~5%) decrease in the number of spicules compared to the previous treatment time and an increase (~40%) in the number of granules (Figure 4.14); however, the average spicule length decreased (~50%) (Figure 4.13C, Figure 4.15). Earlier treatment with nocodazole at 32 hpf resulted in a decrease (~30%) in the number of spicules compared to the previous treatment time and an increase (~80%) in the number of granules (Figure 4.14), as well as a decrease (~20%) in the average spicule length (Figure 4.15).

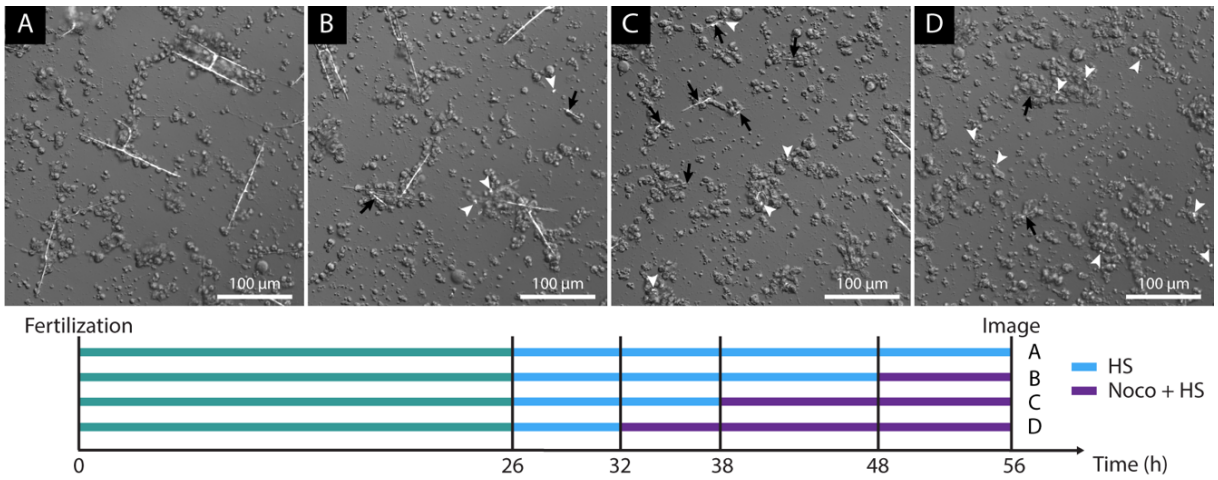

Figure 4.13. Time-response of PMCs to inhibition of tubulin with nocodazole. Cell cultures were incubated from 26 hpf to 56 hpf in (A) 4% (v/v) HS or incubated in 4% (v/v) HS from 26 hpf and with 10 µM nocodazole from (B) 48 hpf, (C) 38 hpf, and (D) 32 hpf to 56 hpf. Cultures were imaged at 56 hpf (frames are overlays of DIC and pol). Small linear spicules (black arrows, B-D) and granules (white arrowheads, B-D) indicated.

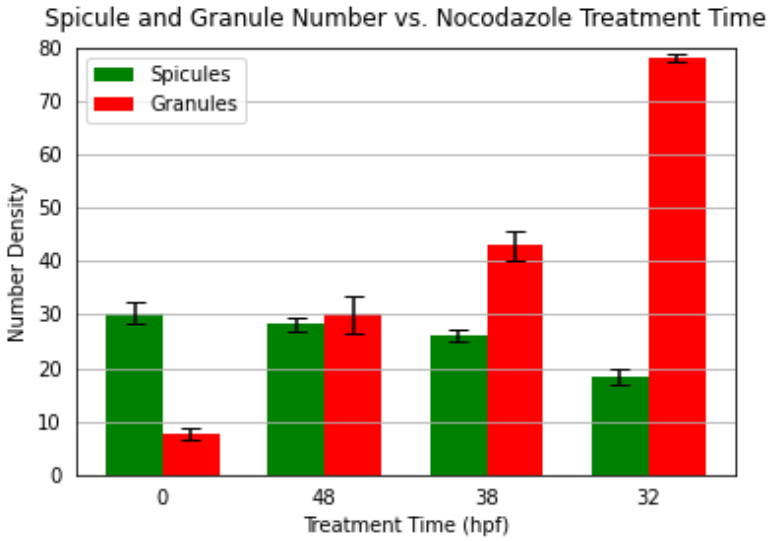

Figure 4.14. Time-response for treatment of PMCs with nocodazole. Bar plot of the average number of spicules (dark) and granules (light) per image frame (0.44 mm^2) vs. concentration of nocodazole. Error bars indicate +/- one standard deviation of the mean (n = 10). PMCs were treated with nocodazole starting at 48, 38, or 32 hpf. Controls were not treated. All cultures were observed at 56 hpf.

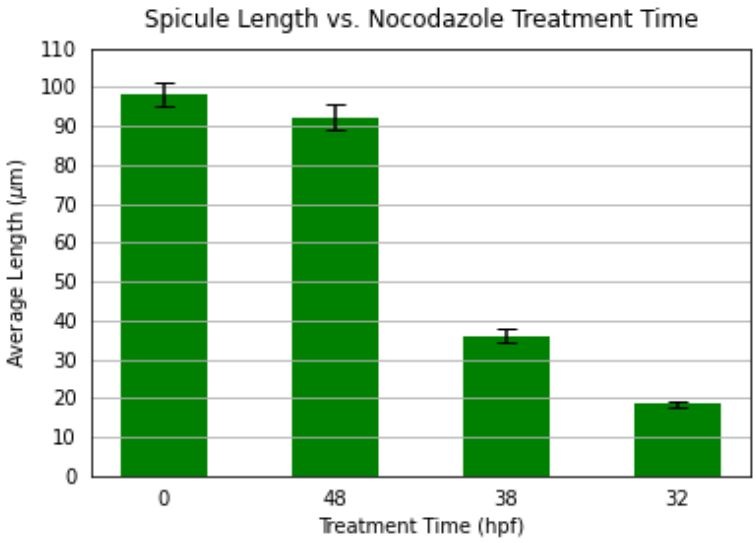

Figure 4.15. Time-response for treatment of PMCs with nocodazole and effect on spicule length. Bar plot of the average spicule length vs. time of nocodazole. Error bars indicate +/- one standard deviation of the mean. PMCs were treated with nocodazole starting at 48, 38, or 32 hpf. Controls were not treated. All cultures were observed at 56 hpf.

The actin and tubulin dose-response experiments discussed in section 4.2.2. produced the same result: increasing the concentration of either inhibitor reduced the number of spicules, increased the number of granules, and reduced the average spicule length, although the trend leveled off for nocodazole beyond a threshold concentration. The time-response experiments of this section revealed a similar relationship, as earlier inhibition times for both inhibitors resulted in a reduction in the number of spicules, an increase in the number of granules, and a decrease in the average spicule length, indicating that continuous cytoskeleton function from the time of granule nucleation is necessary for spicule formation. These findings agree with other research that found a cessation of spicule growth when embryos were treated with pharmacological inhibitors for actin and tubulin. However, for the time-response experiments, it is not certain whether the apparent increase in granules for the cultures inhibited earlier is due to the cells shifting from forming spicules to forming granules, or if those granules had simply already

formed by the time of inhibition. Nevertheless, we can confidently state that early inhibition of the cytoskeleton severely reduces number of linear spicules formed.

4.2.4. Calcein uptake into the spicule in cytoskeleton-inhibited primary mesenchyme cell cultures

The inhibitor concentration and time assays clearly established that disruption of actin or tubulin shuts down the elongation of mature spicules. It is thus certain that inhibition of the cytoskeleton disrupts one or more processes critical to spicule growth. Considering the key processes universal to calcite biomineralization in marine environments, we first examined transport of constituent ions into the mineral. To determine if inhibition of the cytoskeleton disrupts transport of ions to the growing spicule, we used the fluorescent Ca^{2+} chelator calcein. Calcein has been used in prior work with sea urchin PMC cultures and incubation of PMCs with calcein was shown to label the growing parts of the spicule.[87, 125] In our experiments, as first described in section 3.2.4. we introduced bichromatic staining with green calcein and red calcein. Staining with a single color provides information during the pulse treatment but it does not provide before-and-after data, thus comparison between control cultures cultured without inhibitor and inhibited cultures cannot distinguish whether abnormal results are due to abnormal cells or inhibition. To erase this ambiguity, we treated all cultures with one color of calcein, then treated control cultures with the second color and the other set of cultures with both the second color and the inhibitor. If inhibition of the cytoskeleton disrupts uptake of calcium to the mineral, then the second color should not appear in the spicule.

In control cultures, we pulsed cells with calcein red at 51 hpf for 60 min, chased for 60 min, pulsed with calcein green for 60 min, chased for another 60 min, and fixed cells. Spicules

showed labeling of both calcein colors in sequence (Figure 4.16A-D). In contrast, cultures treated with latrunculin A present during the calcein green pulse did not show uptake of calcein green (Figure 4.16E-H). These results agreed with our finding that treatment with latrunculin A shuts down spicule growth.

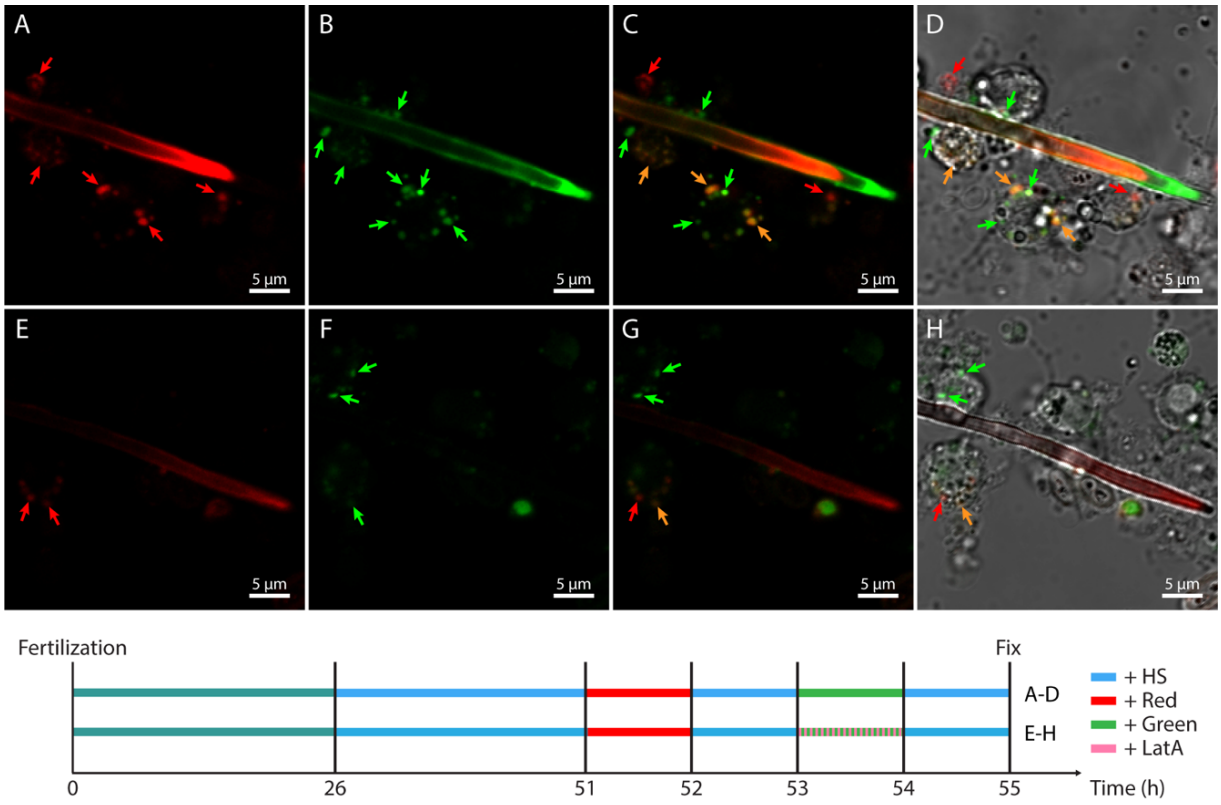

Figure 4.16. Bichromatic calcein staining of spicules with latrunculin A treatment. Cultures were pulsed with calcein red at 51 hpf for 60 min, chased for 60 min, and either (A-D) pulsed with calcein green for 60 min, chased for 60 min, and fixed or (E-H) pulsed with calcein green and 50 nM latrunculin A for 60 min, chased for 60 min, and fixed. (A,E) red channel, (B,F) green channel, (C,G) overlays of red and green channels, and (D,H) overlays of red, green, and BF shown. Vesicles stained with calcein red (red arrows, A,C-D,E,G-H), calcein green (green arrows, B-D,F-H), or both calcein colors (orange arrows, C-D,G-H) indicated.

In the analogous experiments with tubulin inhibition, control cultures incubated with calcein red and calcein green showed spicule labeling of both colors (Figure 4.17A-D). Cultures incubated with nocodazole during the calcein green pulse did not show a reduction in uptake of

calcein green (Figure 4.17E-H). These results did not agree with the finding that inhibition of tubulin severely reduced the number of spicules and average spicule length.

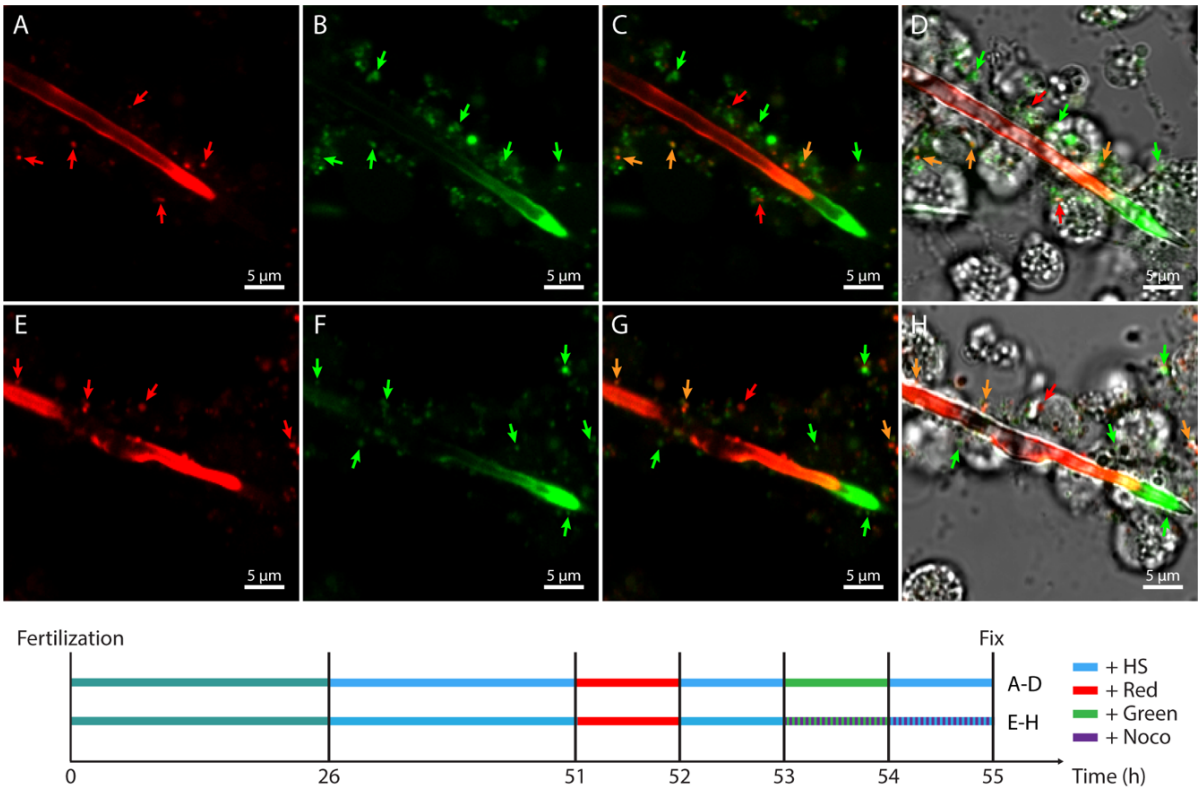

Figure 4.17. Bichromatic calcein staining of spicules with nocodazole treatment. Cultures were pulsed with calcein red at 51 hpf for 60 min, chased for 60 min, and either (A-D) pulsed with calcein green for 60 min, chased for 60 min, and fixed or (E-H) pulsed with calcein green and 10 µM nocodazole for 60 min, chased and incubated with 10 µM nocodazole for 60 min, and fixed. (A,E) red channel, (B,F) green channel, (C,G) overlays of red and green channels, and (D,H) overlays of red, green, and BF shown. Vesicles stained with calcein red (red arrows, A,C-D,E,G-H), calcein green (green arrows, B-D,F-H), or both calcein colors (orange arrows, C-D,G-H) indicated.

The apparent effect on spicule growth caused by actin inhibition and that caused by tubulin inhibition began to differ more from each other in these calcein labeling experiments. As expected, inhibition of actin completely shut down uptake of the second calcein color. This makes sense, because elongation of spicules was stopped by latrunculin A inhibition, so it follows that calcium uptake should also be disrupted. However, tubulin inhibition did not shut down uptake of the second calcein color. This finding suggests that although growth of the spicules is halted by tubulin inhibition, calcium still ends up in the spicule. In this case, it is

possible that thickening of the spicule (i.e., radial growth) occurs since the calcium taken up ends up in the spicule without causing elongation of the spicule. Alternatively, it is possible that tubulin inhibition slows down spicule elongation but does not totally stop it or takes more time to stop it, whereas actin inhibition immediately and totally arrests spicule elongation. This second hypothesis was tested in another experiment in which the second calcein pulse was delayed by a day. In control cultures, we pulsed cells with calcein red at 51 hpf for 60 min, chased for 22 h, pulsed with calcein green for 60 min, chased for another 60 min, and fixed cells. Spicules showed labeling of both calcein colors (Figure 4.18A-D). In contrast, cultures incubated with nocodazole from the time after the calcein red pulse did not show uptake of the second calcein color (Figure 4.18E-H). We thus concluded that nocodazole inhibition of calcein uptake into the spicule has a time delay.

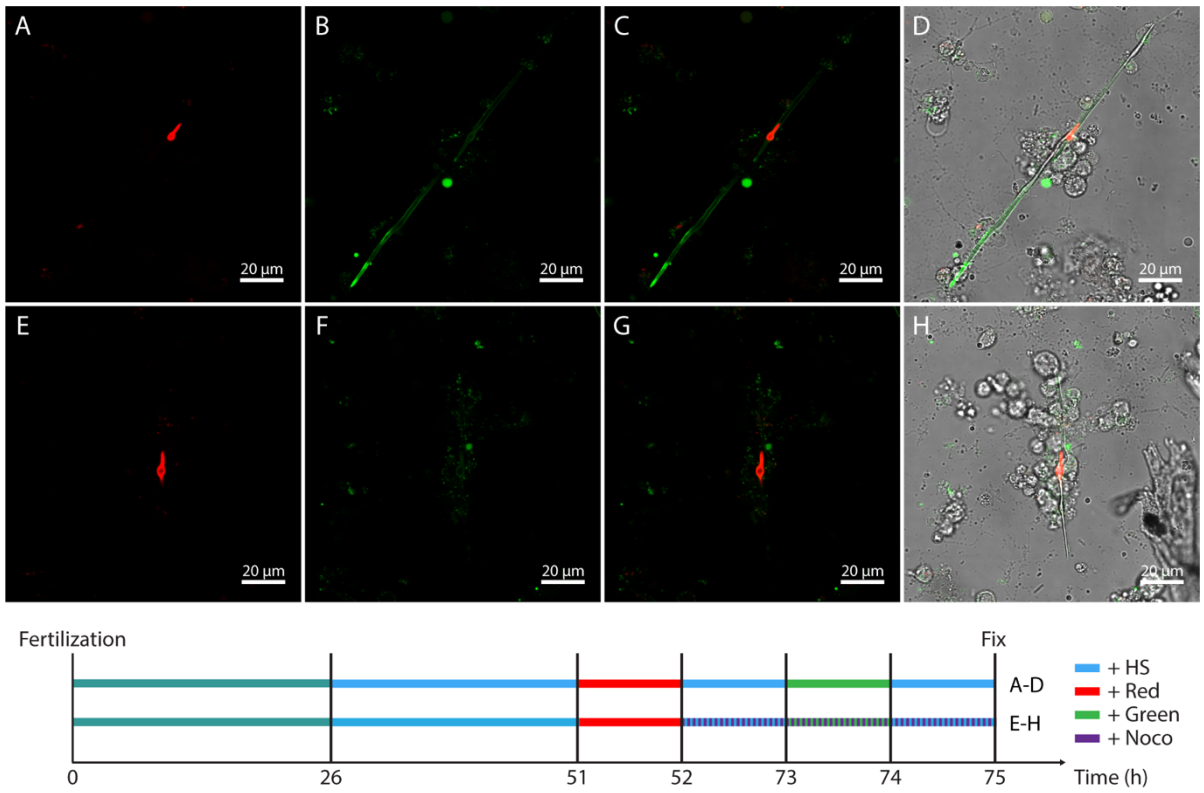

Figure 4.18. Delayed bichromatic calcein staining of spicules with nocodazole treatment. Cultures were pulsed with calcein red at 51 hpf for 60 min and either (A-D) chased for 22 h, pulsed with calcein green for 60 min, chased for 60 min, and fixed or (E-H) chased and incubated in nocodazole for 22 h, pulsed with calcein green and 10 µM nocodazole for 60 min, chased and incubated with 10 µM nocodazole for 60 min, and fixed. (A,E) red channel, (B,F) green channel, (C,G) overlays of red and green channels, and (D,H) overlays of red, green, and BF shown.

4.2.5. Vesicle uptake in cytoskeleton-inhibited primary mesenchyme cell cultures

Simultaneous treatment with calcein and cytoskeleton inhibitors revealed that disruption of actin completely shut down incorporation of calcein in the spicule and disruption of tubulin did after a delay. Since cellular membranes are selectively permeable and calcein cannot diffuse passively through the membrane, calcein must be transported to the growing mineral by biological mechanisms, such as endocytosis and vesicle transport. To determine if inhibition of the cytoskeleton stops vesicle uptake, we again used calcein, which has been previously used to visualize calcium-laden vesicles in sea urchin embryos and PMC cultures.[43, 44, 87, 88, 125] If inhibition of the cytoskeleton shuts down vesicle uptake, then we would expect to see fewer

calcein-labeled vesicles in cultures treated with cytoskeleton inhibitors. To test this hypothesis, we pulsed cells with calcein, calcein and nocodazole, or calcein and latrunculin A for 60 min, and immediately fixed after.

In control plates treated only with calcein, many calcein-containing vesicles were observed (Figure 4.19A). Treatment with latrunculin A during the calcein pulse resulted in a reduction in the area density of calcein-containing vesicles by more than 50% (Figure 4.19B, Figure 4.20). Treatment with nocodazole had an effect of similar magnitude (Figure 4.19C, Figure 4.20).

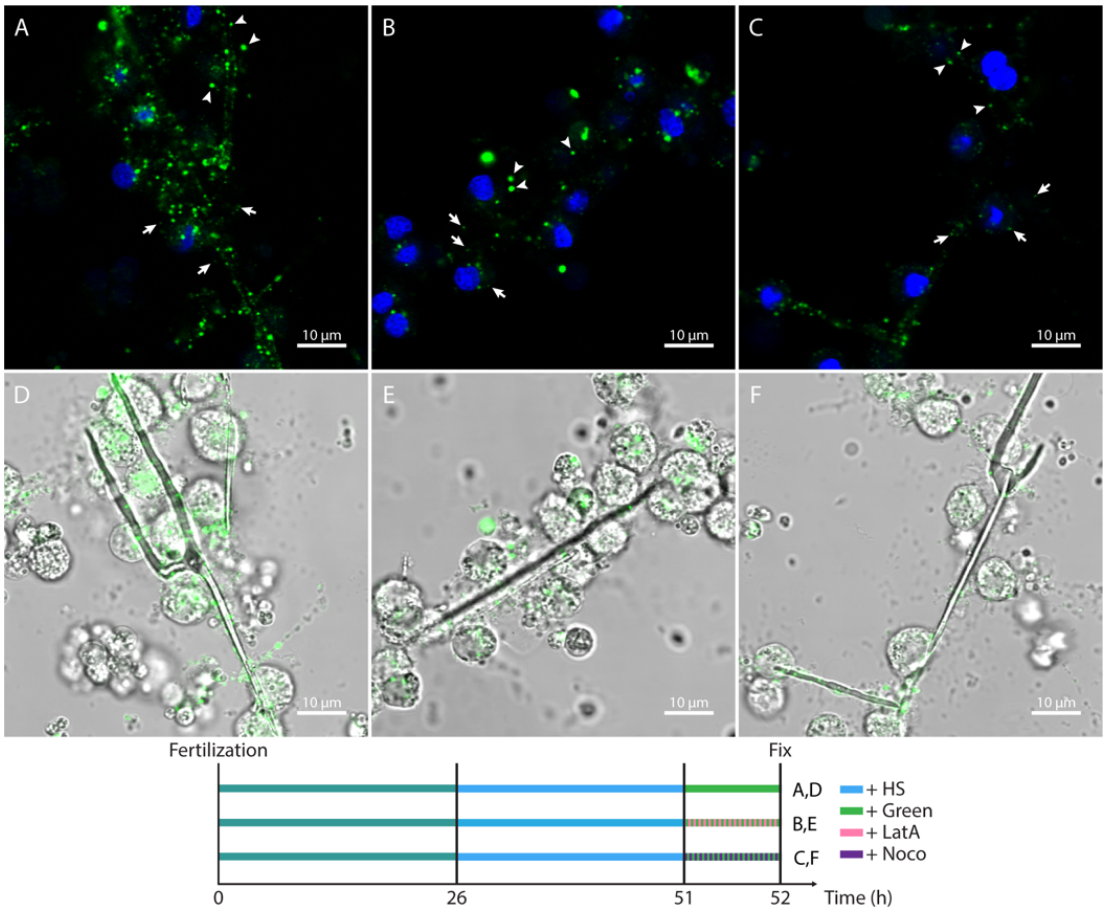

Figure 4.19. Impact of cytoskeletal inhibitors on endocytosis in PMCs. Cells were incubated in 4% (v/v) HS from 26 hpf and pulsed with (A,D) calcein, (B,E) calcein and latrunculin A, or (C,F) calcein and nocodazole from 51 hpf to 52 hpf. Cultures were then fixed with PFA, washed, and nuclei stained with Höchst 33342. (A-C) Green (calcein) and blue (Hoechst 33342) channels, and (D-F) green and BF shown. Small vesicles (A-C, arrows) and large vesicles (A-C, arrowheads) indicated.

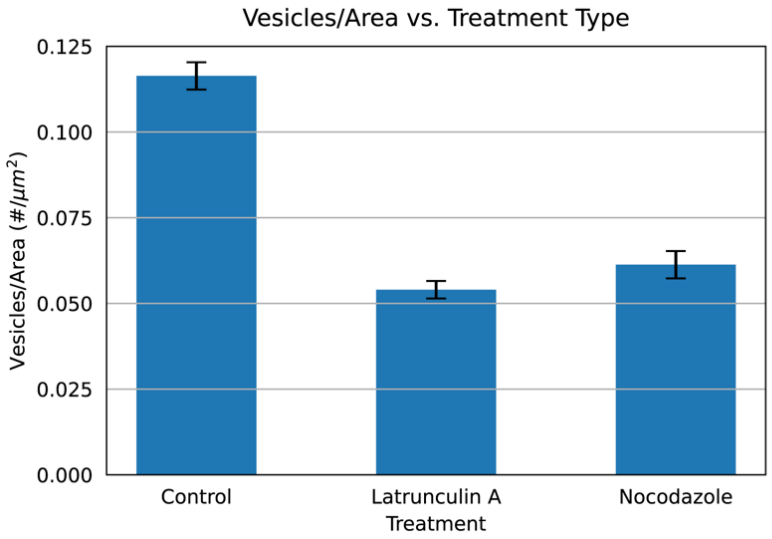

Figure 4.20. Impact of cytoskeletal inhibitors on vesicle number in PMCs. Cells were incubated in 4% (v/v) HS in ASW from 26 hpf and pulsed with calcein, calcein and latrunculin A, or calcein and nocodazole from 51 hpf to 52 hpf and fixed. Error bars indicate +/- one standard deviation of the mean (n = 8).

Both inhibition of actin and tubulin reduced the number of calcein-labeled intracellular vesicles, supporting the hypothesis that inhibition of the cytoskeleton disrupts vesicle uptake necessary to transport ions to the nascent spicule. This is in accord with the well-established relation of the cytoskeleton to uptake and cargo transport: actin polymerization near the cellular membrane remodels the cortex to engulf material and bud off vesicles,[132, 133] and microtubules both provide mechanical forces to assist with vesicle formation and function as the cellular highway used by motor proteins to transport vesicles.[134-136] Inhibition of the cytoskeleton should disrupt these processes, which would hamper the PMCs' ability to transport seawater and ions requisite for spicule formation.

4.2.6. Dynamin, clathrin, and dynein inhibition of primary mesenchyme cell cultures

Actin and tubulin form the bulk of the cytoskeleton, and as previously described, both are known to play roles in vesicle uptake and transport, events that are likely necessary for spiculogenesis. Our results demonstrated that actin is especially important for uptake of calcein

into the spicule and formation of relatively large (~0.5-2 μm) calcium-laden vesicles, suggesting that actin-mediated endocytosis drives spicule formation. However, actin is involved in many, possibly all, endocytotic pathways, such as macropinocytosis and micropinocytosis,[132, 133] so we needed to examine cytoskeleton molecules associated with specific endocytosis pathways to pinpoint exact mechanisms of ion transport to the spicule. Micropinocytosis, such as clathrin-mediated endocytosis and caveolae-mediated endocytosis, has been heavily researched, resulting in the development of many pharmacological inhibitors against its associated molecules;[137] owing to this experimental convenience, we first chose to investigate it as a potential endocytotic mechanism of spicule growth.

Among the major cytoskeleton molecules, dynamin is heavily associated with micropinocytosis, because it catalyzes vesicle fission in clathrin-mediated endocytosis,[138] a type of micropinocytosis. To test whether clathrin-mediated endocytosis is important for spicule formation, we used the inhibitor dynasore, which disrupts dynamin function and has been used with sea urchin embryos to study *nodal*-mediated epigenesis.[139, 140] If perturbation of dynamin function stops spicule growth, this would suggest that micropinocytosis through clathrin-mediated endocytosis is necessary for spiculogenesis.

We treated PMC cultures from 32 hpf to 56 hpf with an ascending concentration series of dynasore. No observable difference between control cultures and inhibited cultures was observed (Figure 4.21). Quantification of image data confirmed that the average number of spicules and granules did not change significantly between control cultures and inhibited cultures (Figure 4.22), and that the average spicule length did not vary significantly between control cultures and inhibited cultures (Figure 4.23).

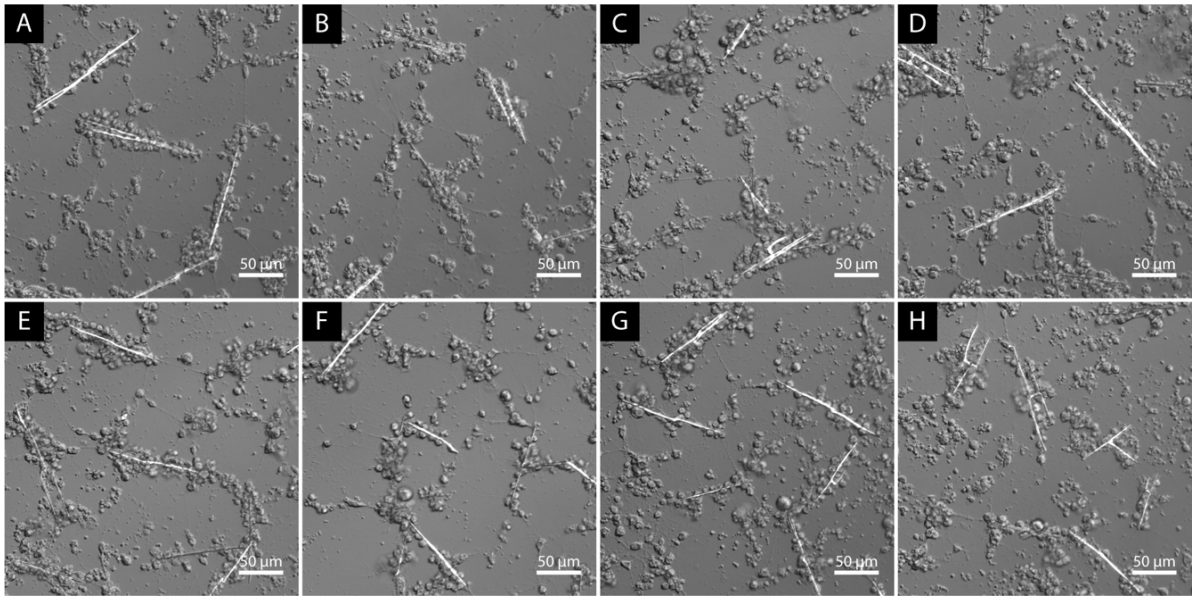

Figure 4.21. Effect of dynamin inhibition on spicule growth. Cultures were incubated from 32 hpf to 56 hpf with (A) 0 µM, (B) 5 µM, (C) 10 µM, (D) 15 µM, (E) 20 µM, (F) 25 µM, (G) 80 µM, (H) and 100 µM dynasore. Imaged at 56 hpf (frames are composites of DIC and pol).

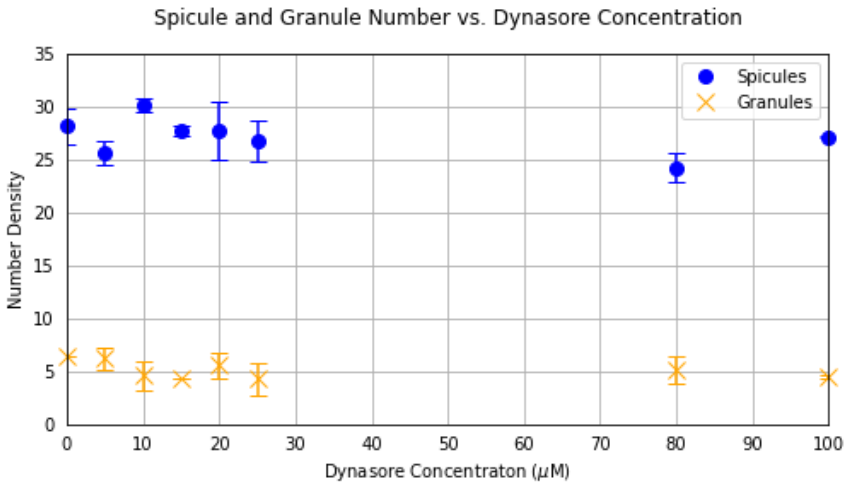

Figure 4.22. Dose-response for treatment of PMCs with dynasore. Plot of the average number of spicules (circle) and granules (x) observed per image frame (0.44 mm^2) vs. concentration of dynasore. Error bars indicate +/- one standard deviation of the mean (n = 10). PMCs were incubated with dynasore from 32 hpf to 56 hpf and observed at 56 hpf.

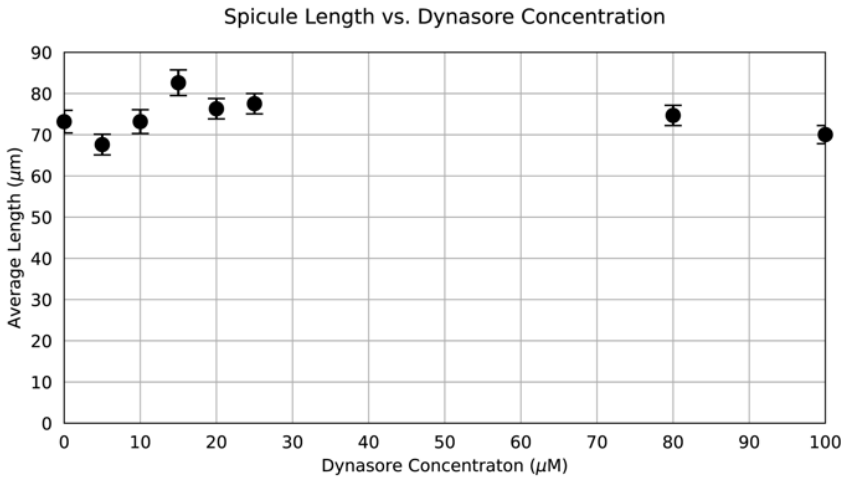

Figure 4.23. Dose-response for treatment of PMCs with dynasore and effect on spicule length. Plot of the average spicule length observed. Error bars indicate +/- one standard deviation of the mean. PMCs were incubated with dynasore from 32 hpf to 56 hpf and observed at 56 hpf).

We sought to further rule out the possibility of clathrin-mediated endocytosis as a pathway for spicule formation by inhibiting clathrin itself rather than accessory proteins such as dynamin. To this end, we employed the inhibitor Pitstop® 2, which interferes with clathrin function by blocking its terminal domain from associating with endocytotic ligands.[141] We thus treated PMC cultures from 32 hpf to 56 hpf with a concentration series of Pitstop® 2 and imaged. We found no observable difference between control and inhibited cultures until the concentration of Pitstop® 2 was increased to 25 μM and 30 μM (Figure 4.24). Quantification of image data showed that the average number of granules did not change significantly with increasing Pitstop® 2 concentration, whereas the average number of spicules decreased by ~50% from culture controls when the Pitstop® concentration was increased to 25 μM and 30 μM (Figure 4.25). The average spicule length varied little between control cultures and inhibited cultures (Figure 4.26).

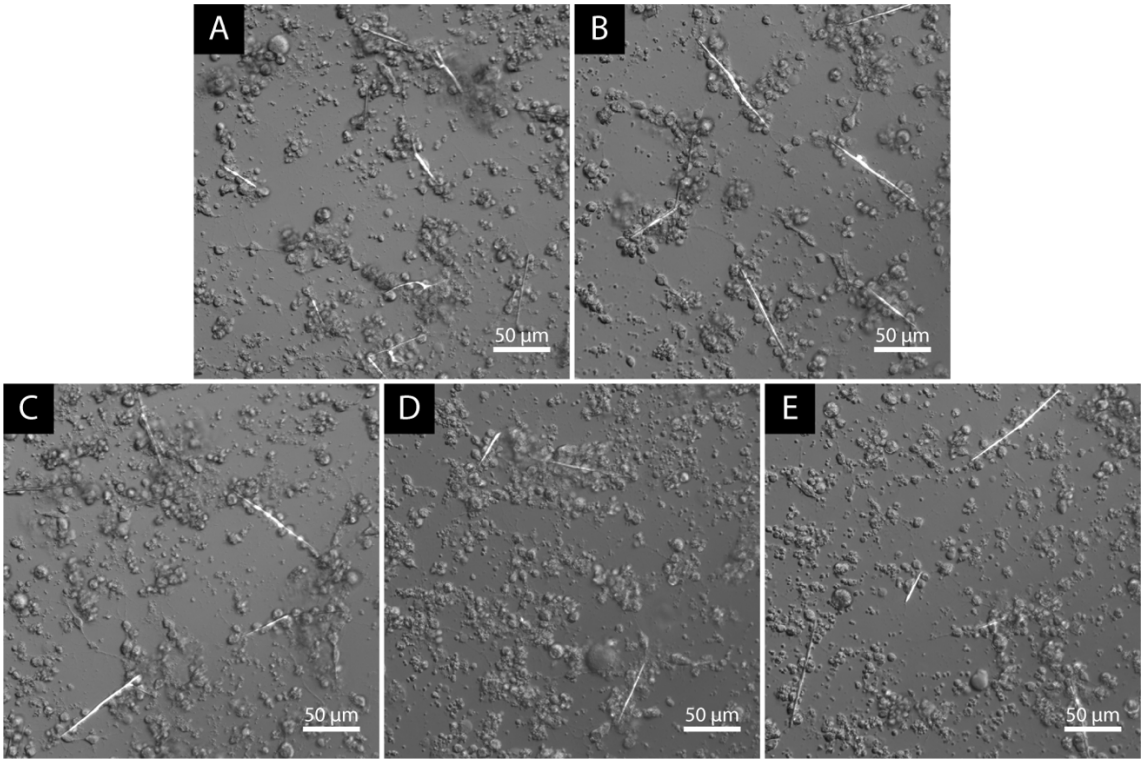

Figure 4.24. Effect of clathrin inhibition on spicule growth. Cultures were incubated from 32 hpf to 56 hpf with (A) 0 µM, (B) 5 µM, (C) 15 µM, (D) 25 µM, and (E) 30 µM Pitstop® 2. Imaged at 56 hpf (frames are composites of DIC and pol).

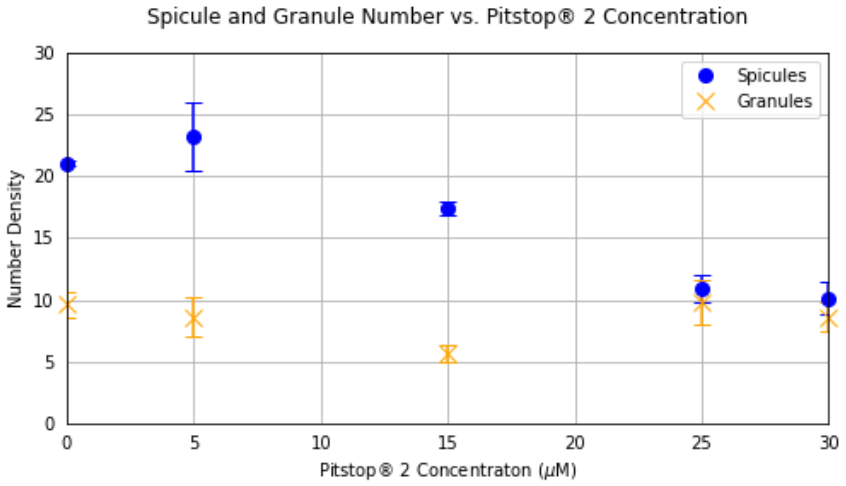

Figure 4.25. Dose-response for treatment of PMCs with Pitstop® 2. Plot of the average number of spicules (circle) and granules (x) observed per image frame (0.44 mm^2) vs. concentration of Pitstop® 2. Error bars indicate +/- one standard deviation of the mean (n = 10). PMCs were incubated with Pitstop® 2 from 32 hpf to 56 hpf and observed at 56 hpf.

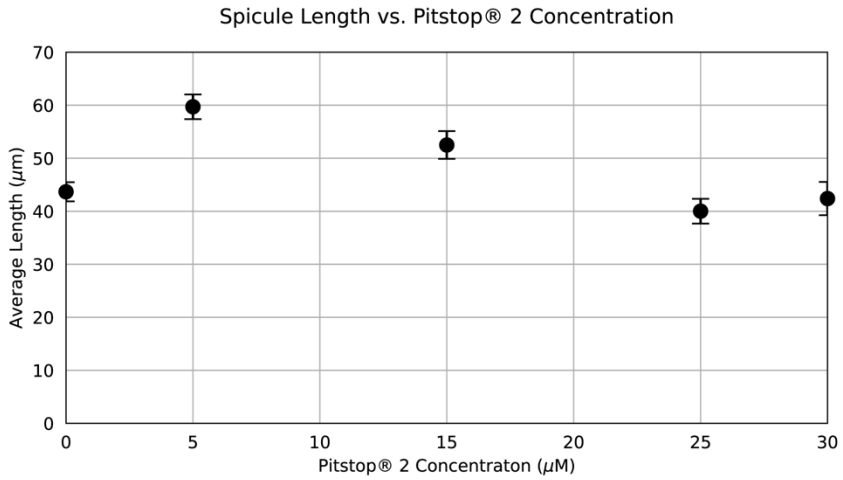

Figure 4.26. Dose-response for treatment of PMCs with Pitstop® 2 and effect on spicule length. Plot of the average spicule length observed. Error bars indicate +/- one standard deviation of the mean. PMCs were incubated with Pitstop® 2 from 32 hpf to 56 hpf and observed at 56 hpf.

Dynasore inhibition of dynamin did not affect spicule formation or elongation, and Pitstop® 2 inhibition of clathrin had only a modest effect on the number of spicules formed, but the latter finding is ambiguous because Pitstop® 2 has been shown to also affect clathrin-independent endocytosis.[142] As such, micropinocytosis through clathrin-mediated endocytosis appears unimportant for spiculogenesis. This agrees with other literature, which have found vesicles on the order of 0.5-1 μm within PMCs in light and electron micrographs,[143] which is larger than the 80-200 nm vesicles associated with micropinocytosis. Our results, taken together with those studies, begin to rule out micropinocytosis and instead suggest that macropinocytosis facilitated by actin and tubulin is the primary cellular driver of mineral uptake into the spicule.

After probing micropinocytosis, we turned our attention to cargo transport as another potential endosomal mechanism for spicule growth. We thus looked into the role of the motor protein dynein, which transports vesicles along microtubules.[135] For this, we used the recently developed inhibitor dynarrestin, which disrupts dynein function and associated endosome movement.[144] We treated PMC cultures from 32 hpf to 56 hpf with an ascending concentration

series of dynarrestin and imaged. We found no observable difference between control cultures and inhibited cultures (Figure 4.27). Quantification confirmed that the number of spicules and granules did not change significantly between control cultures and inhibited cultures (Figure 4.28), and that the average spicule length did not vary significantly between control cultures and inhibited cultures (Figure 4.29). These results weaken the possibility that cargo transport via dynein is a mechanism for spicule growth.

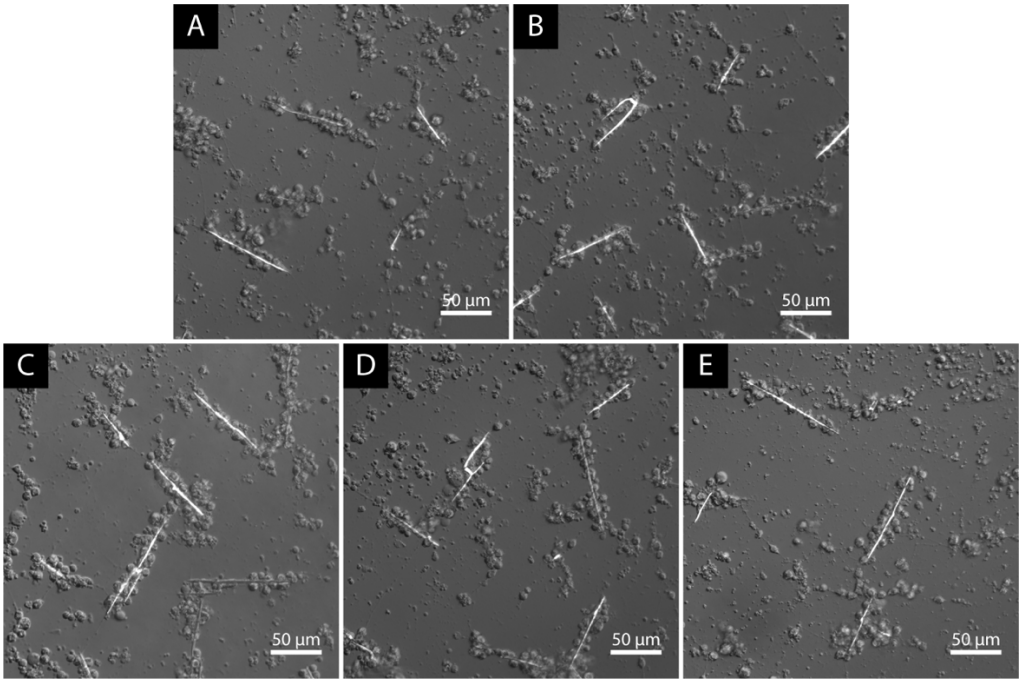

Figure 4.27. Effect of dynein inhibition on spicule growth. Cultures were incubated from 32 hpf to 56 hpf with (A) 0 µM, (B) 6.25 µM, (C) 12.5 µM, (D) 25 µM, and (E) 50 µM dynarrestin. Imaged at 56 hpf (frames are composites of DIC and pol).

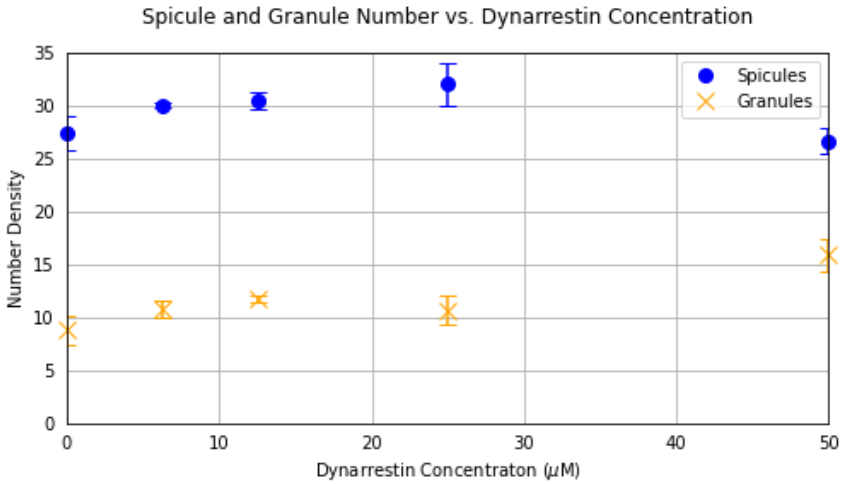

Figure 4.28. Dose-response for treatment of PMCs with dynarrestin. Plot of the average number of spicules (circle) and granules (x) observed per image frame (0.44 mm^2) vs. concentration of dynarrestin. Error bars indicate +/- one standard deviation of the mean (n = 10). PMCs were incubated with dynarrestin from 32 hpf to 56 hpf and observed at 56 hpf.

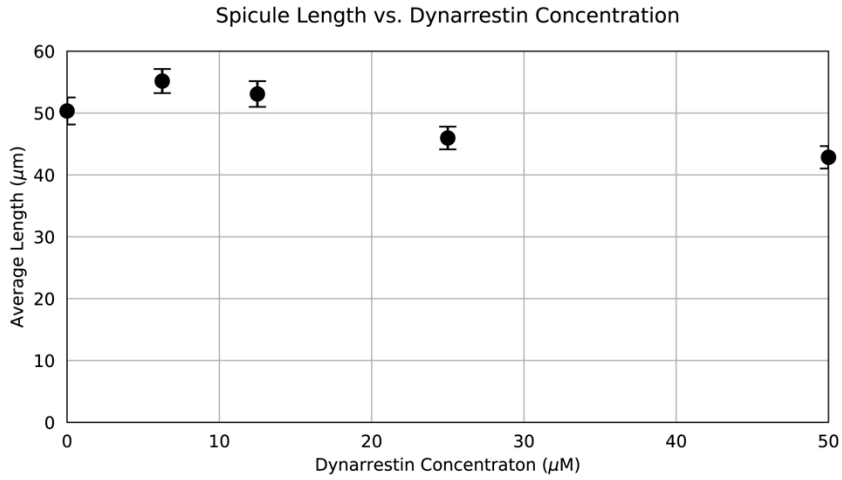

Figure 4.29. Dose-response for treatment of PMCs with dynarrestin and effect on spicule length. Plot of the average spicule length observed. Error bars indicate +/- one standard deviation of the mean. PMCs were incubated with dynarrestin from 32 hpf to 56 hpf and observed at 56 hpf.

4.3. Conclusion

We first examined the roles of the major cytoskeleton molecules actin and tubulin in spicule formation. Confocal fluorescence microscopy revealed that actin and tubulin structures are present throughout spiculogenesis; of particular interest were the actin hotspots at the tips of spicules that suggest an actin polymerization growth front associated with spicule elongation.

The number of spicules decreased, number of granules increased, and the average spicule length decreased as actin and tubulin inhibitor concentrations were increased. The same trends were observed as the inhibition time was varied to be earlier. These results demonstrate that actin and tubulin function are necessary for spicule formation and elongation. Inhibition of actin stopped calcein uptake into the spicule and inhibition of tubulin did after a delay, suggesting that the two molecules have similar roles in spicule growth. Inhibition of actin and tubulin reduced the number of calcein-labeled intracellular vesicles, indicating that both molecules are necessary for vesicle uptake of calcium.

In another series of experiments, we sought more specific mechanisms of vesicle uptake and trafficking to the spicule. Inhibition of dynamin, a molecule associated with micropinocytosis through clathrin-mediated endocytosis, had no effect on spicule formation. Inhibition of clathrin also did not remarkably alter spicule formation. These experiments weaken the notion that micropinocytosis could be a critical pathway for spicule formation. Inhibition of dynein, a motor protein associated with vesicle transport on microtubules, had no effect on spicule formation. Overall, our results indicate that actin and tubulin both play critical roles in spiculogenesis, and that macropinocytosis is the main cellular driver for spicule formation.

4.4. Materials and Methods

4.4.1. Disposables and equipment

Chemicals and consumables:

Unless otherwise noted, all reagents were stored at room temperature (22 °C). NaCl (≥99.5%), $MgSO_4$ (≥99.5%), $CaCl_2 \cdot 2H_2O$ (≥99%), $NaHCO_3$ (≥99%), $MgCl_2 \cdot 6H_2O$ (≥99%), KCl (≥99%) (Avantor, Radnor, PA); concentrated HCl (35-37%), methanol (≥99.5%), dimethyl

sulfoxide (DMSO, anhydrous, ≥99.9%), glycine (≥99%), saponin (8-25% sapogenin), bovine serum albumin (BSA, ≥98%, stored at 4 °C), gentamicin sulfate (≥590 $\mu g \cdot mg^{-1}$, stored at 4 °C), monoclonal mouse anti α-tubulin (DM1α, in 15 mM NaN_3, stored at -20 °C), penicillin + streptomycin (10,000 $units \cdot mL^{-1}$ penicillin, 10,000 $\mu g \cdot mL^{-1}$ streptomycin in 0.85% NaCl, 0.1-μm sterile filtered, stored at -20 °C), dynarrestin (≥98%, stored at 4 °C), Pitstop® 2 (≥98%, stored at -20 °C) (Sigma-Aldrich, St. Louis, MO); NaOH (≥99.1%), paraformaldehyde (PFA, 16% (w/v)), phalloidin Alexa Fluor® 568 conjugate (phalloidin-CF®568, stored in the dark at -20 °C), calcein (≥95%, stored in the dark at 4 °C), goat anti-mouse IgG (H + L) highly cross-adsorbed secondary antibody Alexa Fluor® 633 conjugate (goat anti-mouse-CF®633, 2 $mg \cdot mL^{-1}$ in 5 mM NaN_3, stored in the dark at 4 °C), Hoechst 33342 (10 $mg \cdot mL^{-1}$, stored in the dark at 4 °C), horse serum (sterile, heat inactivated, stored at -20 °C, Gibco Cat #26050) (Thermo Fisher Scientific, Waltham, MA); calcein red™ (≥90%, stored at 4 °C), latrunculin A (≥95%, stored at -20 °C), nocodazole (≥98%, stored at -20 °C), dynasore (≥95%, stored at -20 °C) (Cayman Chemical, Ann Arbor, MI); Instant Ocean® sea salt (Instant Ocean, Blacksburg, VA).

Sterile Falcon tubes (15-, 50-mL), Corning sterile poly(ether sulfone) filter units (0.22-μm, 1-L), Cellvis 29-mm^2 tissue culture dishes with 20-mm^2 #1.5 glass bottom insert (Thermo Fisher Scientific, Waltham, MA); sterile polystyrene serological pipettes (10-, 20-mL) (TPP, Trasadingen, Switzerland); sterile low-binding pipette tips (1-20-, 100-1000-μL,) (Midwest Scientific, Valley Park, MO); Eppendorf® tubes (0.5-, 1.7-mL) (Eppendorf, Hamburg, Germany); dialysis tubing Spectra/Por (12,000-14,000-kDa molecular weight cut-off) (Repligen, Waltham, MA).

Equipment:

Beakers (250-, 500-mL,), graduated cylinders (100-, 500-mL) (Thermo Fisher Scientific, Waltham, MA); Centrifuge 5424, centrifuge 5810R (with temperature control, swing-bucket rotor with four 500-mL buckets, conical 50- and 200-mL inserts), single-channel adjustable volume pipettes (2-20-, 20-200-, 100-1000-µL) (Eppendorf, Hamburg, Germany); Portable Pipet-Aid® XP2 Pipette Controller (Drummond Scientific, Broomall, PA); vacuum aspirator with trap (Sigma-Aldrich, St. Louis, MO).

Solutions:

Unless otherwise noted, all aqueous solutions were prepared with ultra-pure water (UPW, $\rho = 18.2\ M{\cdot}\Omega{\cdot}cm$) dispensed by a Barnstead NanoDiamond UF + UV purification unit and stored at 15 °C. A solution of 2.5 M NaOH was prepared by dissolving 50 g NaOH in 500 mL UPW. A solution of 1.0 M HCl was prepared by diluting 20.75 mL concentrated HCl in a 250-mL volumetric flask with UPW.

Since acidic media dissolves the spicule, the pH of all solutions used with cell cultures was checked and adjusted to ~8.0 by titration with 2.5 M NaOH, if necessary. Artificial seawater (ASW) was prepared with the following final concentrations: 0.48 M NaCl, 0.10 M $CaCl_2{\cdot}2H_2O$, 0.01 M KCl, 0.03 M $MgSO_4$, 0.027 M $MgCl_2{\cdot}6H_2O$, and 0.002 M $NaHCO_3$. ASW was filtered with a 0.22-µm Corning filter.

A volume of 100 mL horse serum was dialyzed twice against 1 L ASW overnight at room temperature (molecular weight cutoff = 12,000-14,000 kDa), sterile filtered with a 0.22-µm Corning filter, and separated into 4 mL-aliquots that were stored at -20 °C.

A 10 μM stock solution of latrunculin A was prepared in DMSO and separated into 50 μL aliquots that were stored at -20 °C. A 10 mM stock solution of nocodazole was prepared in DMSO and separated into 30 μL aliquots that were stored at -20 °C. A 15 mM stock solution of dynasore was prepared in ASW and separated into 100 μL aliquots that were stored at -20 °C. A 10 mM stock solution of dynarrestin was prepared in DMSO and separated into 100 μL aliquots that were stored at -20 °C. A 10 mM stock solution of Pitstop® 2 was prepared in DMSO and separated into 100 μL aliquots that were stored at -20 °C. A 2 $mg \cdot mL^{-1}$ calcein stock solution was prepared by dissolving 100 mg calcein in 50 mL ASW and was stored in the dark at 4 °C (to avoid confusion with other calcein colors, solutions containing calcein are henceforth referred to as calcein green). A 1 $mg \cdot mL^{-1}$ calcein red™ stock solution was prepared by dissolving 1 mg calcein red™ in 1 mL UPW and was stored in the dark at 4 °C (solutions containing calcein red™ are henceforth referred to as calcein red).

0.30% (w/v) saponin was prepared by dissolving 45 mg saponin in 15 mL ASW. A 0.05% (w/v) saponin solution was prepared by diluting the 0.30% (w/v) saponin solution 1:6 in ASW. A 3% (w/v) BSA blocking solution was prepared by dissolving 0.45 g BSA in 15 mL 0.30% (w/v) saponin. 300 units (U) of phalloidin-CF®568 were dissolved in 1.5 mL of methanol to produce a 200 $U \cdot mL^{-1}$ stock solution, which was aliquoted and stored at -20 °C. A stock solution of 100 $\mu g \cdot mL^{-1}$ Hoechst 33342 was prepared in ASW and stored at 4 °C.

4.4.2. Micromere isolation and primary mesenchyme cell culture

Sea urchins were purchased from Marinus Scientific (Long Beach, CA) and South Coast Bio-Marine LLC (San Pedro, CA) and maintained in Instant Ocean® seawater at 15 °C. All experiments involving PMC culture were performed in a climate-controlled room at 15 °C. Glass

bottom plates used in PMC culture were acid washed as described in section 2.2.3. Micromeres were isolated and seeded at a density of ~100,000 cells per glass bottom plate as described in section 2.1.5.

ASW used in PMC culture was supplemented with 100 μg·mL^{-1} gentamicin sulfate and 100 U·mL^{-1} penicillin + 100 μg·mL^{-1} streptomycin (ASWGPS). Culture media was prepared by diluting horse serum to 4% (v/v) in ASWGPS (for brevity, this culture media is henceforth referred to as 4% (v/v) HS, the "in ASWGPS" implied). PMCs were cultured in these media as described in section 2.1.5.

4.4.3. Inhibitor treatment of primary mesenchyme cell cultures

The latrunculin A stock solution was diluted 1:800, 1:400, 1:200, 1:133, and 1:100 in 4 mL 4% (v/v) HS to achieve concentrations of 12.5 nM, 25 nM, 50 nM, 75 nM, and 100 nM. Cell cultures were washed (1×, 2 mL) with and incubated in these media for 90 min at 15 °C. Latrunculin A was removed post treatment by washing (1×, 2 mL) with 4% (v/v) HS and were incubated in these media at 15 °C.

The nocodazole stock solution was diluted 1:4000, 1:2000, 1:1000, 1:667, and 1:500 in 4 mL 4% (v/v) HS to achieve concentrations of 2.5 μM, 5 μM, 10 μM, 15 μM, and 20 μM. Cell cultures were washed (1×, 2 mL) with and incubated in these media at 15 °C.

The dynasore stock solution was diluted 1:15 to a solution of 1,000 μM which was diluted 1:200, 1:100, 1:67, 1:50, 1:40, 1:12.5, and 1:10 in 4 mL 4% (v/v) HS to achieve concentrations of 5 μM, 10 μM, 15 μM, 20 μM, 25 μM, 80 μM, and 100 μM. Cell cultures were washed (1×, 2 mL) with and incubated in these media at 15 °C.

The dynarrestin stock solution was diluted 1:1600, 1:800, 1:400, and 1:200 in 4 mL (v/v) HS to achieve concentrations of 6.25 μM, 12.5 μM, 25 μM, and 50 μM. Cell cultures were washed (1×, 2 mL) with and incubated in these media at 15 °C.

The Pitstop® 2 stocks solution was diluted 1:2000, 1:667, 1:500, and 1:333 in 4 mL (v/v) HS to achieve concentrations of 5 μM, 15 μM, 20 μM, and 30 μM. Cell cultures were washed (1×, 2 mL) with and incubated in these media at 15 °C.

4.4.4. Calcein staining of primary mesenchyme cell cultures

Calcein staining was carried out as described in section 3.2.4. For bichromatic calcein staining, cells were pulsed 2 h with calcein red, chased 2 h with 4% (v/v) HS, pulsed 2 h with calcein green, chased 2 h with 4% (v/v) HS, and fixed as described in section 2.2.3. . For vesicle quantification experiments, cell cultures were pulsed with calcein green for 1 hr and immediately fixed and stained with Hoechst 33342 as described in section 2.2.3.

4.4.5. Fluorescent staining of primary mesenchyme cell cultures

For actin staining, cells were fixed, permeabilized, and stained with phalloidin-CF®568 as described in section 2.2.3.

For tubulin staining, cells were fixed, permeabilized, and blocked with BSA as described in section 2.2.3. The DM1α antibody stock solution was then diluted 1:400 in 0.3% (w/v) BSA in 0.05% (w/v) saponin in ASW. All media were removed from the cultures and 200 μL of the working primary antibody solution were gently layered onto each plate. Cultures were incubated overnight at 4 °C and then washed with 0.05% (w/v) saponin in ASW (3×, 2 mL). A working solution of goat anti-mouse-CF®633 was prepared by diluting the antibody stock solution 1:400 in 3% (w/v) BSA in 0.05% (w/v) saponin in ASW. Media were removed and 200 μL of the

secondary antibody working solution were gently layered on top of each plate. Cultures were incubated for 1 hr at 15 °C and washed with ASWGSP (1×, 2 mL).

Cells were counterstained for nuclei with Hoechst 33342 as described in section 2.2.3.

4.4.6. Imaging of primary mesenchyme cell cultures

Live cell cultures were imaged on a Leica DM6000b light microscope using an inverted light path and either brightfield (BF), differential interference contrast (DIC), or dark-field (polarized) light contrast. Fluorescently labeled and fixed cell cultures were imaged using a Leica TCS SP8 laser scanning confocal microscope. Hoechst 33342 fluorescence was obtained with an excitation wavelength of 405 nm and capture of 415-500 nm bandwidth. Calcein green fluorescence was obtained with an excitation wavelength of 488 nm and capture of 500-570 nm bandwidth. Phalloidin-CF®568 and calcein red fluorescence were obtained with an excitation wavelength of 552 nm and capture of 560-650 nm bandwidth. Goat anti-mouse-CF®633 fluorescence was obtained with an excitation wavelength of 633 nm and capture of 645-750 nm bandwidth. Images were adjusted for brightness and contrast using Fiji.[145]

4.4.7. Image analysis and spicule and vesicle quantification

For quantifying the effect of cytoskeleton inhibition on spicule formation, five representative image frames were chosen for each treatment group and spicules and granules were counted using Cell Counter in Fiji; spicule lengths were also recorded in Fiji. Statistical analysis was performed in Microsoft Excel. The average and standard error were determined for each treatment group and results were plotted using Matplotlib.[146]

For quantifying the effect of cytoskeletal inhibition on calcein vesicle uptake, eight representative image frames were chosen for each treatment group. A perimeter was drawn

around cells or groups of cells that were in focus, the area was recorded, and the number of vesicles within the area was counted using Cell Counter in Fiji. From these data, the number of vesicles per unit area was calculated for each image frame, the average and standard error were determined for each treatment group, and results were plotted using Matplotlib.

Chapter 5. Mapping Organic Matrix Proteins in the Spicule

5.1. Introduction

The sea urchin embryo's intricate endoskeleton is a remarkable case of biologically directed single crystal growth. As a brief recapitulation, during the late gastrula stage, the primary mesenchyme cells (PMCs) fuse their membranes to form the syncytium, which acts as the delineated space in which mineral forms.[37, 38] An initial granule is deposited and grows along the three *a*-axes of calcite. Later, two of the body rods change directions 90° into the *c*-axis of calcite. The final spicule is smooth, curved, single crystalline calcite that has a high degree of magnesium substitution (~5%) and a small percentage of occluded organic matrix (~0.1%).[147]

Although PMC morphogenesis has been worked out in elaborate detail, the mechanisms of spicule growth remain murky. Much work has elucidated the role of amorphous precursor phases in building the mineral. For example, X-ray diffraction (XRD) and X-ray absorption spectroscopy (XAS) studies suggest that the immature spicule contains hydrated amorphous calcium carbonate ($H_2O \cdot ACC$).[42, 148] Later work combining photoelectron emission spectromicroscopy (PEEM) with X-ray absorption near-edge structure (XANES) spectroscopy suggest that as the spicule matures, $H_2O \cdot ACC$ is replaced by anhydrous ACC, which is later replaced by calcite as the dominant $CaCO_3$ polymorph, suggesting that the spicule grows by addition of ACC that eventually crystallizes into calcite.[149, 150] The Joester group used Sr^{2+} labeling combined with XAS to study the spicule and found that the spicule possibly grows through deposition of ACC that is replaced by disordered calcite, which is finally replaced by calcite.[151] These hypotheses were supported by correlative fluorescence microscopy and

cryogenic scanning electron microscopy (cryo-SEM) experiments that revealed vesicles laden with nanospheres, likely ACC, within the mineralizing PMCs.[43, 44]

Evidence for spicule growth via deposition of ACC through vesicle transport exists, but the molecular toolkit used by the PMCs to control crystal growth still eludes understanding. An early suspect was the organic matrix occluded within the spicule that can be separated out by dissolution of the mineral. Using 1D gel electrophoresis of spicule matrix extracts, several research groups independently found multiple (8-10) molecular weight bands corresponding to the major protein constituents of the matrix.[152, 153] Higher resolution 2D gel electrophoresis expanded the number of proteins to around 50,[154] and twenty-first century mass spectrometry-based proteomics enumerated 231 proteins, the most abundant of them including SM30, SM50, MSP-130130, and PM27.[47]

The functions of the spicule matrix proteins in mineral formation have been interrogated through techniques such as gene knockdown and *in vitro* crystal growth. Knockdown of SM50 in *S. purpuratus* embryos (and of the SM50 ortholog LSM34 in *L. pictus*) resulted in total cessation of both granule nucleation and spicule elongation, proving that this protein is absolutely critical for spicule formation.[155, 156] In contrast, knockdown of SM30 had no effect on spicule formation, suggesting a more subtle function.[157] *In vitro* growth of mineral from supersaturated $CaCO_3$ and Mg^{2+} solution supplemented with spicule matrix extracts isolated from immature spicules with high percentages of amorphous content resulted in stable ACC, whereas mineral growth from solution supplemented with extracts taken from mature crystalline spicules did not.[48] Later, analysis of XANES-PEEM spectra collected from *in vitro* $CaCO_3$ growth assays specifically found that the presence of SM50 in solution stabilizes ACC.[149] Other researchers determined that

recombinant SM30 in solution appears as hydrogels and induces supersaturated $CaCO_3$ solutions to form calcite single crystals with elongated and nanotextured sides.[158] Overall, these types of experiments can provide useful data but are expensive, as they require generation of morpholinos specific for the gene of interest and recombinant synthesis of proteins. Furthermore, the trends observed usually elicit multiple explanations (e.g., knockdown of a gene can affect other cells that also interact with the skeletogenic PMCs, resulting in indirect effects on spicule formation), obfuscating analysis.

Localization of macromolecules, through immunolabeling combined with optical or electron microscopy, is straight forward to execute in the laboratory while providing evidence of protein function. Fluorescent labeling of spicule matrix proteins SM30, SM50, and PM27 in embryos, PMC cultures, and isolated and etched spicules revealed the presence of all three proteins near and embedded within the spicule.[86] However, their spatiotemporal distributions throughout spicule formation were different, suggesting unique roles for each. Immunolabeling via gold nanoparticles combined with transmission electron microscopy (TEM) revealed the presence of MSP-130130 in the membranous spicule compartment[105] and SM30 and SM50 in the PMCs' protein secretory pathway and within the spicule matrix.[106] A similar approach leveraging immunolabeling via gold nano particles combined with SEM successfully found SM30 and SM50 occluded in fractured and etched spicules.[159, 160]

Optical microscopy of fluorescently immunolabeled embryos and PMC cultures is limited by the inherent ambiguity in correctly interpreting what is inside the mineral and what is on the membrane surrounding the spicule. Electron microscopy can resolve such differences, but dissolution of the mineral during TEM sample preparation is problematic, and the jagged

topology of etched fracture surfaces observed under SEM complicates interpretation of spatial information. Kitajima and Urakami surmounted these challenges with an elegant technique: by carefully dissolving the spicule on a membrane in a vacuum blotting apparatus and staining the immobilized organic matrix with targeted antibodies, the spicule matrix proteins can be imaged to obtain accurate 2D spatial information.[107] This technique, referred to as spicule blot, was used effectively to demonstrate that SM50 and SM30 localize differently in *H. pulcherrimus* spicules, with SM50 more concentrated in the body rod tip and triradiate portion of the spicule and SM30 present throughout the body rod.

In this project, we sought to leverage the spicule blot technique combined with our imaging capabilities and *in vitro* PMC culture system to map the proteins that form the organic matrix occluded within the spicule. Data collected using this method revealed that the distributions of two key spicule matrix proteins in *S. purpuratus* were similar to those reported by Kitajima and Urakami for *H. pulcherrimus*, indicating that protein localizations are similar across species, and that spicule matrix protein distributions were similar in spicules isolated from PMC cultures and embryos, suggesting a common molecular toolkit for crystal growth. Furthermore, the robustness and reproducibility of results herein demonstrates the technical success of this approach, which can be applied to other sea urchin biomineral organic matrix protein studies or to other organisms' biomineral proteins.

5.2. Results and Discussion

Our primary goal was to uncover the spatial distribution of organic matrix proteins within the spicule. To achieve this, we employed the aforementioned spicule blot procedure combined with immunofluorescence staining and imaging. Using a blotting apparatus, spicules isolated

from pluteus stage embryos were dissolved on blotting membrane with gentle vacuum to immobilize the organic matrix, which was then stained with primary antibodies specific for either of the major spicule matrix proteins SM30B/C or SM50. Afterwards, spicule blot samples were incubated with Alexa Fluor®-conjugated secondary antibodies and imaged. Control specimens were incubated with only the secondary antibody.

Control samples incubated with only the secondary antibody showed negligible fluorescence intensity (Figure 5.1). In striking contrast, fluorescent immunolabeling of spicule blot samples for SM30B/C or SM50 clearly revealed immobilized spicule matrix proteins describing the form of the pluteus spicule (Figure 5.2). Closer inspection discriminated that staining for the two spicule matrix proteins differed markedly. Spicule blot samples stained for SM30B/C showed relatively homogenous intensity throughout the body rod of the spicule (Figure 5.2A,C). This contrasted with spicule blot samples immunolabeled for SM50, for which fluorescence signal in the body rod was heterogeneous, with maximum intensity near the thick region around the tip and gradually tapering off towards the middle section (Figure 5.2B,D). Spicule blot samples stained for SM50 also typically displayed significant fluorescence intensity in the triradiate rudiment region of the spicule (Figure 5.2B,D). On the other hand, spicule blot samples stained for SM30B/C usually did not display high fluorescence intensity in the triradiate rudiment region (Figure 5.2A), although dim fluorescence in that area occasionally appeared (Figure 5.2C).

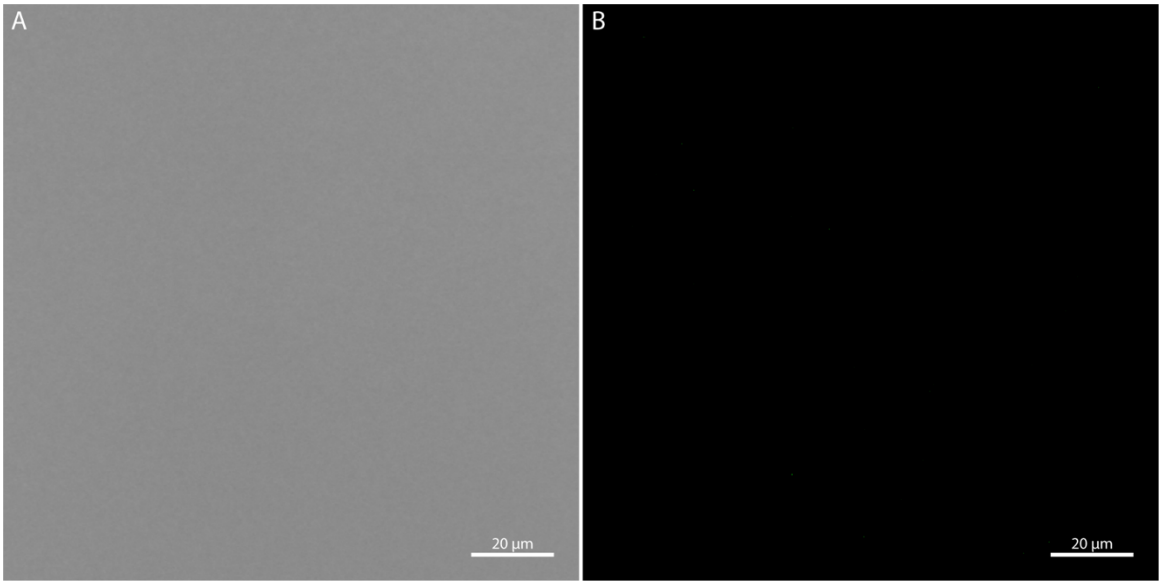

Figure 5.1. Control plates incubated with only secondary antibody. (A) BF and (B) green channels shown.

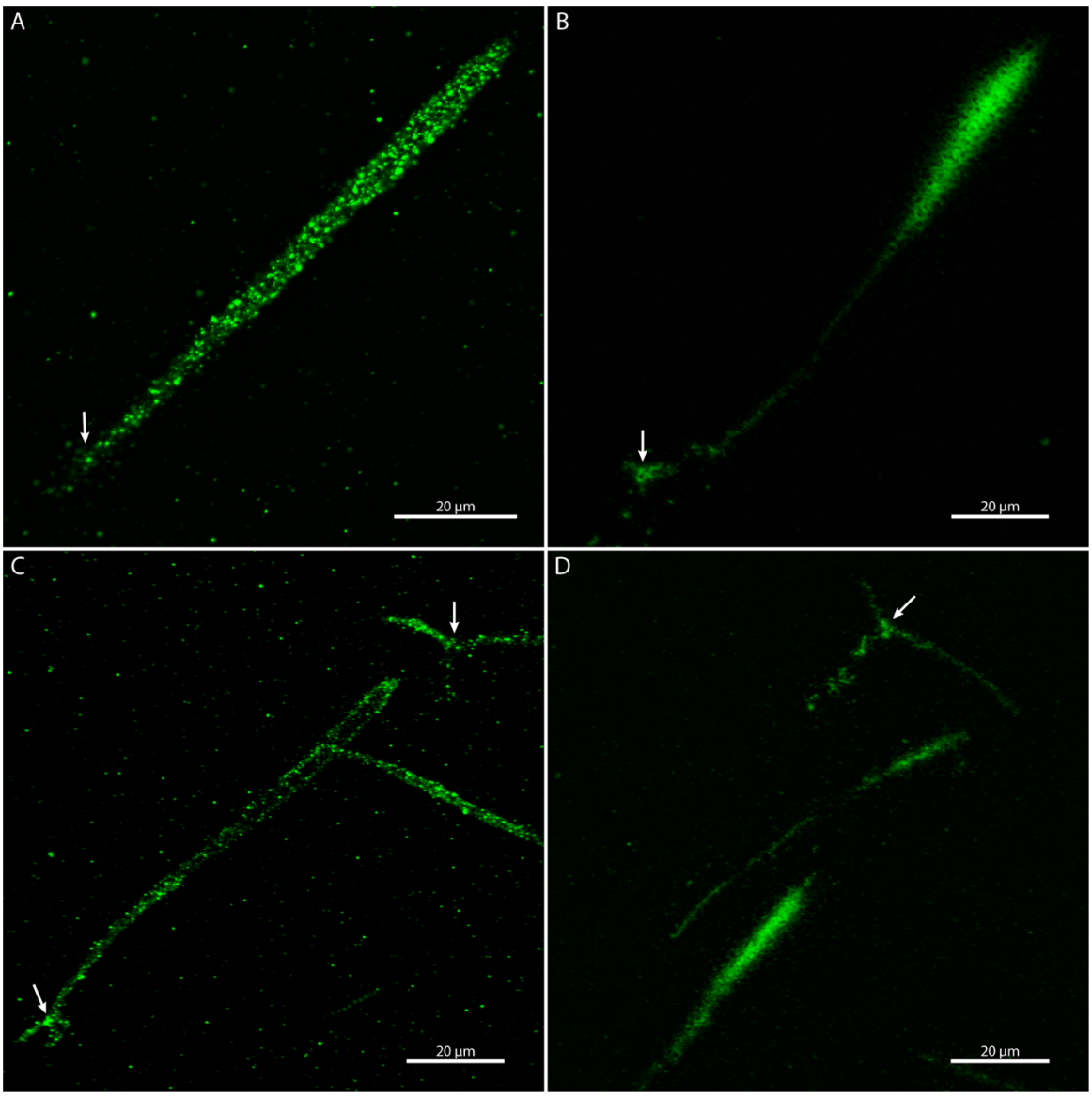

Figure 5.2. Immobilized spicule matrices stained with (A,C) SM30/BC or (B,D) SM50. Two representative frames shown for each protein stain. Region corresponding to triradiate rudiment portion of the spicule indicated (arrows). (A) single frames and (B-D) z-stacks with summed intensity values at each pixel.

The total absence of fluorescence in the control spicule blot samples rules out the possibility of background staining due to significant non-specific binding of the secondary antibody to the blotting paper or to immobilized spicule matrix proteins (Figure 5.1). This, combined with clear outlining of the pluteus spicule geometry in spicule blot samples stained for spicule matrix proteins, gives strong evidence that the spicule blot experiments succeeded in

labeling the organic matrix proteins. The observed static distribution of SM30B/C and heterogenous distribution of SM50 in the body rod of the spicule matched results reported by Kitajima and Urakami (Figure 5.2).[107] They interpreted these data as evidence that SM30 induces *c*-axis growth (because SM30 staining is continuous within the body rod, which elongates parallel to the *c*-axis of calcite) and that SM50 induces *a*-axis growth (because SM50 staining within the body rod is more intense in the thick regions near the tip, and thickening requires that the body rod must grow radially in the direction perpendicular to the *c*-axis). This hypothesis was supported by their findings that SM50 and not SM30 staining is visible in the triradiate portion of the spicule, since the triradiate rudiment forms by elongation along the three *a*-axes of calcite. We, however, did not see a complete absence of fluorescence in that region for spicules stained for SM30B/C, although SM50 staining in the triradiate area was stronger (Figure 5.2). Disparities between ours results and theirs could be due to sample preparation and imaging differences: we reacted primary antibodies specific for spicule matrix proteins with fluorescently conjugated secondary antibodies and observed samples under high resolution confocal microscopy, whereas Kitajima and Urakami reacted primary antibodies with a biotinylated secondary antibody that was then stained with chloronaphthol and imaged under optical microscopy. Our imaging method affords higher resolution and can likely detect lower protein densities. Another possibility is that *H. pulcherrimus* and *S. purpuratus* spicules have slightly different spicule matrix protein distributions, perhaps as a result of more thickening of the triradiate rudiment in *S. purpuratus* (which would require radial growth perpendicular to the *a*-axes that the triradiate elongates parallel to).

Under confocal fluorescence microscopy, we were also able to observe the morphology of the spicule's embedded organic matrix (Figure 5.3). High-resolution imaging of spicule blot samples stained for SM30B/C or SM50 revealed connected grainy spherical structures comprising proteinaceous material (Figure 5.3B,D). This appearance makes sense, given previous SEM characterization of partially demineralized spicules describing the spicule matrix as a web of fibrillar material running through the concentric rings of mineral.[47, 147] In our samples, individual clear masses of fluorescently labeled protein were distinguished, but the texture was different for SM30B/C and SM50. In the SM30B/C-stained spicule blot samples, fluorescently labeled protein appeared as spheres approximately 500 nm in diameter gathering into clusters slightly resembling bunches of grapes; large voids without antibody labeling were also observed (Figure 5.3B). Fluorescently labeled protein in SM50-stained spicule blot samples had a finer texture that assumed the morphology of an amorphous meshwork with unlabeled void areas approximately 400-900 nm in diameter (Figure 5.3D). Given that the voids in the SM30B/C labeled spicule blot samples were large and interconnected, and that the voids in the SM50 labeled spicule blot samples were of similar size to the fluorescently labeled spheres in the SM30B/C labeled samples, it seems probable that the empty regions in samples stained for one protein were the regions occupied by the other protein. This suggests that they gather into mutually exclusive areas even within a small (~9 μm × 9 μm) region of the spicule, but this cannot be stated definitively without simultaneous staining for both proteins followed by imaging and colocalization analysis. In addition, we question whether the patterns we observe exactly mirror those of the native proteins within the spicule, since dissolution from the mineral

and immobilization on the matrix could cause precipitation of protein into non-native morphologies.

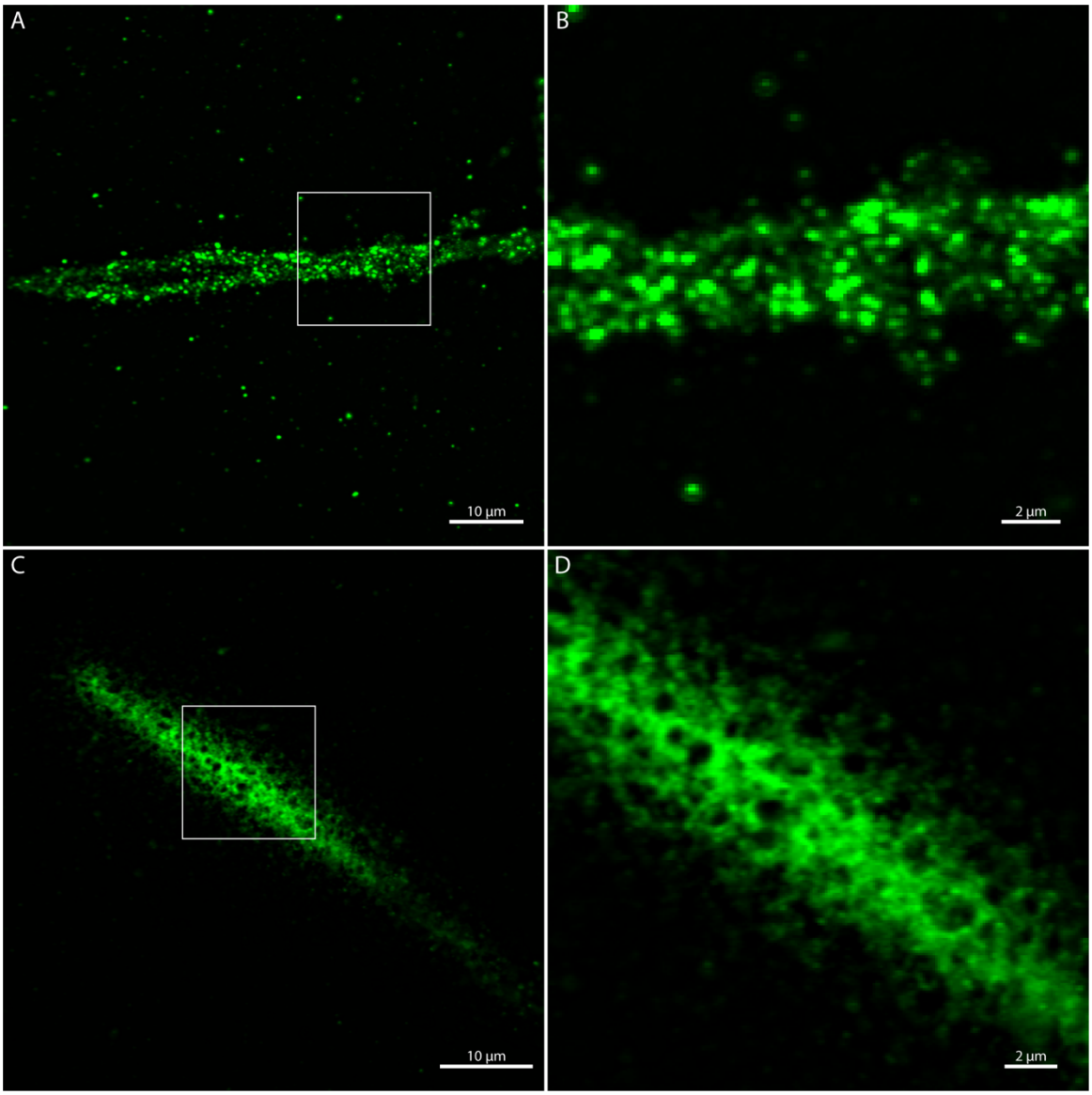

Figure 5.3. Texture of the spicule protein matrix. Spicule blots stained for (A-B) SM30B/C and (C-D) SM50. Regions within white squares (A,C) are zoomed in on (B,D). Images are single frames.

To broaden our analysis, we next sought to determine if spicule matrix proteins occluded within spicules collected from *in vitro* cultured PMCs had similar spatial distribution patterns to those of pluteus embryo spicules. We thus applied the successful spicule blot system on spicules

isolated from PMCs grown under different conditions with corresponding different shapes. As described in Chapter 3. we cultured PMCs in 4% (v/v) HS to generate linear spicules and in 4% (v/v) HS supplemented with 1.2 $\mu g \cdot mL^{-1}$ rVEGF to generate triradiate spicules. We isolated these spicules, used the spicule blot apparatus to dissolve and immobilize their protein matrices, and fluorescently immunolabeled for SM30B/C or SM50, which successfully revealed the shape of both spicule types (Figure 5.4). Staining was more diffuse than that of the pluteus embryo spicules, which may suggest that the protein matrix of spicules formed by PMC cultures is more dispersed and less dense than that of embryo spicules. The case could also be that the spicule blot sample preparation method is less robust for *in vitro* grown spicules, perhaps due to more contamination from organic material in the cell cultures, resulting in higher background signal, or, that the *in vitro* grown spicules are thinner and thus simply have less mineral resulting in less protein; the latter hypothesis could be tested by electron microscopy of isolated spicules from *in vitro* PMC cultures and embryos to compare diameters. Linear spicule blot samples stained with SM30B/C showed homogeneous fluorescence intensity across the rod (Figure 5.4A), whereas linear spicule blot samples stained with SM50 had much higher intensity at the tip of the spicule (Figure 5.4B). These data were in accord with that of embryo spicule specimens that had had consistent fluorescence intensity across the body rod for SM30B/C and a gradient of increasing fluorescence intensity towards the tip of the body rod for SM50. Triradiate spicule blot samples stained with SM30B/C had very diffuse intensity that lightly described the spicule (Figure 5.4C), whereas those stained with SM50 had denser and more intense staining (Figure 5.4D). This agreed with embryo samples for which SM50 staining of the triradiate section of the spicule was more common and much more intense than SM30B/C staining.

Interestingly, Kitajima and Urakami[107] observed very little SM50 and no SM30B/C staining in *in vitro* cultured spicules and Urrey *et al.* observed only light staining for both,[86] although these samples were fixed or fixed and lightly etched, so the overwhelming majority of occluded proteins was probably not observable. Our data herein thus provides entirely new insights into the protein matrix spatial distribution of *in vitro* grown spicules. We found that among spicule blot samples fluorescently immunolabeled for SM30B/C or SM50, intensity patterns were the same for spicules isolated from PMC cultures and embryos, that is, SM50 staining was more intense in *in vitro* grown triradiates, triradiate rudiment regions of pluteus spicules, and the tips of pluteus spicule body rods, whereas SM30B/C staining was homogeneous through *in vitro* grown linear spicules and pluteus spicule body rods, and absent or dim in *in vitro* grown triradiates and the triradiate rudiment regions of pluteus spicules. Altogether, these results suggest that deposition patterns of the spicule matrix proteins are the same *in vitro* and *in vivo*. This strengthens the hypothesis that *a*-axis growth (viz., triradiate elongation and body rod radial thickening) is accompanied by secretion of SM50, and *c*-axis growth (viz., body rod elongation and triradiate arm radial thickening) is accompanied by SM30B/C secretion.

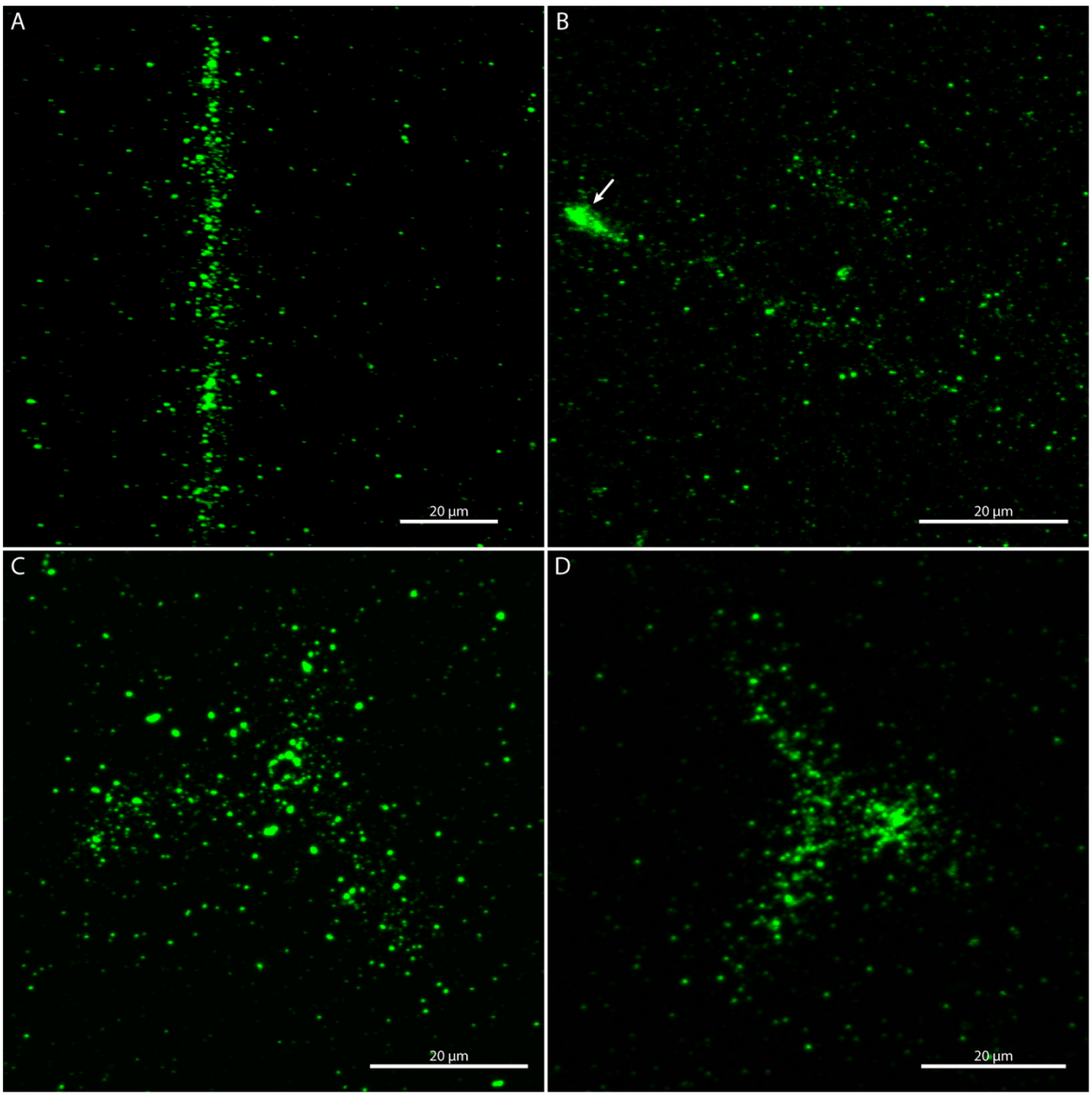

Figure 5.4. Spicules taken from PMC cultures incubated in (A-B) 4% (v/v) HS or (C-D) 4% (v/v) HS supplemented with 1.2 µg·mL^{-1} rVEGF, and stained for (A,C) SM30B/C or (C,D) SM50. Bright tip of a linear spicule indicated (B, arrow). Images are z-stacks with summed intensity values at each pixel.

5.3. Conclusion

We have successfully leveraged the spicule blot technique on spicules isolated from *S. purpuratus* embryos and PMC cultures. We immunolabeled spicule blot samples for the abundant spicule matrix proteins SM30B/C and SM50 and visualized protein distribution using a fluorescently conjugated secondary antibody and high-resolution confocal microscopy. We

found that, in pluteus embryo spicules, SM30B/C was homogeneously distributed in the body rod, whereas SM50 was localized in the triradiate rudiment section of the spicule and at the tip of the body rod. These results agreed with prior research finding similar spatial distributions for SM30 and SM50 in both *S. purpuratus* and other sea urchin species.[86, 107] For *in vitro* grown spicules, we found that SM50 staining was intense at the tip of linear spicules and in triradiate spicules, whereas SM30B/C staining was consistent throughout linear spicules and dim and disperse in triradiate spicules. These data agree with that of the pluteus embryo spicules.

Since protein distributions were similar in *in vitro* and *in vivo* grown spicules (i.e., SM50 localized at the thick tips of linear rods and in triradiates, and SM30B/C was homogeneously distributed throughout linear rods), we agree with the hypothesis that SM50 selects for *a*-axis growth and SM30B/C selects for *c*-axis growth. Our results herein strengthen this hypothesis, and because we observed the same phenomena in spicules isolated from PMC cultures and embryos, we postulate that these are selection rules universal to sea urchin spiculogenesis, probably even across species (although this needs to be experimentally verified beyond *S. purpuratus* and *H. pulcherrimus*).

Other experimental techniques, such as *in vitro* $CaCO_3$ growth assays probing spicule matrix protein function, as well as *in vivo* knockdown experiments, will be able to further test and validate the hypothesis that SM50 induces *a*-axis growth and SM30B/C induces *c*-axis growth. Furthermore, the robustness of our data demonstrates that the spicule blot system is an effective tool for studying the spatial distribution of biomineralization proteins. We believe this technique can be further leveraged to study the distribution of other spicule matrix proteins across sea urchin species, and even used to map proteins in biominerals formed by other

organisms, or macromolecules occluded within synthetically grown crystals (although proof of concept in the latter two cases will be necessary). We look forward to our methods refined herein enabling valuable insights into the mechanisms of protein-mediated crystal growth.

5.4. Materials and Methods

5.4.1. Disposables and equipment

Chemicals and consumables:

Unless otherwise noted, all reagents were stored at room temperature (22 °C). Ethanol (200 proof, Decon Laboratories Inc., King of Prussia, PA); concentrated bleach (8.25% NaClO, The Clorox Company, Oakland, CA); Na_2CO_3 (anhydrous, ≥99.5%), sucrose (≥99.5%) (Sigma-Aldrich, St. Louis, MO); rabbit anti-SM50 affinity purified antibody (1 $mg \cdot mL^{-1}$ in 0.09% NaN_3, stored at 4 °), rabbit anti-SM30BC affinity purified antibody (1 $mg \cdot mL^{-1}$ in 0.09% NaN_3, stored at 4 °) (Bethyl Laboratories, Montgomery, TX); EDTA disodium salt dihydrate (≥99%), PBS buffer (phosphate buffered saline, 1×, pH = 7.4, stored at 4 °C), TAE buffer (tris-acetate-EDTA, 100×, stored at 4 °C), Tween®-20 (20%), goat anti-rabbit IgG (H + L) highly cross-adsorbed secondary antibody Alexa Fluor® 488 conjugate (goat anti-rabbit-CF®488, 2 $mg \cdot mL^{-1}$ in 5 mM NaN_3, stored in the dark at 4 °C) (Thermo Fisher Scientific, Waltham, MA); 80% glycerol (sterile, stored at 4 °C) (Avantor, Radnor, PA).

Sterile Falcon tubes (15-mL, 50-mL), plastic Petri dishes (29 mm), poly(vinylidene difluoride) transfer membranes (PVDF, 0.45-μm) (Thermo Fisher Scientific, Waltham, MA); micro cover glass slips (18 mm × 18 mm, 0.14-0.17 mm thickness) (VWR, Radnor, PA); sterile polystyrene serological pipettes (10-mL, 20-mL) (TPP, Trasadingen, Switzerland); sterile low-

binding pipette tips (100-1000-µL) (Midwest Scientific, Valley Park, MO); Eppendorf® tubes (1.7-, 2-mL) (Eppendorf, Hamburg, Germany).

Equipment:

Beakers (250-, 500-mL,), graduated cylinders (100-, 500-mL), RS-5883 surgical grade scissors (Thermo Fisher Scientific, Waltham, MA); Dumoxel® tweezers (120 mm length) (Electron Microscopy Sciences, Hatfield, PA); centrifuge 5424, centrifuge 5810R (with temperature control, swing-bucket rotor with four 500-mL buckets, conical 50- and 200-mL inserts), single-channel adjustable volume pipettes (2-20-, 20-200-, 100-1000-µL) (Eppendorf, Hamburg, Germany); Portable Pipet-Aid® XP2 Pipette Controller (Drummond Scientific, Broomall, PA); Minifold® I microsample filtration system (dot-blot system acrylic) (Schleicher & Schuell, Keene, NH); Corning® stirrer/hotplate (model PC-320), vacuum aspirator with trap (Sigma-Aldrich, St. Louis, MO).

Solutions:

A solution of 85% (w/v) sucrose was prepared by dissolving 425 g sucrose in 500 mL UPW by gently stirring and heating (50 °C, 20 min). A stock solution of 300 mM Na_2CO_3 was prepared by dissolving 3.18 g Na_2CO_3 in 100 mL UPW. This was diluted 1:10 and 1:39 in UPW to make 30 mM and 7.7 mM solutions of Na_2CO_3. 25% (v/v), 50% (v/v), and 75% (v/v) ethanol solutions were prepared in UPW.

A solution of 1× TAE buffer was prepared by adding 1 mL of 100× TAE buffer to 99 mL UPW. Blotting buffer was prepared by dissolving 0.17 g of EDTA disodium dihydrate in 50 mL PBS. 0.8% (w/v) agarose solution was prepared immediately prior to use in spicule blot

experiments by suspending 0.8 g agarose in 100 mL 1× TAE buffer and dissolving the solid agarose by gently stirring and heating (50 °C, 5 min).

The blocking solution of 3% (w/v) BSA was prepared by dissolving 0.3 g BSA in 10 mL PBS. A solution of 0.02% Tween-20 was prepared in PBS by adding 10 µL of 20% Tween-20 to 10 mL PBS.

5.4.2. Spicule isolation from embryos

Sea urchins were purchased from Marinus Scientific (Long Beach, CA) and South Coast Bio-Marine LLC (San Pedro, CA) and maintained in Instant Ocean® seawater at 15 °C. Embryos were fertilized and cultured to the desired stage of development in a climate-controlled room at 15 °C as described in section 2.1.5. Embryos were collected by centrifugation (450 × *g*, 5 min) and supernatant was discarded. Embryos were resuspended in 50 mL ice cold (~4 °C) UPW for 10 min and collected by centrifugation (450 × *g*, 5 min). Supernatant was discarded and embryos were resuspended in 50 mL 8.25% (v/v) bleach. Embryos were incubated in this solution for 20 min and collected by centrifugation (2,000 × *g*, 10 min). Supernatant was removed and the white pellet of organic material and spicules was dispersed in 1 mL 8.25% (v/v) bleach and incubated for 10 min.

0.5 mL of 85% (w/v) sucrose were pipetted into a 1.7-mL Eppendorf tube and the suspension of organic material and spicules in bleach was gently layered on top of this solution by pipetting down the side of the Eppendorf tube. The Eppendorf tube was centrifuged (9,500 × *g*, 5 min) and the band of organic material at the boundary between sucrose and bleach, as well as the rest of the supernatant, were removed with a pipette. The spicule pellet at the bottom of the

Eppendorf tube dispersed in 8.25% (v/v) bleach and centrifugation through sucrose was repeated once.

The band of organic material and supernatant were again removed and, as described in section 3.4.5. Spicules were washed in series, with 8.25% (v/v) bleach, 30 mM Na_2CO_3, and 7.7 mM Na_2CO_3. Spicules were then dehydrated by washing, in series, with 25% (v/v), 50% (v/v) 75% (v/v), and 100% ethanol, the last wash repeated once. Spicules were stored for several days to weeks at -20 °C until needed for spicule blot experiments (note that spicules suspended in ethanol are stable for months at -20 °C).

5.4.3. Spicule isolation from PMC cultures

All experiments involving PMC culture were performed in a climate-controlled room at 15 °C. Glass bottom plates used in PMC culture were acid washed as described in section 2.2.3. Micromeres were isolated and seeded at a density of ~100,000 cells per glass bottom plate as described in section 2.1.5.

ASW used in PMC culture was supplemented with 100 $\mu g \cdot mL^{-1}$ gentamicin sulfate and 100 $U \cdot mL^{-1}$ penicillin + 100 $\mu g \cdot mL^{-1}$ streptomycin (ASWGPS). To induce linear or triradiate spicule formation, PMCs were incubated from 26 hpf to 56 hpf in ASWGPS supplemented with 4% (v/v) HS or 4% (v/v) HS and 1.2 $\mu g \cdot mL^{-1}$ rVEGF as described in section 3.4.3.

At 56 hpf, media were removed from the plates via aspiration and 2 mL of 8.25% (v/v) bleach were added to each plate. Spicules were dislodged using gentle trituration with a pipette. Bleach containing spicules and organic material was transferred to 2-mL Eppendorf tubes, which were then centrifuged (9,500 × *g*, 5 min). Supernatant was removed, and pellets of spicules and organic material were dispersed and collected in 2 mL of 8.25% (v/v) bleach. This suspension

was incubated for 20 min at room temperature with gentle agitation and was then centrifuged (9,500 × *g*, 5 min).

As described in section 3.4.5. spicules were washed, in series, with 8.25% (v/v) bleach, 30 mM Na_2CO_3, and 7.7 mM Na_2CO_3, and were then dehydrated by washing, in series, with 25% (v/v), 50% (v/v) 75% (v/v), and 100% ethanol, the last wash repeated once. Spicules were stored for several days to weeks at -20 °C until needed for spicule blot experiments.

5.4.4. Spicule blot and antibody staining

The blotting apparatus was unclamped, and plastic wrap was placed under the blotting wells. Each well of the blot apparatus was filled ~3/4 with freshly prepared and still liquid agarose solution and the apparatus was chilled at 4 °C to hasten agarose gelling. The blotting apparatus was returned to room temperature, unclamped, and excess agarose was washed off. A PVDF membrane was soaked in blotting buffer and placed over the region of blotting wells.

An Eppendorf tube containing spicules in ethanol was removed from -20 °C and warmed to room temperature. The Eppendorf tube was inverted several times to disperse the spicule pellet, and 100 µL of this dense suspension were transferred to another 1.7-mL Eppendorf tube and centrifuged (9,500 × *g*, 5 min). Supernatant was removed with a pipette and the spicules were resuspended in 1 mL PBS. The diluted spicule suspension was pipetted onto the soaked PVDF membrane, and the agarose wells were overlain on top of the spicules. The blotting apparatus was clamped, and ~3 mL of blotting buffer were pipetted over the agarose wells. The blotting apparatus was attached to a vacuum and blotting buffer was aspirated for 30 min. Afterwards, the vacuum was turned off, the blotting apparatus was unclamped, and the PVDF membrane was removed from the apparatus.

The PVDF membrane was cut with scissors into small (~1.5 cm × 1.5 cm) squares. PVDF squares were placed into plastic Petri dishes, immersed in 1 mL of 3% (w/v) BSA in PBS, and incubated for 1 h at room temperature with gentle agitation. The primary antibody (rabbit anti-SM50 or rabbit anti-SM30BC) was diluted 1:50 in 1 mL of 3% (w/v) BSA in PBS and PVDF squares were transferred to a plastic Petri dish containing this solution and incubated overnight at room temperature. Simultaneously, a control sample of spicule blot PVDF squares was incubated overnight at room temperature in only 3% (w/v) BSA in PBS.

The next day, all PVDF squares were transferred to fresh Petri dishes and washed with 0.02% Tween-20 in PBS (×2, 1 mL) and PBS (×3, 1 mL). The secondary antibody (goat anti-rabbit-CF®488) was diluted 1:200 in 2 mL of 3% (w/v) BSA in PBS and PVDF squares (including the control squares) were transferred to Petri dishes containing this solution and incubated overnight at room temperature. PVDF squares were again washed with 0.02% Tween-20 in PBS (×2, 1 mL) and PBS (×3, 1 mL). PVDF squares were transferred to fresh Petri dishes and immersed in 1 mL of 80% glycerol to make them translucent for optical microscopy. Samples were stored at 4 °C in the dark for 12-72 h before imaging.

5.4.5. Imaging of spicule blot samples

Spicule blot samples were removed from 4 °C and allowed to reach room temperature. Using tweezers, the PVDF squares were removed from solution and sandwiched between two micro cover glass slides. High resolution imaging was performed on a Leica TCS SP8 laser scanning confocal microscope using a 63× oil immersion objective lens. Goat anti-rabbit-CF®488 fluorescence was obtained with an excitation wavelength of 488 nm and capture of 500-570 nm bandwidth. Images were adjusted for brightness and contrast using ImageJ (NIH,

Bethesda, MD). Images in figures are single frames or z-stacks with summed intensity values at each pixel.

Chapter 6. Analysis of the Microstructure of *Crepidula fornicata* Shells

6.1. Introduction

In any discussion of biomineralizing phyla, it is quite painful to leave out Mollusca. Mollusks are interesting to compare to echinoderms: both masterfully produce an array of mineralized structures, but whereas most echinoderms specialize in molding calcium carbonate (and nearly without exception, as amorphous calcium carbonate (ACC) or calcite with varying degrees of magnesium substitution) into diverse body parts, mollusks make use of over 21 different minerals, including but not limited to calcite, aragonite, vaterite, magnetite, ferrihydrite, amorphous phosphates, and in one known case, hydroxyapatite![2] Owing to this massive diversity, it is more challenging to search for common structural themes or mechanisms of biomineral formation among mollusks than echinoderms. However, daunting the task may be, meticulously examining the biomineral of any one mollusk species from the perspectives of both materials science (analysis of microstructures; "form fits function") and biology (analysis of occluded macromolecules; finding a biomineralizing molecular toolkit) is a useful experimental framework to begin with.

The most prominent mineralized structures produced by mollusks are their shells that function doubly as housing and protection.[161] In the shell-forming mollusks (monoplacophorans, bivalves, scaphopods, cephalopods, and gastropods), mineralization occurs inside the mantle organ, which comprises two layers of epithelia.[162, 163] Analogous to the PMCs of the sea urchin embryo, specialized epithelial cells that line the dorsal mantle tissue are the main undertakers of shell biomineral formation.[164] These cells synthesize and secrete an array of macromolecules into an enclosed space delimited from the external environment by the proteinaceous and

unmineralized outer layer known as the periostracum.[165, 166] Within this enclosed space, the secreted macromolecules organize into an extracellular matrix that acts as a scaffold where mineral precipitation occurs.[167-169] The characteristic layers of shell build up over time, each layer typically comprising calcite or aragonite embedded within organic matrix.[170]

Mollusks form a dazzling array of over 50 shell microstructure types and subtypes, such as nacre and crossed-lamellar, which are identified by ultrastructural motifs.[171-173] Mechanical engineers and materials scientists have used high-resolution characterization techniques like electron microscopy to describe these complex hierarchical structures and have demonstrated that their spatial organization gives rise to a host of unique mechanical properties.[174] However, these analyses do not shed much light on the nuanced biochemical pathways through which mollusk shells form, making it difficult to reverse-engineer similar materials or find bio-inspired approaches for materials synthesis. Here is where the molecular biologists come in: over the past ten years, they have spent significant energy characterizing molluscan extracellular organic matrix proteins (henceforth, shell matrix proteins, SMPs) through powerful twenty-first century techniques in biotechnology such as proteomics and transcriptomics.[175, 176] These approaches have generated comprehensive lists of shell matrix proteins, but the next challenge is to interrogate shell matrix protein function. Functional studies can be accomplished by examining the biomineralization genetic regulatory program (viz., to understand how shell matrix proteins are transcriptionally regulated during development) through gene knockdown experiments,[177] as well as testing the role of these proteins through *in vitro* crystal growth experiments.[178, 179]

The overarching goal of this collaborative work between groups at Northwestern University and The University of California, San Diego was to combine materials

characterization with molecular biology approaches to both understand the shell microstructure of the gastropod species *Crepidula fornicata* and the gene regulatory network (GRN) controlling its formation, knowledge that, when combined, will unlock a full picture of mollusk shell biomineralization. The work included in this thesis focuses on the materials side of the project, but interested readers are encouraged to delve into the full paper in Integrative Organismal Biology for a discussion of the extremely complex GRN that was described for the first time.

6.2. Results and Discussion

6.2.1. XRD characterization of shell powders

The most frequently encountered shell microstructure in gastropods is the crossed lamellar structure.[171, 180] Similar to nacre, but much less studied, it comprises aragonite ($CaCO_3$) and a small fraction of organic matter.[181-183] Since nacre and crossed-lamellar comprise different polymorphs of $CaCO_3$, techniques that can distinguish between crystalline phases, such as X-ray diffraction (XRD), will quickly eliminate one of the microstructures. Powder XRD (PXRD) patterns obtained from *C. fornicata* shells matched those of a geological reference material, confirming that the calcium carbonate polymorph present is aragonite,[184] thus ruling out nacre as a possible microstructure. This finding confirms recent observations[185] and shows no indication for the presence of other crystalline minerals (Figure 6.1). It must be mentioned, however, that PXRD cannot rule out the presence of amorphous phases such as ACC.

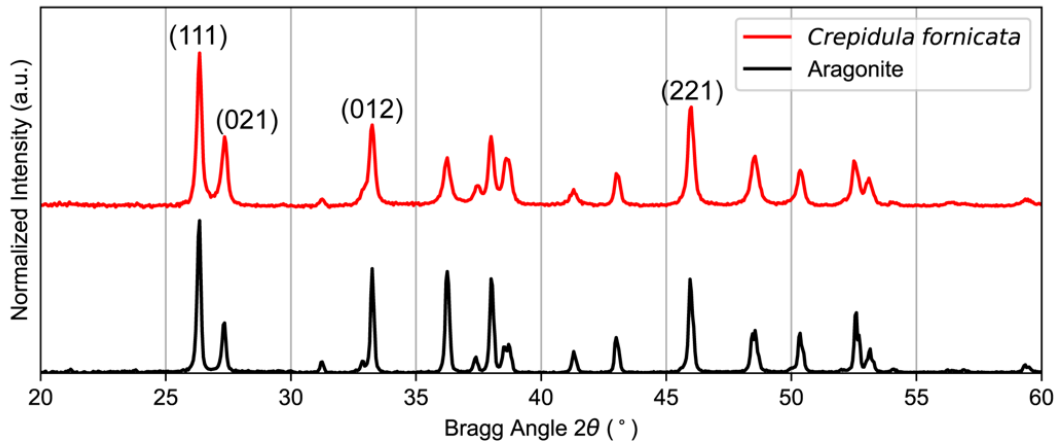

Figure 6.1. Powder X-ray diffraction (PXRD) patterns of *C. fornicata shell* and geological aragonite reference standard. Plot of diffracted intensity, normalized to that of the (111) reflection, against the Bragg angle.

6.2.2. Light and electron microscopy of shells

Inspection of fracture surfaces and sections of *C. fornicata* shells revealed a hierarchical organization at lengths from the micro- to the nanoscale that is typical for the crossed-lamellar structure (Figure 6.2). Under crossed-polarized illumination, alternating bands of light and dark contrast revealed outer, middle, and inner macrolayers that can be distinguished at the length scale of hundreds of µm and run approximately parallel to the external surface. Under scanning electron microscopy (SEM), fracture surfaces revealed macrolayers to comprise first-order (1˚) lamellae that appear as alternating light and dark bands approximately 5-25 µm in thickness. Interestingly, near the outer shell surface they run normal to the macrolayers (Figure 6.2C-E). Each 1˚ lamella comprises second order (2˚) lamellae that give rise to the characteristic stepped fracture surface. In ground, polished, and lightly etched sections, borders between 1˚ and 2˚ lamellae can be distinguished (Figure 6.2F), revealing a long axis that runs in the plane of the 1˚ lamella, and two shorter axes, one of which is normal to the plane. The long axes of 2˚ lamella in successive 1˚ lamellae are rotated against each other by and angle between 80-100˚. This is

particularly apparent where 2˚ lamellae emerge at the fracture surface under different angles in alternating 1˚ layers (Figure 6.2D-E). Finally, each 2˚ lamella comprises of a stack of third-order (3˚) lamellae that are elongated parallel to the long axis of the 2˚ lamellae and show a characteristic pattern of thin laths 100-250 nm in thickness (Figure 6.2G-H). Etching partially dissolves the 3˚ lamellae into thin aragonite needles and makes their orientation more apparent, such as the ~90° misorientation between 3˚ lamellae in neighboring 1˚ lamellae (Figure 6.2H). In other gastropods, 3˚ lamellae display a high amount of crystallographic twinning that could be considered a 4th order lamellar structure.[186] It is expected that this is true for *C. fornicata* as well, although it is not yet confirmed so.

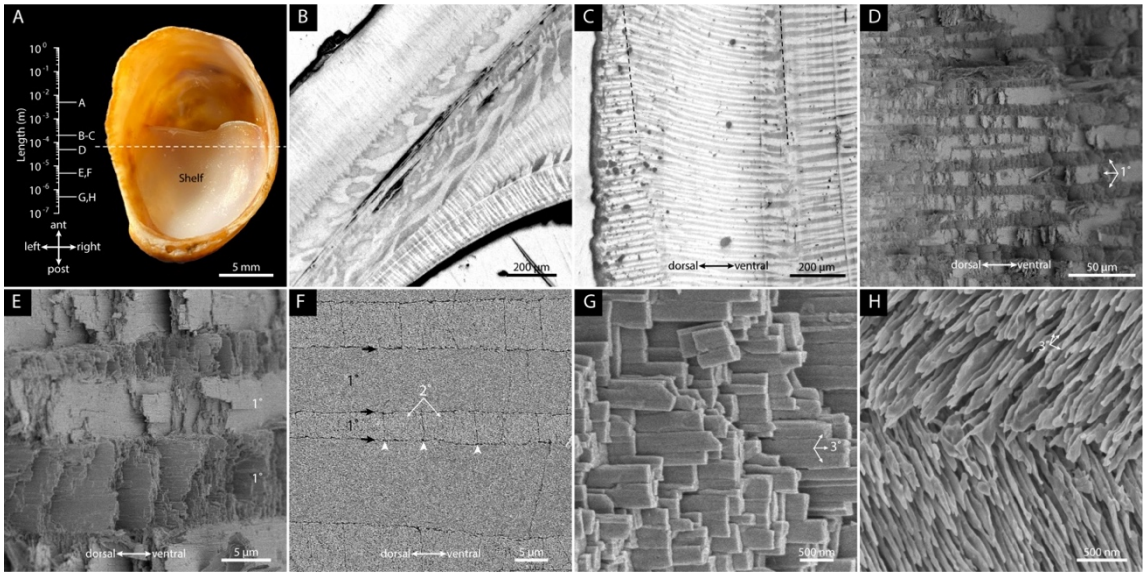

Figure 6.2. Length scales of the crossed-lamellar microstructure of the shell of *C. fornicata*. (A) Ventral view of the adult shell. (B-C) Reflected, polarized light microscopy images of sections approximately normal to the anterior-posterior axis. A number of macro layers with different orientations of 1˚ lamellae are visible where the shelf is joined to the shell (B); on the arc between these junctions three macro layers can be recognized by the slightly different orientation of the banding pattern (dashed lines, C). (D) SEM image of a fracture surface, approximately normal to the anterior-posterior axis. White arrows indicate first order (1˚) lamellae. (E) Higher magnification image from the same area in B. (F) SEM image of a polished and etched surface on the plane normal to the posterior-anterior axis and looking down the posterior direction. Black arrows indicate boundaries between 1˚ lamellae and white arrowheads indicate boundaries between second order (2˚) lamellae. (G) SEM image of third order (3˚) lamellae (white arrows) in a fracture surface. (H) SEM image showing 3˚ lamellae (white arrows) in neighboring 1˚ lamellae in a polished and etched sample.

The highly hierarchical structure is thought to convey exceptional fracture toughness to the shell, which likely occurs by tortuous propagation of cracks along lamellae boundaries, thus preventing catastrophic fracture.[186, 187] The regular appearance of macro- and microlayers in which smaller elements are rotated against each other and stacked in a regular fashion strongly suggests that the deposition is under tight biological control. For instance, the mantle tissue likely controls the orientation of the plane of the 1˚ lamellae that in the outer and inner macrolayers are normal to the shell surface, but oriented at some oblique angle in middle layers (Figure 6.2B). Similarly, the alternating orientation of the 2˚ lamellae in subsequent 1˚ lamellae is unlikely to occur by chance. It is therefore highly likely that spatiotemporal control over mineral deposition depends on a dedicated GRN in the mantle.

6.3. Conclusion

We herein used materials characterization to generate robust evidence that the shell of *C. fornicata* comprises the crossed-lamellar microstructure. PXRD proved unequivocally that the shell is composed of the aragonite phase of calcium carbonate. SEM of fracture surfaces revealed the characteristic stepped architecture of crossed-lamellar microstructure. This was confirmed in light microscopy of ground and polished sections, which also revealed outer, middle, and inner macrolayers of the shell, another hallmark of crossed-lamellar microstructure. SEM of ground, polished, and lightly etched sections provided confirmation of the presence of hierarchically organized 1˚, 2˚, and 3˚ lamellae. This regular and nuanced microstructure is likely controlled by a complex biomineralizing GRN, such as the one shown to exist in *C. fornicata* by our collaborators at The University of California San Diego. This work not only elaborates the microstructure of a particular species of mollusk but provides the framework in which materials

and biological approaches may be used to fully explain a pathway through which a complex shell architecture is formed.

6.4. Materials and Methods

6.4.1. Consumables and equipment

Chemicals and disposables:

All reagents were stored at room temperature (22 °C). EDTA disodium salt dihydrate (≥99%) (Thermo Fisher Scientific, Waltham, MA); Epofix resin (Electron Microscopy Sciences, Hatfield, PA); geological aragonite (Top Minerals, Czech Republic).

CarbiMet silicon carbide grinding paper (600, 800, 1200 grit size), MetaDi™ Supreme polycrystalline diamond suspensions (1-µm, 3-µm, aqueous) (Buehler, Wooster, OH); carbon conductive tape (12 mm width × 20 m length, double coated), SEM pin mount stubs (Ø12.7 mm × 8 mm height) (Ted Pella, Inc., Redding, CA).

Equipment:

Dumoxel® tweezers (120 mm length) (Electron Microscopy Sciences, Hatfield, PA); Isomet™ diamond blade (0.4 mm thickness, 127 mm diameter) (Buehler, Wooster, OH).

Solutions:

Solutions were prepared with ultrapure water (UPW, $\rho = 18.2\ M{\cdot}\Omega{\cdot}cm$) dispensed by a Barnstead NanoDiamond UF + UV purification unit and stored at room temperature.

A solution of 4.3% (w/v) EDTA disodium dihydrate was prepared by dissolving 21.5 g EDTA disodium salt dihydrate in 500 mL UPW.

6.4.2. Sample preparation for PXRD analysis

The shells of adult *C. fornicata* specimens and of approximately 1 g of geological aragonite were powdered using a mortar and pestle. Powders were analyzed on a Rigaku Ultima with a voltage of 40 kV and a tube current of 44 mA with a 5 mm slit to obtain PXRD data. Background subtraction was performed in CrystalDiffract (Version 6.9.3). Patterns were plotted using Matplotlib (Version 3.3.3) in Python.

6.4.3. Sample preparation for light and electron microscopy

Fracture surfaces were prepared by using a pair of tweezers to break adult *C. fornicata* shells approximately normal to the posterior-anterior axis. For ground and polished sections, adult *C. fornicata* shells were embedded in fresh Epofix resin (prepared according to the manufacturer's instructions) and cured at room temperature for 24 h. Shells were then sectioned in a plane normal to the posterior-anterior axis, using a Buehler low-speed Isomet™ rotary saw equipped with a diamond blade. The resulting sections were ground, in series, with 600, 800, and 1200 grit silicon carbide paper. Sections were then polished, in series, with 3-µm and 1-µm aqueous diamond suspensions and rinsed with deionized water. If etching was desired, samples were immersed in 4.3% (w/v) EDTA disodium dihydrate for 20 s at room temperature, rinsed with deionized water, and air dried.

Light microscope images of polished samples were taken on a Nikon Eclipse MA200 using brightfield and crossed-polarized illumination. For electron microscopy, shell fragments and polished and etched sections were mounted on aluminum SEM stubs using double-sided carbon tape and coated with 20 nm of Au/Pd using a Denton Desk IV sputter coater (Denton Vacuum). Samples were imaged using a Hitachi SU8030 SEM equipped with a field emission

source. Images were recorded at 2 keV acceleration voltage and a working distance of 8.0 mm, using secondary electron contrast.

Chapter 7. Future Work and Outlook

7.1. Synopsis

Herein, we have leveraged the PMC *in vitro* culture system to examine the formation of the sea urchin spicule, which is a model system for biogenic single crystal growth.

In Chapter 2, we refine the PMC *in vitro* culture system and expand it to characterization tools including confocal fluorescence microscopy, transmission electron microscopy, and transcriptomics analysis. We also optimize imaging and other experimental parameters to work extraordinarily well with the *in vitro* cultured PMCs and spicules, allowing consistent generation of robust data. This proof-of-concept work enables intimate dissection of a biomineralization process and forms the backbone of experimentation in the vast majority of this dissertation.

In Chapter 3, we found that the timing of VEGF signaling is another lever controlling spicule formation. Specifically, we demonstrated that continuous VEGF signaling is requisite for triradiate formation and that delayed VEGF signaling can induce spicule hyperbranching. Spicule morphology can be further controlled by varying the starting and ending VEGF concentrations, resulting in several types of hyperbranched spicules and thickened spicules. Furthermore, bichromatic calcein staining and fluorescence microscopy revealed that spicule branching occurs off of both existing body rod and off of nascent body rod.

In Chapter 4, we found that the cytoskeleton is critical for spicule formation. Using confocal fluorescence microscopy, we revealed a complex cytoskeleton comprising the molecules actin and tubulin that accompanies spiculogenesis. With inhibition via pharmacological inhibitors, we demonstrated that continuous function of both actin and tubulin from an early timepoint is necessary for spicule formation and growth. Using calcein staining,

we showed that inhibition of actin and tubulin halts calcium uptake into the spicule, and that inhibition of both molecules decreases the number of endocytosed vesicles. We used pharmacological inhibitors to perturb the function of two molecules associated with micropinocytosis via clathrin-mediated endocytosis, dynamin and clathrin, and found that neither was critical for spicule formation, indicating that micropinocytosis likely unimportant for spiculogenesis. Inhibition of dynein, a motor protein that transports vesicles along microtubules, also did not disturb spicule formation. Overall, our results point to cytoskeleton-dependent macropinocytosis as critical for spicule formation.

In Chapter 5, we successfully applied the spicule blot technique to *S. purpuratus* spicules isolated from embryos and PMC cultures and immunolabeled for spicule matrix proteins SM30B/C and SM50. We found that both are heterogeneously distributed throughout the spicule, confirming prior results from other groups with different species. We thus find evidence that the two proteins have different functions in spiculogenesis and that this function is universal across species and in *in vitro* cultured PMCs and the whole embryo.

In Chapter 6, we used X-ray diffraction and light and electron microscopy to analyze adult *C. fornicata* shells. We demonstrated that these shells comprise aragonite organized into the crossed-lamellar microstructure.

7.2. Future Directions

We envision myriad paths forward for these projects.

As the basis for most experimentation in this project, the *in vitro* PMC culture system outlined in Chapter 2 can be used with powerful characterization techniques such as TEM and

SEM to enhance the other experiments within this dissertation. Specific examples are discussed below.

The VEGF signaling system researched in Chapter 3 can be further explored via the spatial dimension: more specifically, patterning of VEGF on cell culture substrates via 2D printing and engineering of VEGF gradients via microfluidic devices could be used to test if the location of VEGF is another lever for control over spicule formation. We suspect that it is, as the embryo is known to tightly control the spatial distribution of growth factors within the epithelium.[57, 60] We also seek a mechanistic explanation for how the PMCs directly control spicule branching and crystallographic direction changing at the molecular level. To this end, ultrastructural studies looking into cellular features such as the cytoskeleton and the occluded spicule matrix proteins will likely be pursued. We thus expect that this project will significantly overlap with the cytoskeleton project and the spicule blot studies.

The cytoskeleton project of Chapter 4 can be rounded out by using more pharmacological inhibitors to probe the remaining endocytosis pathways. For example, we have eliminated clathrin-mediated endocytosis as a potential mechanism of spicule formation, but other processes such as caveolar-mediated endocytosis remain a possibility. More structural studies leveraging techniques such as immunolabeling and TEM could be used to examine microscopic features such as the actin hotspots observed under confocal fluorescence microscopy. In addition, confirmation of *in vitro* results in the whole embryo would eliminate ambiguity of data interpretation.

The spicule blot project of Chapter 5 should be leveraged with other spicule matrix proteins. As a next step, we will generate recombinant antibodies for proteins such as PM27 and

immunolabel spicule blot samples for these proteins, thus providing novel data on the spatial distribution of these proteins within the spicule. We also believe this technique can be adapted for electron microscopy through the use of gold nanoparticle conjugated secondary antibodies, although proof-of-concept here is necessary. It is also possible that the spicule blot method can be adapted for use with other biominerals such as the strontium sulfate skeletons of Acantharea, but again, proof-of-concept experimentation is requisite.

The *C. fornicata* collaboration project of Chapter 6 could benefit from more ultrastructural analysis, such as TEM imaging to look for fourth-order lamellae, or demineralization studies coupled with SEM to characterize the organic matrix of the shell. Mechanical testing could also be used to study the fracture mechanics of the shell and determine the basic mechanical properties. To study the shell microstructure within the context of its gene regulatory network, we also foresee characterization of shells formed by animals genetically manipulated to over or under express particular shell biomineralization proteins.

7.3. Concluding Remarks

Overall, we have expanded upon the model for formation of the sea urchin embryonic spicule. We demonstrated that the timing of VEGF signaling is a critical control lever for spicule formation. This strengthens our knowledge of how indirect control via growth factors directs PMC behavior to alter spicule morphology. We also showed that the cytoskeleton, especially the molecules actin and tubulin, are necessary for spicule formation and growth, and our results indicate that macropinocytosis a key driver for spiculogenesis. In addition, we confirmed that two major spicule matrix proteins are heterogeneously distributed within the spicule. We have thus elucidated specific mechanisms of spicule formation. The findings in this dissertation clarify

a complex process of biogenic single crystal growth and will benefit our understanding not only of sea urchin spiculogenesis, but biomineralization processes in general, which will inform anthropogenic mastery over materials synthesis.

References

1. Cloud, P., Earliest biogeologic history: The emergence of a paradigm. In *Earth's Earliest Biosphere*, Schopf, J. W., Ed. Princeton University Press: Princeton, 1983; pp 14-31.
2. Lowenstam, H. A.; Weiner, S., *On Biomineralization*. Oxford University Press: Oxford, 1989.
3. Mann, S., *Biomineralization: Principles and Concepts in Bioinorganic Materials Chemistry*. Oxford University Press: Oxford, 2001.
4. Drake, J. L.; Mass, T.; Stolarski, J.; Von Euw, S.; van de Schootbrugge, B.; Falkowski, P. G., How corals made rocks through the ages. *Global Change Biology* **2020,** *26* (1), 31-53.
5. Krumhardt, K. M.; Lovenduski, N. S.; Iglesias-Rodriguez, M. D.; Kleypas, J. A., Coccolithophore growth and calcification in a changing ocean. *Progress in oceanography* **2017,** *159*, 276-295.
6. Reynolds, C. S., Diatoms and the geochemical cycling of silicon. In *Biomineralization in lower plants and animals*, Leadbeater, B. S. C.; Riding, R., Eds. Oxford University Press: Oxford, 1986; Vol. 30, pp 269-289.
7. Jiang, W.; Pan, H.; Wang, F.; Jiang, M.; Deng, X.; Li, J., A rapid sample processing method to observe diatoms via scanning electron microscopy. *Journal of applied phycology* **2014,** *27* (1), 243-248.
8. Mishra, M.; Arukha, A. P.; Bashir, T.; Yadav, D.; Prasad, G. B. K. S., All New Faces of Diatoms: Potential Source of Nanomaterials and Beyond. *Frontiers in microbiology* **2017,** *8*, 1239-1239.
9. Addadi, L.; Joester, D.; Nudelman, F.; Weiner, S., Mollusk Shell Formation: A Source of New Concepts for Understanding Biomineralization Processes. *ChemInform* **2006,** *37* (16), no-no.
10. Berman, A.; Hanson, J.; Leiserowitz, L.; Koetzle, T. F.; Weiner, S.; Addadi, L., Biological Control of Crystal Texture: A Widespread Strategy for Adapting Crystal Properties to Function. *Science (American Association for the Advancement of Science)* **1993,** *259* (5096), 776-779.
11. Evans, J., Polymorphs, Proteins, and Nucleation Theory: A Critical Analysis. *Minerals (Basel)* **2017,** *7* (4), 62.
12. Raz, S.; Weiner, S.; Addadi, L., Formation of High-Magnesian Calcites via an Amorphous Precursor Phase: Possible Biological Implications. *Advanced materials (Weinheim)* **2000,** *12* (1), 38-42.
13. Pikey, O. H.; Goodell, H. G., Trace Elements in Recent Mollusk Shells. *Limnology and oceanography* **1963,** *8* (2), 137-148.
14. Lowenstam, H. A., Mineralogy, O18/O16Ratios, and Strontium and Magnesium Contents of Recent and Fossil Brachiopods and Their Bearing on the History of the Oceans. *The Journal of geology* **1961,** *69* (3), 241-260.
15. Aizenberg, J.; Tkachenko, A.; Weiner, S.; Addadi, L.; Hendler, G., Calcitic microlenses as part of the photoreceptor system in brittlestars. *Nature* **2001,** *412* (6849), 819-822.
16. Bandyopadhyay-Ghosh, S., Bone as a collagen-hydroxyapatite composite and its repair. *Trends in Biomaterials and Artificial Organs* **2008,** *22*.

17. Uebe, R.; Schüler, D., Magnetosome biogenesis in magnetotactic bacteria. *Nature reviews. Microbiology* **2016,** *14* (10), 621-637.
18. Sandhage, K. H.; Allan, S. M.; Dickerson, M. B.; Gaddis, C. S.; Shian, S.; Weatherspoon, M. R.; Cai, Y.; Ahmad, G.; Haluska, M. S.; Snyder, R. L.; Unocic, R. R.; Zalar, F. M.; Zhang, Y.; Rapp, R. A.; Hildebrand, M.; Palenik, B. P., Merging Biological Self-Assembly with Synthetic Chemical Tailoring: The Potential for 3-D Genetically Engineered Micro/Nano-Devices (3-D GEMS). *International journal of applied ceramic technology* **2005,** *2* (4), 317-326.
19. Sandhage, K. H.; Bao, Z.; Weatherspoon, M. R.; Shian, S.; Cai, Y.; Graham, P. D.; Allan, S. M.; Ahmad, G.; Dickerson, M. B.; Church, B. C.; Kang, Z.; Abernathy Iii, H. W.; Summers, C. J.; Liu, M., Chemical reduction of three-dimensional silica micro-assemblies into microporous silicon replicas. *Nature (London)* **2007,** *446* (7132), 172-175.
20. Poulsen, N.; Berne, C.; Spain, J.; Kröger, N., Silica Immobilization of an Enzyme through Genetic Engineering of the Diatom Thalassiosira pseudonana. *Angewandte Chemie (International ed.)* **2007,** *46* (11), 1843-1846.
21. Demers, C.; Hamdy, C. R.; Corsi, K.; Chellat, F.; Tabrizian, M.; Yahia, L. H., Natural coral exoskeleton as a bone graft substitute: a review. *Bio-medical materials and engineering* **2002,** *12* (1), 15-35.
22. Sethmann, I.; Luft, C.; Kleebe, H.-J., Development of Phosphatized Calcium Carbonate Biominerals as Bioactive Bone Graft Substitute Materials, Part I: Incorporation of Magnesium and Strontium Ions. *Journal of functional biomaterials* **2018,** *9* (4), 69.
23. Stegbauer, L.; Smeets, P. J. M.; Free, R.; Wallace, S. G.; Hersam, M. C.; Alp, E. E.; Joester, D., Persistent polyamorphism in the chiton tooth: From a new biomineral to inks for additive manufacturing. *Proceedings of the National Academy of Sciences - PNAS* **2021,** *118* (23), 1.
24. Garnier, M. J.; Dunand, D. C., Ni-Al2O3 nacre-like composites through hot-pressing of freeze-cast foams. *Materials science & engineering. A, Structural materials : properties, microstructure and processing* **2019,** *743*, 190-196.
25. Tester, C. C.; Brock, R. E.; Wu, C.-H.; Krejci, M. R.; Weigand, S.; Joester, D., In vitro synthesis and stabilization of amorphous calcium carbonate (ACC) nanoparticles within liposomes. *CrystEngComm* **2011,** *13* (12), 3975-3978.
26. Tester, C. C.; Whittaker, M. L.; Joester, D., Controlling nucleation in giant liposomes. *Chemical communications (Cambridge, England)* **2014,** *50* (42), 5619-5622.
27. Tester, C. C.; Wu, C.-H.; Weigand, S.; Joester, D., Precipitation of ACC in liposomes-a model for biomineralization in confined volumes. *Faraday discussions* **2012,** *159* (2012), 345-356.
28. Cavanaugh, J.; Whittaker, M. L.; Joester, D., Crystallization kinetics of amorphous calcium carbonate in confinement. *Chemical science (Cambridge)* **2019,** *1* (19), 539-543.
29. Aizenberg, J., Crystallization in Patterns: A Bio-Inspired Approach. *Advanced materials (Weinheim)* **2004,** *16* (15), 1295-1302.
30. Kayo, O.; Richard, M. D.; Karl, M. W., Crystalline Axes of the Spine and Test of the Sea Urchin Strongylocentrotus purpuratus: Determination by Crystal Etching and Decoration. *The Biological bulletin (Lancaster)* **1981,** *161* (3), 402-415.

31. Ma, Y.; Aichmayer, B.; Paris, O.; Fratzl, P.; Meibom, A.; Metzler, R. A.; Politi, Y.; Addadi, L.; Gilbert, P. U. P. A.; Weiner, S., The Grinding Tip of the Sea Urchin Tooth Exhibits Exquisite Control over Calcite Crystal Orientation and Mg Distribution. *Proceedings of the National Academy of Sciences - PNAS* **2009,** *106* (15), 6048-6053.
32. Masic, A.; Weaver, J. C., Large area sub-micron chemical imaging of magnesium in sea urchin teeth. *Journal of structural biology* **2015,** *189* (3), 269-275.
33. Dubois, P.; Ameye, L., Regeneration of spines and pedicellariae in echinoderms: A review. *Microscopy research and technique* **2001,** *55* (6), 427-437.
34. Wilt, F. H., Matrix and Mineral in the Sea Urchin Larval Skeleton. *Journal of structural biology* **1999,** *126* (3), 216-226.
35. Okazaki, K.; Inoué, S., Crystal property of the larval sea urchin spicule. *Development, growth & differentiation* **1976,** *18* (4), 413-434.
36. Emlet, R. B., Echinoderm Calcite: A Mechanical Analysis from Larval Spicules. *The Biological bulletin (Lancaster)* **1982,** *163* (2), 264-275.
37. Ettensohn, C. A., Lessons from a gene regulatory network: echinoderm skeletogenesis provides insights into evolution, plasticity and morphogenesis. *Development* **2009,** *136* (1), 11-21.
38. Lyons, D. C.; Kaltenbach, S. L.; McClay, D. R., Morphogenesis in sea urchin embryos: linking cellular events to gene regulatory network states. *Wiley Interdiscip Rev Dev Biol* **2012,** *1* (2), 231-52.
39. Hu, M. Y.; Petersen, I.; Chang, W. W.; Blurton, C.; Stumpp, M., Cellular bicarbonate accumulation and vesicular proton transport promote calcification in the sea urchin larva. *Proceedings of the Royal Society. B, Biological sciences* **2020,** *287* (1934), 20201506-20201506.
40. Hu, M. Y.; Yan, J.-J.; Petersen, I.; Himmerkus, N.; Bleich, M.; Stumpp, M., A SLC4 family bicarbonate transporter is critical for intracellular pH regulation and biomineralization in sea urchin embryos. *eLife* **2018,** *7*.
41. Weiner, S.; Addadi, L., Crystallization Pathways in Biomineralization. *Annual review of materials research* **2011,** *41* (1), 21-40.
42. Beniash, E.; Aizenberg, J.; Addadi, L.; Weiner, S., Amorphous calcium carbonate transforms into calcite during sea urchin larval spicule growth. *Proceedings of the Royal Society. B, Biological sciences* **1997,** *264* (1380), 461-465.
43. Vidavsky, N.; Addadi, S.; Mahamid, J.; Shimoni, E.; Ben-Ezra, D.; Shpigel, M.; Weiner, S.; Addadi, L., Initial stages of calcium uptake and mineral deposition in sea urchin embryos. *Proc Natl Acad Sci U S A* **2014,** *111* (1), 39-44.
44. Vidavsky, N.; Masic, A.; Schertel, A.; Weiner, S.; Addadi, L., Mineral-bearing vesicle transport in sea urchin embryos. *J Struct Biol* **2015,** *192* (3), 358-365.
45. De Yoreo, J.; Gilbert, P. U. P. A.; Sommerdijk, N. A. J. M.; Lee Penn, R.; Whitelam, S.; Joester, D.; Zhang, H.; Rimer, J. D.; Navrotsky, A.; Banfield, J. F.; Wallace, A. F.; Marc Michel, F.; Melum, F. C.; Cölfen, H.; Dove, P. M., Crystallization by particle attachment in synthetic, biogenic, and geologic environments. *Science (American Association for the Advancement of Science)* **2015,** *349* (6247), 498-498.
46. Addadi, L.; Weiner, S., Biomineralization: mineral formation by organisms. *Physica scripta* **2014,** *89* (9), 98003.

47. Mann, K.; Wilt, F. H.; Poustka, A. J., Proteomic analysis of sea urchin (Strongylocentrotus purpuratus) spicule matrix. *Proteome Science* **2010,** *8* (1).
48. Raz, S.; Hamilton, P. C.; Wilt, F. H.; Weiner, S.; Addadi, L., The Transient Phase of Amorphous Calcium Carbonate in Sea Urchin Larval Spicules: The Involvement of Proteins and Magnesium Ions in Its Formation and Stabilization. *Advanced Functional Materials* **2003,** *13* (6), 480-486.
49. Jain, G.; Pendola, M.; Rao, A.; Cölfen, H.; Evans, J. S., A Model Sea Urchin Spicule Matrix Protein Self-Associates To Form Mineral-Modifying Protein Hydrogels. *Biochemistry* **2016,** *55* (31), 4410-4421.
50. Oliveri, P.; Tu, Q.; Davidson, E. H., Global regulatory logic for specification of an embryonic cell lineage. *Proc Natl Acad Sci U S A* **2008,** *105* (16), 5955-62.
51. Rafiq, K.; Cheers, M. S.; Ettensohn, C. A., The genomic regulatory control of skeletal morphogenesis in the sea urchin. *Development (Cambridge)* **2012,** *139* (3), 579-590.
52. Armstrong, N.; McClay, D. R., Skeletal Pattern Is Specified Autonomously by the Primary Mesenchyme Cells in Sea Urchin Embryos. *Developmental Biology* **1994,** *162* (2), 329-338.
53. Harkey, M. A.; Whiteley, A. H., The program of protein synthesis during the development of the micromere-primary mesenchyme cell line in the sea urchin embryo. *Developmental biology* **1983,** *100* (1), 12-28.
54. Page, L.; Benson, S., Analysis of competence in cultured sea urchin micromeres. *Experimental cell research* **1992,** *203* (2), 305-311.
55. Stephens, L.; Kitajima, T.; Wilt, F., Autonomous expression of tissue-specific genes in dissociated sea urchin embryos. *Development (Cambridge)* **1989,** *107* (2), 299-307.
56. Armstrong, N.; Hardin, J.; McClay, D. R., Cell-cell interactions regulate skeleton formation in the sea urchin embryo. *Development (Cambridge, England)* **1993,** *119* (3), 833.
57. Duloquin, L.; Lhomond, G.; Gache, C., Localized VEGF signaling from ectoderm to mesenchyme cells controls morphogenesis of the sea urchin embryo skeleton. *Development* **2007,** *134* (12), 2293-302.
58. Ettensohn, C. A., The regulation of primary mesenchyme cell patterning. *Developmental Biology* **1990,** *140* (2), 261-271.
59. Kiyomoto, M.; Tsukahara, J., Spicule Formation‐Inducing Substance in Sea Urchin Embryo. *Development, Growth & Differentiation* **1991,** *33* (5), 443-450.
60. Röttinger, E.; Saudemont, A.; Duboc, V.; Besnardeau, L.; McClay, D.; Lepage, T., FGF signals guide migration of mesenchymal cells, control skeletal morphogenesis [corrected] and regulate gastrulation during sea urchin development. *Development* **2008,** *135* (2), 353-65.
61. Ettensohn, C. A.; Guss, K. A.; Hodor, P. G.; K.M., M., The morphogenesis of the skeletal system of the sea urchin embryo. In *Progress in developmental biology*, J, C., Ed. Wiley and Sons: New York, 1997; Vol. VIII.
62. Piacentino, M. L.; Ramachandran, J.; Bradham, C. A., Late Alk4/5/7 signaling is required for anterior skeletal patterning in sea urchin embryos. *Development* **2015,** *142* (5), 943-52.
63. Taylor, E.; Heyland, A., Thyroid Hormones Accelerate Initiation of Skeletogenesis via MAPK (ERK1/2) in Larval Sea Urchins (Strongylocentrotus purpuratus). *Frontiers in endocrinology (Lausanne)* **2018,** *9*, 439-439.

64. Kitajima, T.; Okazaki, K., Spicule formation in vitro by the descendants of precocious micromeres formed at the 8-cell stage of sea urchin embryo. *Development, Growth & Differentiation* **1980,** *22* (3), 265-279.
65. Okazaki, K., Spicule formation by isolated micromeres of the sea urchin embryo. *Integrative and Comparative Biology* **1975,** *15* (3), 567-581.
66. Wu, C. H.; Park, A.; Joester, D., Bioengineering single crystal growth. *J Am Chem Soc* **2011,** *133* (6), 1658-61.
67. Adomako-Ankomah, A.; Ettensohn, C. A., Growth factor-mediated mesodermal cell guidance and skeletogenesis during sea urchin gastrulation. *Development* **2013,** *140* (20), 4214-25.
68. Karp, G. C.; Solursh, M., Dynamic activity of the filopodia of sea urchin embryonic cells and their role in directed migration of the primary mesenchyme in vitro. *Developmental Biology* **1985,** *112* (2), 276-283.
69. Sepulveda-Ramirez, S. P.; Toledo-Jacobo, L.; Henson, J. H.; Shuster, C. B., Cdc42 controls primary mesenchyme cell morphogenesis in the sea urchin embryo. *Dev Biol* **2018,** *437* (2), 140-151.
70. Hwang, S.-P. L.; Lennarz, W. J., Studies on the Cellular Pathway Involved in Assembly of the Embryonic Sea Urchin Spicule. *Experimental Cell Research* **1993,** *205* (2), 383-387.
71. Knapp, R. T.; Wu, C. H.; Mobilia, K. C.; Joester, D., Recombinant sea urchin vascular endothelial growth factor directs single-crystal growth and branching in vitro. *J Am Chem Soc* **2012,** *134* (43), 17908-11.
72. Benson, S.; Smith, L.; Wilt, F.; Shaw, R., The synthesis and secretion of collagen by cultured sea urchin micromeres. *Experimental cell research* **1990,** *188* (1), 141-146.
73. Wilt, F. H.; Benson, S. C., Isolation and Culture of Micromeres and Primary Mesenchyme Cells. Elsevier Science & Technology: 2004; Vol. 74, pp 273-285.
74. Wilt, F. H.; Hamilton, P.; Benson, S.; Kitajima, T., Culture of micromeres of *Strongylocentrotus purpuratus* in vitro. *Developmental Biology* **2000,** *225*, 212-213.
75. Ettensohn, C. A.; McClay, D. R., A new method for isolating primary mesenchyme cells of the sea urchin embryo: Panning on wheat germ agglutinin-coated dishes. *Experimental cell research* **1987,** *168* (2), 431-438.
76. Barsi, J. C.; Tu, Q.; Davidson, E. H., General approach for in vivo recovery of cell type-specific effector gene sets.(Report). *Genome Research* **2014,** *24* (5), 860-868.
77. Ettensohn, C. A.; McClay, D. R., The regulation of primary mesenchyme cell migration in the sea urchin embryo: Transplantations of cells and latex beads. *Developmental biology* **1986,** *117* (2), 380-391.
78. Miller, J.; Fraser, S. E.; McClay, D., Dynamics of thin filopodia during sea urchin gastrulation. *Development (Cambridge, England)* **1995,** *121* (8), 2501.
79. Oliveri, P.; Davidson, E. H.; McClay, D. R., Activation of pmar1 controls specification of micromeres in the sea urchin embryo. *Developmental biology* **2003,** *258* (1), 32-43.
80. Revilla-i-Domingo, R.; Oliver, P.; Davidson, E. H., A Missing Link in the Sea Urchin Embryo Gene Regulatory Network: hesC and the Double-Negative Specification of Micromeres. *Proceedings of the National Academy of Sciences - PNAS* **2007,** *104* (30), 12383-12388.

81. Benson, S.; Chuppa, S., Differentiation in vitro of sea-urchin micromeres on extracellular-matrix in the absence of serum. *The Journal of experimental zoology* **1990,** *256* (2), 222-226.
82. Malinda, K. M.; Fisher, G. W.; Ettensohn, C. A., Four-Dimensional Microscopic Analysis of the Filopodial Behavior of Primary Mesenchyme Cells during Gastrulation in the Sea Urchin Embryo. *Developmental biology* **1995,** *172* (2), 552-566.
83. Tu, Q.; Cameron, R. A.; Davidson, E. H., Quantitative developmental transcriptomes of the sea urchin Strongylocentrotus purpuratus. *Dev Biol* **2014,** *385* (2), 160-7.
84. Hodor, P. G.; Ettensohn, C. A., The Dynamics and Regulation of Mesenchymal Cell Fusion in the Sea Urchin Embryo. *Developmental biology* **1998,** *199* (1), 111-124.
85. Ettensohn, C. A.; McClay, D. R., Cell lineage conversion in the sea urchin embryo. *Developmental biology* **1988,** *125* (2), 396-409.
86. Urry, L. A.; Hamilton, P. C.; Killian, C. E.; Wilt, F. H., Expression of Spicule Matrix Proteins in the Sea Urchin Embryo during Normal and Experimentally Altered Spiculogenesis. *Developmental biology* **2000,** *225* (1), 201-213.
87. Killian, C. E.; Wilt, F. H., Endocytosis in primary mesenchyme cells during sea urchin larval skeletogenesis. *Exp Cell Res* **2017,** *359* (1), 205-214.
88. Vidavsky, N.; Addadi, S.; Schertel, A.; Ben-Ezra, D.; Shpigel, M.; Addadi, L.; Weiner, S., Calcium transport into the cells of the sea urchin larva in relation to spicule formation. *Proc Natl Acad Sci U S A* **2016,** *113* (45), 12637-12642.
89. Cheers, M. S.; Ettensohn, C. A., P16 is an essential regulator of skeletogenesis in the sea urchin embryo. *Developmental biology* **2005,** *283* (2), 384-396.
90. Balinsky, B. I., An electron microscopic investigation of the mechanisms of adhesion of the cells in a sea urchin blastula and gastrula. *Experimental cell research* **1959,** *16* (2), 429-433.
91. Gibbins, J. R.; Tilney, L. G.; Porter, K. R., Microtubules in the Formation and Development of the Primary Mesenchyme in Arbacia punctulata. I. The Distribution of Microtubules. *The Journal of cell biology* **1969,** *41* (1), 201-226.
92. Hagström, B. E.; Lönning, S., Time-lapse and electron microscopic studies of sea urchin micromeres. *Protoplasma* **1969,** *68* (3), 271-288.
93. Millonig, G., A study on the formation and structure of the sea urchin spicule. *Journal of Submicroscopic Cytology and Pathology* **1970,** *2*, 157-165.
94. Wolpert, L.; Mercer, E. H., An electron microscope study of the development of the blastula of the sea urchin embryo and its radial polarity. *Experimental cell research* **1963,** *30* (2), 280-300.
95. Amemiya, S., Development of the Basal Lamina and Its Role in Migration and Pattern Formation of Primary Mesenchyme Cells in Sea Urchin Embryos. *Development, growth & differentiation* **1989,** *31* (2), 131-145.
96. Anstrom, J. A.; Raff, R. A., Sea urchin primary mesenchyme cells: Relation of cell polarity to the epithelial-mesenchymal transformation. *Developmental biology* **1988,** *130* (1), 57-66.
97. Katow, H.; Solursh, M., Ultrastructure of primary mesenchyme cell ingression in the sea urchin *Lytechinus pictus*. *The Journal of experimental zoology* **1980,** *213* (2), 231-246.

98. Katow, H.; Solursh, M., Ultrastructural and time-lapse studies of primary mesenchyme cell behavior in normal and sulfate-deprived sea urchin embryos. *Experimental cell research* **1981,** *136* (2), 233-245.
99. Beniash, E.; Addadi, L.; Weiner, S., Cellular Control Over Spicule Formation in Sea Urchin Embryos: A Structural Approach. *Journal of Structural Biology* **1999,** *125* (1), 50-62.
100. Benson, S.; Jones, E. M. E.; Crise-Benson, N.; Wilt, F., Morphology of the organic matrix of the spicule of the sea urchin larva. *Experimental cell research* **1983,** *148* (1), 249-253.
101. Ameye, L.; Compère, P.; Dille, J.; Dubois, P., Ultrastructure and cytochemistry of the early calcification site and of its mineralization organic matrix in Paracentrotus lividus (Echinodermata: Echinoidea). *Histochemistry and cell biology* **1998,** *110* (3), 285-294.
102. Ameye, L.; Hermann, R.; Dubois, P., Ultrastructure of Sea Urchin Calcified Tissues after High-Pressure Freezing and Freeze Substitution. *Journal of structural biology* **2000,** *131* (2), 116-125.
103. Markel, K.; Roser, U.; Mackenstedt, U.; Klostermann, M., Ultrastructural investigation of matrix-mediated biomineralization in echinoids (Echinodermata, Echinoida). *Zoomorphology* **1986,** *106* (4), 232-243.
104. Markel, K.; Roser, U.; Stauber, M., On the ultrastructure and the supposed function of the mineralizing matrix coat of sea-urchins (Echinodermata, Echinoida). *Zoomorphology* **1989,** *109* (2), 79-87.
105. Decker, G. L.; Morrill, J. B.; Lennarz, W. J., Characterization of sea urchin primary mesenchyme cells and spicules during biomineralization in vitro. *Development (Cambridge)* **1987,** *101* (2), 297-312.
106. Ingersoll, E. P.; McDonald, K. L.; Wilt, F. H., Ultrastructural localization of spicule matrix proteins in normal and metalloproteinase inhibitor-treated sea urchin primary mesenchyme cells. *Journal of experimental zoology. Part A, Comparative experimental biology* **2003,** *300A* (2), 101-112.
107. Kitajima, T.; Urakami, H., Differential distribution of spicule matrix proteins in the sea urchin embryo skeleton. *Development, Growth & Differentiation* **2000,** *42* (4), 295-306.
108. Chang, I. Y. T.; Joester, D., Cryo-planing of frozen-hydrated samples using cryo triple ion gun milling (CryoTIGM™). *Journal of structural biology* **2015,** *192* (3), 569-579.
109. Chang, I. Y. T.; Joester, D., Large Area Cryo-Planing of Vitrified Samples Using Broad-Beam Ion Milling. *Microscopy and microanalysis* **2015,** *21* (6), 1616-1621.
110. DiCorato, A. Multi-Scale Imaging of Nanomaterial-Tissue Interactions. ProQuest Dissertations Publishing, 2021.
111. Ernst, S. G.; Hough-Evans, B. R.; Britten, R. J.; Davidson, E. H., Limited complexity of the RNA in micromeres of sixteen-cell sea urchin embryos. *Developmental Biology* **1980,** *79* (1), 119-127.
112. Harkey, M. A.; Whiteley, H. R.; Whiteley, A. H., Coordinate accumulation of five transcripts in the primary mesenchyme during skeletogenesis in the sea urchin embryo. *Developmental biology* **1988,** *125* (2), 381-395.
113. Zhu, X. D.; Mahairas, G.; Illies, M.; Cameron, R. A.; Davidson, E. H.; Ettensohn, C. A., A large-scale analysis of mRNAs expressed by primary mesenchyme cells of the sea urchin embryo. *Development (Cambridge)* **2001,** *128* (13), 2615-2627.

114. Sodergren, E.; Weinstock, G. M.; Davidson, E. H.; Cameron, R. A.; Gibbs, R. A.; Angerer, R. C.; Angerer, L. M.; Arnone, M. I.; Burgess, D. R.; Burke, R. D.; Coffman, J. A.; Dean, M.; Elphick, M. R.; Ettensohn, C. A.; Foltz, K. R.; Hamdoun, A.; Hynes, R. O.; Klein, W. H.; Marzluff, W.; McClay, D. R.; Morris, R. L.; Mushegian, A.; Rast, J. P.; Smith, L. C.; Thorndyke, M. C.; Vacquier, V. D.; Wessel, G. M.; Wray, G.; Zhang, L.; Elsik, C. G.; Ermolaeva, O.; Hlavina, W.; Hofmann, G.; Kitts, P.; Landrum, M. J.; Mackey, A. J.; Maglott, D.; Panopoulou, G.; Poustka, A. J.; Pruitt, K.; Sapojnikov, V.; Song, X.; Souvorov, A.; Solovyev, V.; Wei, Z.; Whittaker, C. A.; Worley, K.; Durbin, K. J.; Shen, Y.; Fedrigo, O.; Garfield, D.; Haygood, R.; Primus, A.; Satija, R.; Severson, T.; Gonzalez-Garay, M. L.; Jackson, A. R.; Milosavljevic, A.; Tong, M.; Killian, C. E.; Livingston, B. T.; Wilt, F. H.; Adams, N.; Bellé, R.; Carbonneau, S.; Cheung, R.; Cormier, P.; Cosson, B.; Croce, J.; Fernandez-Guerra, A.; Genevière, A.-M.; Goel, M.; Kelkar, H.; Morales, J.; Mulner-Lorillon, O.; Robertson, A. J.; Goldstone, J. V.; Cole, B.; Epel, D.; Gold, B.; Hahn, M. E.; Howard-Ashby, M.; Scally, M.; Stegeman, J. J.; Allgood, E. L.; Cool, J.; Judkins, K. M.; McCafferty, S. S.; Musante, A. M.; Obar, R. A.; Rawson, A. P.; Rossetti, B. J.; Gibbons, I. R.; Hoffman, M. P.; Leone, A.; Istrail, S.; Materna, S. C.; Samanta, M. P.; Stolc, V.; Tongprasit, W., The genome of the sea urchin Strongylocentrotus purpuratus. *Science (New York, N.Y.)* **2006,** *314* (5801), 941.
115. Tu, Q.; Cameron, R. A.; Worley, K. C.; Gibbs, R. A.; Davidson, E. H., Gene structure in the sea urchin Strongylocentrotus purpuratus based on transcriptome analysis. *Genome research* **2012,** *22* (10), 2079-2087.
116. Guss, K. A.; Ettensohn, C. A., Skeletal morphogenesis in the sea urchin embryo: Regulation of primary mesenchyme gene expression and skeletal rod growth by ectoderm-derived cues. *Development* **1997,** *124* (10), 1899-1908.
117. Hardin, J.; Coffman, J. A.; Black, S. D.; McClay, D. R., Commitment along the dorsoventral axis of the sea urchin embryo is altered in response to NiCl2. *Development (Cambridge)* **1992,** *116* (3), 671-685.
118. Söllner, C.; Burghammer, M.; Busch-Nentwich, E.; Berger, J.; Schwarz, H.; Riekel, C.; Nicolson, T., Control of Crystal Size and Lattice Formation by Starmaker in Otolith Biomineralization. *Science (American Association for the Advancement of Science)* **2003,** *302* (5643), 282-286.
119. Samata, T.; Hayashi, N.; Kono, M.; Hasegawa, K.; Horita, C.; Akera, S., A new matrix protein family related to the nacreous layer formation of Pinctada fucata. *FEBS letters* **1999,** *462* (1), 225-229.
120. Suzuki, M.; Saruwatari, K.; Kogure, T.; Yamamoto, Y.; Nishimura, T.; Kato, T.; Nagasawa, H., An Acidic Matrix Protein, Pif, Is a Key Macromolecule for Nacre Formation. *Science (American Association for the Advancement of Science)* **2009,** *325* (5946), 1388-1390.
121. Bittner, S. M.; Guo, J. L.; Mikos, A. G., Spatiotemporal Control of Growth Factors in Three-Dimensional Printed Scaffolds. *Bioprinting* **2018,** *12*, e00032.
122. Cao, L.; Mooney, D. J., Spatiotemporal control over growth factor signaling for therapeutic neovascularization. *Advanced drug delivery reviews* **2007,** *59* (13), 1340-1350.
123. Hu-Lowe, D. D.; Zou, H. Y.; Grazzini, M. L.; Hallin, M. E.; Wickman, G. R.; Amundson, K.; Chen, J. H.; Rewolinski, D. A.; Yamazaki, S.; Wu, E. Y.; McTigue, M. A.; Murray, B. W.; Kania, R. S.; O'Connor, P.; Shalinsky, D. R.; Bender, S. L., Nonclinical

Antiangiogenesis and Antitumor Activities of Axitinib (AG-013736), an Oral, Potent, and Selective Inhibitor of Vascular Endothelial Growth Factor Receptor Tyrosine Kinases 1, 2, 3. *Clinical cancer research* **2008,** *14* (22), 7272-7283.
124. Wray, G. A.; McClay, D. R., The origin of spicule-forming cells in a 'primitive' sea urchin (Eucidaris tribuloides) which appears to lack primary mesenchyme cells. *Development (Cambridge)* **1988,** *103* (2), 305-315.
125. Wilt, F. H.; Killian, C. E.; Hamilton, P.; Croker, L., The dynamics of secretion during sea urchin embryonic skeleton formation. *Exp Cell Res* **2008,** *314* (8), 1744-52.
126. Okazaki, K., Skeleton formation of sea urchin larvae: II. Organic matrix of the spicule. *Embryologia* **1960,** *5* (3), 283-320.
127. Gustafson, T.; Wolpert, L., Studies on the cellular basis of morphogenesis in the sea urchin embryo: Gastrulation in vegetalized larvae. *Experimental cell research* **1961,** *22*, 437-449.
128. Anstrom, J. A., Microfilaments, cell shape changes, and the formation of primary mesenchyme in sea urchin embryos. *The Journal of experimental zoology* **1992,** *264* (3), 312-322.
129. Gustafson, T.; Wolpert, L., Cellular movement and contact in sea urchin morphogenesis. *Biological reviews of the Cambridge Philosophical Society* **1967,** *42* (3), 442-498.
130. McClay, D. R., The Role of Thin Filopodia in Motility and Morphogenesis. *Experimental Cell Research* **1999,** *253* (2), 296-301.
131. Anstrom, J. A., Sea urchin primary mesenchyme cells: Ingression occurs independent of microtubules. *Developmental Biology* **1989,** *131* (1), 269-275.
132. Engqvist-Goldstein, A. E. Y.; Drubin, D. G., Actin assembly and endocytosis: From yeast to mammals. *Annual review of cell and developmental biology* **2003,** *19* (1), 287-332.
133. Mooren, O. L.; Galletta, B. J.; Cooper, J. A., Roles for Actin Assembly in Endocytosis. *Annual review of biochemistry* **2012,** *81* (1), 661-686.
134. Bloom, G. S.; Goldstein, L. S. B., Cruising along Microtubule Highways: How Membranes Move through the Secretory Pathway. *The Journal of cell biology* **1998,** *140* (6), 1277-1280.
135. Granger, E.; McNee, G.; Allan, V.; Woodman, P., The role of the cytoskeleton and molecular motors in endosomal dynamics. *Seminars in cell & developmental biology* **2014,** *31* (100), 20-29.
136. Shelley, M. J., The Dynamics of Microtubule Motor-Protein Assemblies in Biology and Physics. *Annual review of fluid mechanics* **2016,** *48* (1), 487-506.
137. Saha, K.; Kim, S. T.; Yan, B.; Miranda, O. R.; Alfonso, F. S.; Shlosman, D.; Rotello, V. M., Surface Functionality of Nanoparticles Determines Cellular Uptake Mechanisms in Mammalian Cells. *Small (Weinheim an der Bergstrasse, Germany)* **2013,** *9* (2), 300-305.
138. Takei, K.; Haucke, V., Clathrin-mediated endocytosis: membrane factors pull the trigger. *Trends in Cell Biology* **2001,** *11* (9), 385-391.
139. Ertl, R. P.; Robertson, A. J.; Saunders, D.; Coffman, J. A., Nodal-mediated epigenesis requires dynamin-mediated endocytosis. *Developmental dynamics* **2011,** *240* (3), 704-711.
140. Macia, E.; Ehrlich, M.; Massol, R.; Boucrot, E.; Brunner, C.; Kirchhausen, T., Dynasore, a Cell-Permeable Inhibitor of Dynamin. *Developmental cell* **2006,** *10* (6), 839-850.

141. von Kleist, L.; Stahlschmidt, W.; Bulut, H.; Gromova, K.; Puchkov, D.; Robertson, Mark J.; MacGregor, Kylie A.; Tomlin, N.; Pechstein, A.; Chau, N.; Chircop, M.; Sakoff, J.; von Kries, Jens P.; Saenger, W.; Kräusslich, H.-G.; Shupliakov, O.; Robinson, Phillip J.; McCluskey, A.; Haucke, V., Role of the Clathrin Terminal Domain in Regulating Coated Pit Dynamics Revealed by Small Molecule Inhibition. *Cell* **2011,** *146* (3), 471-484.
142. Dutta, D.; Williamson, C. D.; Cole, N. B.; Donaldson, J. G., Pitstop 2 Is a Potent Inhibitor of Clathrin-Independent Endocytosis. *PloS one* **2012,** *7* (9), e45799-e45799.
143. Winter, M. R.; Morgulis, M.; Gildor, T.; Cohen, A. R.; Ben-Tabou de-Leon, S., Calcium-vesicles perform active diffusion in the sea urchin embryo during larval biomineralization. *PLoS computational biology* **2021,** *17* (2), e1008780-e1008780.
144. Höing, S.; Yeh, T.-Y.; Baumann, M.; Martinez, N. E.; Habenberger, P.; Kremer, L.; Drexler, H. C. A.; Küchler, P.; Reinhardt, P.; Choidas, A.; Zischinsky, M.-L.; Zischinsky, G.; Nandini, S.; Ledray, A. P.; Ketcham, S. A.; Reinhardt, L.; Abo-Rady, M.; Glatza, M.; King, S. J.; Nussbaumer, P.; Ziegler, S.; Klebl, B.; Schroer, T. A.; Schöler, H. R.; Waldmann, H.; Sterneckert, J., Dynarrestin, a Novel Inhibitor of Cytoplasmic Dynein. *Cell chemical biology* **2018,** *25* (4), 357-369.e6.
145. Schindelin, J.; Arganda-Carreras, I.; Frise, E.; Kaynig, V.; Longair, M.; Pietzsch, T.; Preibisch, S.; Rueden, C.; Saalfeld, S.; Schmid, B.; Tinevez, J.-Y.; White, D. J.; Hartenstein, V.; Eliceiri, K.; Tomancak, P.; Cardona, A., Fiji: an open-source platform for biological-image analysis. *Nature Methods* **2012,** *9* (7), 676-682.
146. Hunter, J. D., Matplotlib: A 2D Graphics Environment. *Computing in science & engineering* **2007,** *9* (3), 90-95.
147. Killian, C. E.; Wilt, F., Molecular Aspects of Biomineralization of the Echinoderm Endoskeleton. *Chemical Reviews* **2008,** *108* (11), 4463-4474.
148. Politi, Y.; Levi-Kalisman, Y.; Raz, S.; Wilt, F.; Addadi, L.; Weiner, S.; Sagi, I., Structural Characterization of the Transient Amorphous Calcium Carbonate Precursor Phase in Sea Urchin Embryos. *Advanced Functional Materials* **2006,** *16* (10), 1289-1298.
149. Gong, Y. U.; Killian, C. E.; Olson, I. C.; Appathurai, N. P.; Amasino, A. L.; Martin, M. C.; Holt, L. J.; Wilt, F. H.; Gilbert, P. U., Phase transitions in biogenic amorphous calcium carbonate. *Proc Natl Acad Sci U S A* **2012,** *109* (16), 6088-93.
150. Politi, Y.; Metzler, R. A.; Abrecht, M.; Gilbert, B.; Wilt, F. H.; Sagi, I.; Addadi, L.; Weiner, S.; Gilbert, P. U., Transformation mechanism of amorphous calcium carbonate into calcite in the sea urchin larval spicule. *Proc Natl Acad Sci U S A* **2008,** *105* (45), 17362-6.
151. Tester, C. C.; Wu, C.-H.; Krejci, M. R.; Mueller, L.; Park, A.; Lai, B.; Chen, S.; Sun, C.; Balasubramanian, M.; Joester, D., Time-Resolved Evolution of Short- and Long-Range Order During the Transformation of Amorphous Calcium Carbonate to Calcite in the Sea Urchin Embryo. *Advanced Functional Materials* **2013,** *23* (34), 4185-4194.
152. Benson, S. C.; Benson, N. C.; Wilt, F., The Organic Matrix of the Skeletal Spicule of Sea Urchin Embryos. *The Journal of cell biology* **1986,** *102* (5), 1878-1886.
153. Venkatesan, M.; Simpson, R. T., Isolation and characterization of spicule proteins from Strongylocentrotus purpuratus. *Experimental cell research* **1986,** *166* (1), 259-264.
154. Killian, C. E.; Wilt, F. H., Characterization of the Proteins Comprising the Integral Matrix of Strongylocentrotus purpuratus Embryonic Spicules (∗). *The Journal of biological chemistry* **1996,** *271* (15), 9150-9159.

155. Peled-Kamar, M.; Hamilton, P.; Wilt, F. H., Spicule Matrix Protein LSM34 Is Essential for Biomineralization of the Sea Urchin Spicule. *Experimental cell research* **2002,** *272* (1), 56-61.
156. Wilt, F.; Croker, L.; Killian, C. E.; McDonald, K., Role of LSM34/SpSM50 proteins in endoskeletal spicule formation in sea urchin embryos. *Invertebrate biology* **2008,** *127* (4), 452-459.
157. Wilt, F.; Killian, C. E.; Croker, L.; Hamilton, P., SM30 protein function during sea urchin larval spicule formation. *Journal of structural biology* **2013,** *183* (2), 199-204.
158. Jain, G.; Pendola, M.; Rao, A.; Cölfen, H.; Evans, J. S., A Model Sea Urchin Spicule Matrix Protein Self-Associates To Form Mineral-Modifying Protein Hydrogels. *Biochemistry (Easton)* **2016,** *55* (31), 4410-4421.
159. Cho, J. W.; Partin, J. S.; Lennarz, W. J., A Technique for Detecting Matrix Proteins in the Crystalline Spicule of the Sea Urchin Embryo. *Proceedings of the National Academy of Sciences - PNAS* **1996,** *93* (3), 1282-1286.
160. Seto, J.; Zhang, Y.; Hamilton, P.; Wilt, F., The localization of occluded matrix proteins in calcareous spicules of sea urchin larvae. *Journal of Structural Biology* **2004,** *148* (1), 123-130.
161. Mann, S., Mineralization in biological systems. Springer Berlin Heidelberg: Berlin, Heidelberg, 2007; pp 125-174.
162. Kniprath, E., Growth of the Shell-field in Mytilus (Bivalvia). *Zoologica scripta* **1978,** *7* (1-4), 119-120.
163. Waller, T. R., Scanning electron microscopy of shell and mantle in the order Arcoida (Mollusca: Bivalvia). *Smithsonian contributions to zoology* **1980**.
164. Kocot, K. M.; Aguilera, F.; McDougall, C.; Jackson, D. J.; Degnan, B. M., Sea shell diversity and rapidly evolving secretomes: insights into the evolution of biomineralization. *Frontiers in zoology* **2016,** *13* (1), 23-23.
165. Clark, G. R., Shell Growth in the Marine Environment: Approaches to the Problem of Marginal Calcification. *American zoologist* **1976,** *16* (3), 617-626.
166. Marin, F.; Luquet, G., Molluscan biomineralization: The proteinaceous shell constituents of Pinna nobilis L. *Materials Science & Engineering C* **2005,** *25* (2), 105-111.
167. Bevelander, G.; Nakahara, H., An electron microscope study of the formation of the nacreous layer in the shell of certain bivalve molluscs. *Calcified Tissue Research* **1969,** *3* (1), 84-92.
168. Kaplan, D. L., Mollusc shell structures: novel design strategies for synthetic materials. *Current opinion in solid state & materials science* **1998,** *3* (3), 232-236.
169. Wada, K., Crystal growth of molluscan shells *Bull. Natl. Pearl Res. Lab.* **1961,** *7*, 703-785.
170. Addadi, L.; Weiner, S., Control and Design Principles in Biological Mineralization. *Angewandte Chemie (International ed.)* **1992,** *31* (2), 153-169.
171. Bøggild, O. B., The shell structure of the mollusks. *K. Dan. Vidensk. Selsk. Skr. Naturevidensk. Math. Afd.* **1930,** *9*, 233-326.
172. Carter, J. G., Guide to bivalve shell microstructures. In *Skeletal Growth of Aquatic Organisms*, Rhoads, D. C.; Lutz, R. A., Eds. Plenum Press: New York, 1980; pp 645-673.
173. Carter, J. G.; Clark, G. R., Classification and phylogenetic significance of molluscan shell microstructure. *Notes for a Short Course: Studies in Geology* **1985,** *13*, 50-71.

174. Ballarini, R.; Kayacan, R.; Ulm, F. J.; Belytschko, T.; Heuer, A. H., Biological structures mitigate catastrophic fracture through various strategies. *International journal of fracture* **2005,** *135* (1-4), 187-197.
175. Joubert, C.; Piquemal, D.; Marie, B.; Manchon, L.; Pierrat, F.; Zanella-Cleon, I.; Cochennec-Laureau, N.; Gueguen, Y.; Montagnani, C., Transcriptome and proteome analysis of Pinctada margaritifera calcifying mantle and shell: focus on biomineralization. *BMC genomics* **2010,** *11* (1), 613-613.
176. Marie , B.; Zanella-Cléon, I.; Le Roy, N.; Becchi, M.; Luquet, G.; Marin, F., Proteomic Analysis of the Acid-Soluble Nacre Matrix of the Bivalve Unio pictorum: Detection of Novel Carbonic Anhydrase and Putative Protease Inhibitor Proteins. *Chembiochem : a European journal of chemical biology* **2010,** *11* (15), 2138-2147.
177. Jackson, D. J.; Degnan, B. M., The importance of evo-devo to an integrated understanding of molluscan biomineralisation. *Journal of structural biology* **2016,** *196* (2), 67-74.
178. Addadi, L.; Weiner, S., Interactions between Acidic Proteins and Crystals: Stereochemical Requirements in Biomineralization. *Proceedings of the National Academy of Sciences - PNAS* **1985,** *82* (12), 4110-4114.
179. Gotliv, B.-A.; Addadi, L.; Weiner, S., Mollusk Shell Acidic Proteins: In Search of Individual Functions. *Chembiochem : a European journal of chemical biology* **2003,** *4* (6), 522-529.
180. Wilmot, N. V.; Barber, D. J.; Taylor, J. D.; Graham, A. L., Electron Microscopy of Molluscan Crossed-Lamellar Microstructure. *PHILOSOPHICAL TRANSACTIONS OF THE ROYAL SOCIETY B-BIOLOGICAL SCIENCES* **1992,** *337* (1279), 21-35.
181. Agbaje, O. B. A.; Thomas, D. E.; Dominguez, J. G.; McLnerney, B. V.; Kosnik, M. A.; Jacob, D. E., Biomacromolecules in bivalve shells with crossed lamellar architecture. *Journal of materials science* **2018,** *54* (6), 4952-4969.
182. Dauphin, Y.; Cuif, J.-P.; Cotte, M.; Salomé, M., Structure and composition of the boundary zone between aragonitic crossed lamellar and calcitic prism layers in the shell of Concholepas concholepas (Mollusca, Gastropoda). *Invertebrate biology* **2012,** *131* (3), 165-176.
183. Li, X. W.; Ji, H. M.; Yang, W.; Zhang, G. P.; Chen, D. L., Mechanical properties of crossed-lamellar structures in biological shells: A review. *Journal of the mechanical behavior of biomedical materials* **2017,** *74*, 54-71.
184. Kontoyannis, C. G.; Vagenas, N. V., Calcium carbonate phase analysis using XRD and FT-Raman spectroscopy. *Analyst (London)* **2000,** *125* (2), 251-255.
185. Bouasria, M.; Khadraoui, F.; Benzaama, M.-H.; Touati, K.; Chateigner, D.; Gascoin, S.; Pralong, V.; Orberger, B.; Babouri, L.; El Mendili, Y., Partial substitution of cement by the association of Ferronickel slags and Crepidula fornicata shells. *Journal of Building Engineering* **2021,** *33*, 101587.
186. Heuer, A. H.; Kamat, S.; Su, X.; Ballarini, R., Structural basis for the fracture toughness of the shell of the conch Strombus gigas. *Nature (London)* **2000,** *405* (6790), 1036-1040.
187. Kuhn-Spearing, L. T.; Kessler, H.; Chateau, E.; Ballarini, R.; Heuer, A. H.; Spearing, S. M., Fracture mechanisms of the Strombus gigas conch shell: Implications for the design of brittle laminates. *Journal of materials science* **1996,** *31* (24), 6583-6594.